

***Book of extended
abstracts***

11th

**European Conference
on Radar in Meteorology
and Hydrology**

***29th August - 02nd September 2022
Locarno, Switzerland***

INDEX

CLIMATOLOGICAL STUDIES

Classification of parent convective systems of tornadoes by using radarreflectivity

HAIL AND SEVERE CONVECTION

Off-shore and in-land hail detection through radar and satellite

HARDWARE, CALIBRATION AND MONITORING

Climatology of the “monitoring signals” to support maintenance

Monitoring Bright Ground Clutter Targets in the Canadian Weather Radar

HYDROLOGICAL APPLICATIONS

A flash flood warning system for ungauged basins in the tropical context of Reunion island

NOWCASTING OF CONVECTION AND THUNDERSTORMS

Meteorological Algorithm Requirements for Disaster Early Warning and Decision Support

Using Dual-Polarization Radars to Nowcast Severe Weather Events

POLARIMETRY

Refraction of radar beams in precipitation

QUANTITATIVE PRECIPITATION ESTIMATION

Supporting Weather Radar Observations with the Vaisala FD70

RADAR IN NUMERICAL WEATHER PREDICTION

Operational assimilation of radar reflectivity and radial wind volumes in the COSMO model at Arpae-SIMC

RADAR OPERATIONS AND NETWORKS

Centralisation in mainland France of the weather radar data processing system for the French overseas territories

Revision of the integration of disdrometers to improve the quality of the products at the coast

RADAR SIGNAL AND DOPPLER PROCESSING

Forward method for vertical air motion estimation from frequency modulated continuous wave radar rain measurements

CLIMATOLOGICAL STUDIES

Classification of parent convective systems of tornadoes by using radar reflectivit





CLASSIFICATION OF PARENT CONVECTIVE SYSTEMS OF TORNADOES BY USING RADAR REFLECTIVITY

Kotaro Fujii¹, Koji Sassa²

August 7, 2022

¹Graduate School of Integrated Arts and Sciences,
Kochi University, Kochi, Japan

²Science Cluster, Kochi University, Kochi, Japan

ABSTRACT

The present study aims to classify parent convective systems of tornadoes based on the echo pattern. Our radar network observed 28 systems and 34 vortices in them in Kochi Prefecture for 8 years from 2014. The systems are classified to isolated cell, cloud cluster, wavy cloud, super cell, squall line and inner rainband of typhoon. The characteristics of these convective systems are quite different. Then we easily identify their systems. The lower limit of maximum velocity is found to be 20m/s.

1. INTRODUCTION

In Japan, most of tornadoes are non-supercell type as mentioned by Niino et al. (1997). But the detailed classification of tornado type is not still made. If climatological description of tornadoes in Japan will be made based on the taxonomy established by Agee (2014), we can estimate degree of risk by tornadoes with respect to their parent convective systems and hazards wind watch issued by Japan Meteorological Agency (JMA) will be highly revised. Agee's taxonomy depends on many situations about parent convective systems. The radar echo pattern of their systems might be principal index. Tornadoes frequently occur in Kochi Prefecture in Japan. Especially in the coastline from Kochi city to Aki city, the probability of tornado occurrence is about 32 per year per 10,000 km² (Sassa et al. 2011). We observed many tornadoes by our X-band polarimetric radar network. The present study aims to classify parent convective systems of tornadoes based on the echo pattern. The characteristics of each convective systems and vortices in them are investigated.

2. ANALYSIS METHOD

Our radar network is composed of 6 X-band polarimetric radars and covers most of Kochi Prefecture. One of them is Asakura radar. Its beamwidth is 2 deg. and its observation range is 80 km. Asakura radar makes 2 lower elevation angles from 2 deg. every 1 min. and 8 elevation angles to make total volume scans every 5 min. The other radars' beamwidth and observation range are 2.7 deg. and 30 km, respectively. They make 5 elevation angles

from 3 deg. every 1 min. Two radar started observation since April 2014, and the network completed October 2018. Then, analysis period is 8 years from April 2014. When the tornado damage is reported by Kochi observatory of Japan Meteorological Agency (JMA) or hazardous wind watch is issued by JMA, we analyze the radar data. We also analyzed when SNS reported tornado occurrence. The reflectivity and Doppler velocity are drawn mainly for the lowest elevation angle, by using Draft developed by Meteorological Research Institute of JMA. Then, the altitude of the observation ranges from 600 to 1000 m AGL. We also used the data observed by Muroto JMA radar when the convective system was too large to be observed by our radars. Muroto radar is C-band Doppler radar and its beam width is 0.9 deg. We estimated the horizontal size of the parent convective systems with respect to the area of more than 40 dBZ in reflectivity. In the case of severe rain attenuation is observed, the correction is made with Kdp. The length, L , is corresponding to the dimension of long axis of the parent convective system and the width, W , is that of short one. The lifetime and moving velocity, V , of the parent convective system were estimated from the observed period, T , and moving velocity of vortex in it, respectively. The velocity difference, Dv , and diameter, D , of the vortex are measured from dipole signal of Doppler velocity. The maximum velocity, U_{max} , is obtained as sum of $Dv/2$ and V , which is the measure of tornado intensity.

Convective system	number
Isolated cell	12
Cloud cluster	9
Wavy cloud	2
Supercell	2
Squall line	2
Inner rainband	1

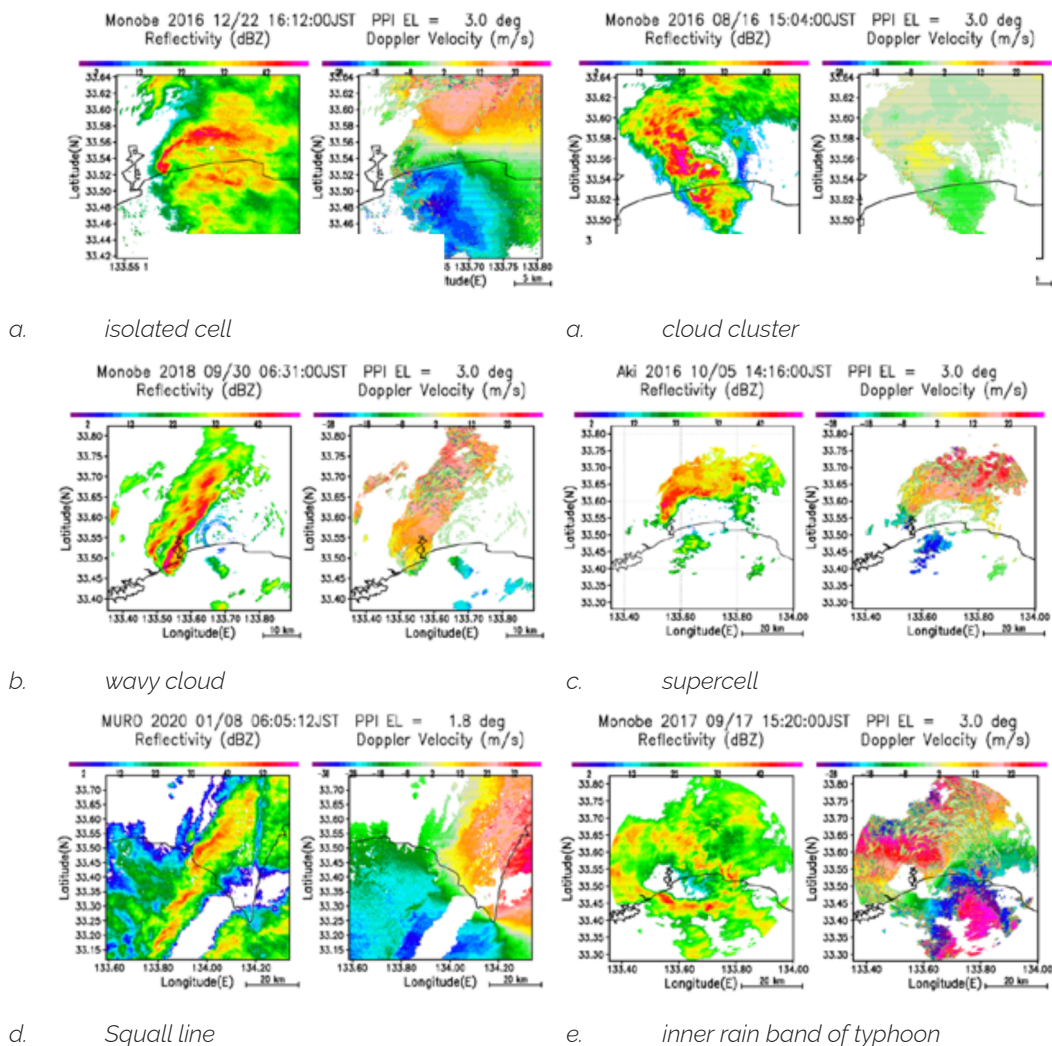
Table 1: Number of parent convective system

3. RESULT AND DISCUSSION

3.1 SYSTEM CLASSIFICATION

We detected 28 parent convective systems and 34 vortices in them. The parent convective systems are classified 6 types as shown in Table 1: isolated cell, cloud cluster, wavy cloud, supercell, squall line and inner rain band of typhoon. Typical echo patterns of them are shown in Fig.1. Isolated cell is the most popular system in this area. Its horizontal size is relatively small, but the clear hook echo accompanied by a tornado vortex is sometimes clearly observed as shown in Fig.1a. Cloud cluster is composed of many convective cells and the boundary between each cell is not clear. This system is secondary major system. Fig. 1b shows the smallest cloud cluster. The other cloud clusters are widely distributed. The wavy cloud is the array of slender cloud aligned parallel to the radial direction from the typhoon eye. The tornadoes due to typhoon usually occur in its outer rainband. The wavy clouds were, however, appeared the outer region of the outer rainband of the Typhoon, 'Trami', in September 2018. One of them yielded the JEF 1 tornado and another caused funnel cloud. Supercell has been thought as minor in Japan (Niino et al. 1997), we observed two cases for 8 years. We think that supercells were more frequently observed after 2008 when the Doppler radar became common in Japan. The example shown in Fig.1d is observed on the conversion line in the warm sector of extra tropical cyclone changed from the Typhoon, 'Chaba'. Squall line shown in Fig. 1e is long quasi-linear rainband moving to almost the right angle of it. They have relatively faster moving speed. Fig.1f shows the convective cell in the inner rainband of typhoon.

Figure 1
Typical radar echo patterns of parent convective systems



a. isolated cell

a. cloud cluster

b. wavy cloud

c. supercell

d. Squall line

e. inner rain band of typhoon

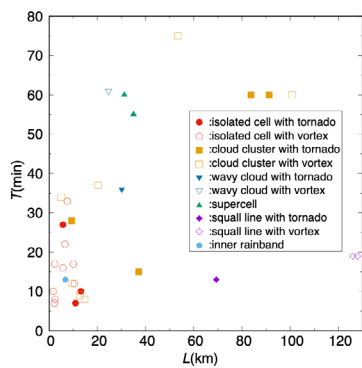


Figure 2: Length and width of parent system

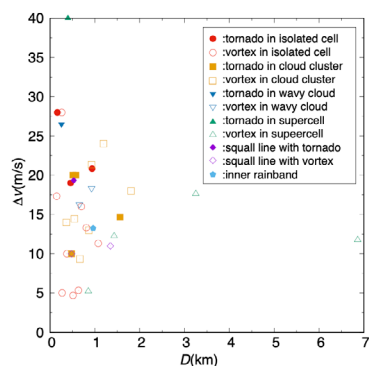


Figure 3: Length and moving velocity of parent system

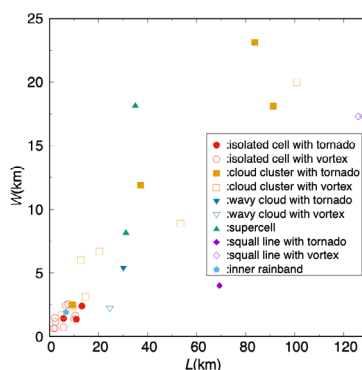


Figure 4: Length and lifetime of parent system

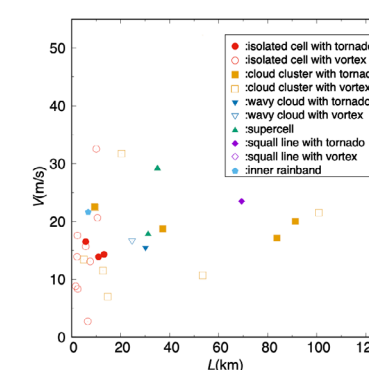


Figure 5: Diameter and velocity difference of vortex

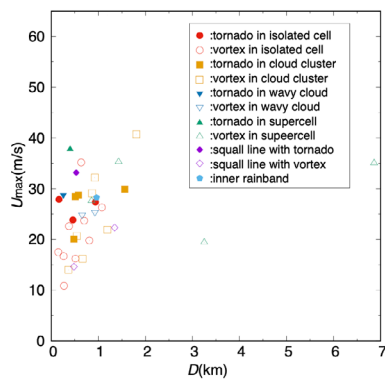


Figure 6: Maximum velocity and diameter of vortex

Figure 2 shows the length and the width of the parent convective systems. In this figure, solid symbols show the parent convective systems in which tornado caused damage whereas open symbols show those with no damage in spite of existence of vortex in them. Most of the parent cloud has large aspect ratio of more than 2 even for isolated cell. Especially, squall line and wavy cloud have large aspect ratio. Most of isolated cells are less than 10 km. Wavy clouds are as large as supercell but their width is quite different. Moving velocity distributes between 2 and 33 m/s as shown in Fig. 3. The parent convective systems yielding tornado damage have relatively large moving velocity more than 15 m/s. a. cloud cluster. This corresponds to the fact that the large vertical wind shear is relevant for tornado genesis. The lifetime of supercell is relatively long and some cloud clusters also have long lifetime as shown in Fig. 4. On the other hand, the lifetime of squall line is relatively short. Figure 5 shows the relationship between velocity difference and diameter of the vortices. Open symbols having large value show not tornado vortex but mesocyclone. Most of tornadoes caused damage are less than 1 km except one case. Some vortices can cause damage having relatively small velocity difference. This is because of large moving velocity. The maximum velocity plots collapse in small range from 20 m/s to 40 m/s as shown in Fig. 6. The lower limit of maximum velocity is found to be 20 m/s. Such value is smaller than that of marginal tornado (Wurman and Kosiba 2013). But it is reasonable if we consider the altitude of our observation. The no damage case having maximum velocity shows that these vortices locate offshore.

4. CONCLUSIONS

We classified the parent convective system of tornado to six types from the radar echo pattern; isolated cell, cloud cluster, wavy cloud, supercell, squall line and inner rainband of typhoon. Major types are isolated cell and cloud cluster. Squall line and wavy cloud are very slim. The lifetime of supercell is relatively long. The lower limit of maximum velocity is 20 m/s.

In Japan, X-band polarimetric radar network, XRAIN, is also constructed by MEXT. Then, the climatology of Japanese tornado will be investigating with the data obtained from XRAIN. In the future, the deep learning of these convective system will be enable to real time detection of the dangerous convective system and the hazardous wind watch will be improved dramatically.

ACKNOWLEDGMENTS

The present study was supported by the MIC/SCOPE 165009001 and JSPS KAKENHI 18H01682.

REFERENCES

- Agee, E.M.: A Revised Tornado Definition and Changes in Tornado Taxonomy, *Wea Forecasting*, 29, 1256–1258, <https://doi.org/10.1175/WAF-D-14-00058.1>, 2014.
- Niino, H., Fujitani, T. and Watanabe, N.: A Statistical Study of Tornadoes and Waterspouts in Japan from 1961 to 1993, *J. Climate*, 10, 1730–1752, [https://doi.org/10.1175/1520-0442\(1997\)010%3C1730:ASSOTA%3E2.0.CO;2](https://doi.org/10.1175/1520-0442(1997)010%3C1730:ASSOTA%3E2.0.CO;2), 1997.
- Sassa, K., Hamada, I., Hamaguchi, Y. and Hayashi T.: Characteristics of Mesocyclones Observed on Tosa Bay in Japan, *Ext. Abstract of the 6th European Conference on Severe Storms*, <https://www.essl.org/ECSS/2011/programme/abstracts/55.pdf>, 2011.
- Wurman, J. and Kosiba, K.: Finescale Radar Observations of Tornado and Mesocyclone Structures, *Wea. Forecasting*, 28, 1157–1174, doi: 10.1175/WAF-D-12-00127.1, 2013.

HAIL AND SEVERE CONVECTION

Off-shore and in-land hail detection through radar and satellite





OFF-SHORE AND IN-LAND HAIL DETECTION THROUGH RADAR AND SATELLITE

Antonini Andrea¹, Laviola Sante², Melani Samantha^{1,3}, Sonnini Aldo¹, Monte Giulio², Ortolani Alberto^{1,3}, Levizzani Vincenzo²

August 6, 2022

¹Laboratory of Monitoring and Environmental Modelling for the sustainable development, Sesto Fiorentino, Firenze, Italy

²Institute of Atmospheric Sciences and Climate, National Research Council, Bologna, Italy

³Institute of Bioeconomy, National Research Council, Firenze, Italy

ABSTRACT

The estimation of hail probability based on satellite and radar observations opens up interesting perspectives for nowcasting methods. Most ground instruments are based on impact sensors that can classify hailstones in terms of DSD and intensity; the weather radar systems (in particular the polarimetric ones) can observe microphysical processes of within-cloud atmospheric levels and weather satellites collect information from medium-high levels of precipitating systems. In this work a comparison between radar and satellite-based products is proposed for hail detection. S- and X-band single polarization radar data have been selected from the high Tyrrhenian Sea network. The Probability Of Hail (POH) has been estimated using two different approaches, based on the VIL (Vertical Integrated Liquid)-Density parameter and on the Waldvogel (1979) method, respectively. Satellite hail product is based on the MicroWave Cloud Classification-Hail (MWCC-H) method developed by Laviola et al. (2020a-b). This method exploits the whole suite of microwave high-frequency radiometers of the Global Precipitation Measurement Constellation (GPM-C) for detecting hail clouds and classifying the intensity degree of hail clusters: Hail Potential, Hail Initiation, Hail, and Super Hail. The hailstorms case studies have been selected by using raincap sensors (i.e., piezoelectric impact sensors measuring hail occurrence and intensity) mounted onboard of a ship-based GNSS-meteo observation network. The hail events were matched in time and space with the available satellite- and radar-based hail data. The comparison between the different POH products shows an encouraging cross consistency in the core and shape localization of the severe systems and in the quantification of the hail probability.

1. INTRODUCTION

In Japan, most of tornadoes are non-supercell type as mentioned by Niino. Severe weather systems are sometimes characterized by the presence of hail. Understanding the spatial and temporal variability of severe hail is important not only to advance the science of extreme weather and climate, but also for supporting urban-scale risk management. An accurate characterization of hail from in situ measurements is very difficult; instead, an operational hail detection system based on the synergy of heterogeneous

sensors could be a valid tool to this scope. From the remote sensing point of view, both from the ground and from space, hail detection is an open and challenging issue. In this work, we have exploited the potential offered by the GPM-C for monitoring and characterizing severe events with hail in connection with ground-based radar observations. In the last decades, the increasing number of passive microwave (PMW) satellite radiometers has stimulated the development of a variety of algorithms for studying clouds and precipitation rates; the high correlation between precipitation intensity and brightness temperature (TB) depression has been largely used as a diagnostic basis for identifying rain clouds and deriving hydrometeor phase. Also, reflectivity observations of ground radar systems, even in a single-polarization mode, have been used to derive the probability of hail and its intensity. Some hail case studies, as selected from piezoelectric impact sensors on board of a ship-based GNSS-meteo observation network, have been analyzed and preliminary results concerning the performance of satellite- and radar-based methodologies in assessing a probability of hail during severe weather events will be shown.

2. DATA AND METHODS

2.1 HAIL ESTIMATION FROM RADAR

The detection of hail is much more reliable and simpler if Doppler and polarimetric radars are used, and some algorithms already exist allowing to define a Probability Of Hail (POH) occurrence during the development of severe weather systems. Nevertheless, hail can be detected also using single polarization weather radars and some studies have been made to compare such different algorithms and to characterize their performance (Holleman, 2001), also focusing on X-band systems (Capozzi et al., 2016). When dealing with hail detection algorithms applied to single polarization radars, the analysis of the Vertical Profile of Reflectivity (VPR) is strictly necessary over the domain of POH occurrence. The estimation of the correct height relative to the measured reflectivity is strongly affected by error due to signal propagation in the atmosphere, resulting in uncertainties in hail (Delobbe and Holleman, 2006). A great number of elevations collected at every desired timestamp very often allows the estimation of the VPR for hail detection purposes, as occurs with the ten elevations acquired by the X-band Tuscany radar network used in this study. Greene and Clark (1972) firstly introduced the vertically integrated liquid water (VIL) as indicator of the severity of a storm cell, based on theoretical studies of drop size distributions and empirical studies of reflectivity factor and liquid water content. Using only VIL is, however, not straightforward because there is a large variability in the VIL threshold associated with the presence of hail. VIL density (VILD) is the VIL divided by the echo top height, and can be used to identify storms with high reflectivity values relative to their heights, which are very often characterized by hail (Amburn and Wolf, 1997). The increment of VILD is strongly correlated with the increment of hailstone size and quantity. In this work, we will adopt the empirical relationship of Capozzi et al. (2016) to convert VILD into POH. The empirical coefficients result from the analyses of measured VILD for 53 severe storms in the Gulf of Naples from 2012 to 2015:

$$POH(VILD) = 0.009344 (VILD)^3 - 0.1106 (VILD)^2 + 0.5057 (VILD) + 0.05351 \quad (\text{Eq. 1})$$

Most of the current methods for severe weather detection are based on Vertical Maximum Intensity (VMI) values, where each pixel represents the maximum reflectivity on the vertical column. Values exceeding 50dBZ very often indicate heavy rainfall (Auer Jr., 1994). A first indication of the

hail presence is given by the vertical location of the higher reflectivity values. To allow the hail formation process the maximum reflectivity must be above the freezing level. To this scope, the Waldvogel method uses the difference in altitude between the highest level attained by 45-dBZ reflectivity core (HZ45) and the height of the freezing level (Ho) (Waldvogel et al. 1979). Given ΔH as the difference between HZ45 and Ho (in km), the POH is expressed as:

$$POH(\Delta H) = 0.319 + 0.133 \Delta H \quad (\text{Eq. 2})$$

To implement the two methods for POH detection (POH(VLD) and POH(ΔH)), we used as radar data the volume scan reflectivity observations from the Elba (Tuscany, Italy) and Aleria (Corsica) systems. The first one is a non-polarimetric, X-band radar, covering a range of 108km and ten elevations (from 0.5° to 5.0° with a step of 0.5°). The second one is a Doppler, S-band radar, with a range of 256km and 5 elevations (0.6°, 1.0°, 1.4°, 3.2°, 4.5°). The WRF-ARW meteorological model is used to estimate the freezing level for computing the vertical extension of the systems. Two severe hail-storm cases will be presented and discussed in Section 3.

2.2 HAIL ESTIMATION FROM SATELLITE

The MicroWave Cloud Classification-Hail (MWCC-H) method for hail detection has been developed by Laviola et al. (2020a). The hail detection model is based on a probability model of growth (Verhulst, 1845) that exploits the TBs at 150 and 190 GHz. The general concept is based on the inverse proportionality between the upwelling radiation and hail cross-sections. As demonstrated above, the frequencies at 150 and 190 GHz are the most sensitive to the presence of hail being subject to a modification of their radiation field as a function of hail diameter. Furthermore, although their dynamic is pretty similar, the signal at 150 GHz channel tends to decrease more steeply than at 190 GHz. Therefore, we assume as model for hail detection a modified sigmoidal function as follows:

$$f(x, y) = 1 - \frac{1}{1 + e^{-(x-y)}} \quad (\text{Eq. 3})$$

where x and y are the TBs at 150 and 190 GHz, respectively. The difference between these two frequencies is demonstrated to be very sensitive to the growth of ice aggregates particularly when hail size is the order of centimeters. Eq. 3 shows boundaries between 0 with clear sky conditions and 1 when hail is progressively observed. Equation (3) is also reinforced by a variable inspired by the concept of carrying capacity of biological species, which is the maximum population size that the environment can sustain indefinitely or on the contrary the maximal load of the environment that modulates the population equilibrium. The carrying capacity is then a sort of regulator of population dynamics typically approximated by a probability model, which controls the occurrence of an overshooting of survival conditions that in long term leads to the collapse of the species. In the case of hail detection, the population (hail) impacts on the upwelling radiation (environment) by increasing the scattering effects (environment sustainability). The growth of hail sizes increases the scattering effects and then decreases the radiation to the satellite. This process is well described by Equation (3), which approximates the expected probability distribution as a function of decreasing TBs. To govern the dynamics of the probability model by stopping the computation when the sensitivity reaches

its maximum (overshooting) and no hail signatures can be recognized (saturation condition), a dynamic carrying capacity was introduced. The carrying capacity attains values in the range [0,1] and is described by the dimensionless variable K:

$$K(x) = \frac{\alpha}{x} \quad (\text{Eq. 4})$$

where $\alpha = 104 K$ and x is the TB at 150 GHz, frequency chosen because it reaches saturation conditions faster. For $K \ll 1$ the population load is minimum while for $K = 1$ the model reaches the overshooting and the computation stops. Thus, by regressing Eqs. (3) and (4) we derive a compact general model able to represent the hail size distribution as a function of TB depression. The result is a new function $H(K)$ that maps the probability of hail detection as only function of TB150:

$$H(K(x)) = 0.9844 \ln(K(x)) + 0.9072 \quad (\text{Eq. 5})$$

Table 1 shows the MWCC-H hail categories calculated through the Eq. (5) and the associated potential damages.

Table 1
MWCC-H hail categories as a function of the kinetic energy and potential damages of the hail impact at ground.

Probability of hail	Diameter range (cm)	Kinetic energy (J)	Terminal velocity (m s ⁻¹)	Category description	Potential damage
0.20 ÷ 0.36	~	~	~	Hail Potential (HP)	Absent to low
0.36 ÷ 0.45	< 2	< 33.84x10 ⁻²	< 19.09	Graupels/Hail Initiation (HI)	Low to moderate
0.45 ÷ 0.60	2 ÷ 10	33.84x10 ⁻² ÷ 423	19.09 ÷ 42.69	Large Hail (H)	High to severe
> 0.60	> 10	> 423	> 42.69	Super Hail (SH)	Severe to extreme

The dynamics of the hail detection model (Eq. 5) is modeled by the Temperature-Hail (T-H) diagram in Figure 1. The T-H proxy curve correlates the satellite signal at 150-157 GHz with the correspondent hail probability. Thus, the T-H diagram is a sort of "slide rule" to quickly identify the hail diameter category by crossing the instantaneous measurements of TBs in the channel at 150-157 GHz with the hail categories and associated potential damages.

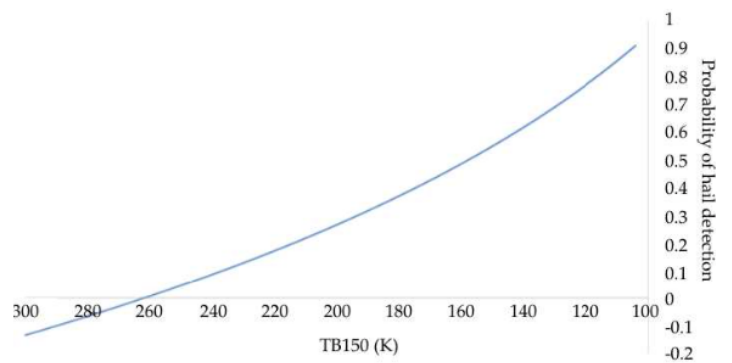


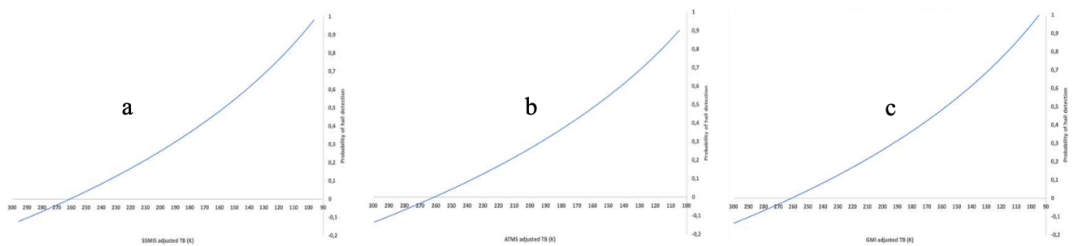
Figure 1: Distribution of hail probabilities calculated from Eq. (5) as a function of TB150.

Eq. (5), originally developed for the radiometers Advanced Microwave Sounding Unit-B (AMSU-B) and Microwave Humidity Sounder (MHS), has been generalized to all MHS-like sensors orbiting on the Global Precipitation Measurement Constellation (GPM-C). As demonstrated by Laviola et al. (2020b), the MHS-like channels in the frequency range 150-170 GHz have been adjusted on the MHS channel 2 (157 GHz) in order to account for the instrumental differences and tune the original model on the MHS-like technical characteristics:

$$TB_{MHS-i}^R = \frac{TB_i - b_i}{a_i} + C_i^{th} \quad (\text{Eq. 6})$$

where TB_{MHS-i}^R is the MHS reconstructed signal at 157 GHz through the brightness temperature TB_i for each radiometer i (ATMS, SSMIS, GMI) and C_i^{th} designates the correction terms calculated on the basis of the TB threshold (th) values for each radiometer. The linear regression described by Eq. (3) is then applied to all GPM-C MHS-like sensors to feed the original scheme of the MWCC-H hail detection model. Further details can be found in Laviola et al. (2020b).

Figure 2
T-H diagrams for the adjusted signals as measured from the ATMS (a), SSMIS (b) and GMI (c) useful for directly identifying the hail categories.



3. CASE STUDIES

Two case studies of hailstorm were selected based on piezoelectric impact measurements acquired by Vaisala Raincap sensors mounted on board of a ship-based GNSS-meteo observation network. The first hailstorm hits the Tuscany coast and the nearby islands on 30 December 2020. This event was observed and reconstructed by several passages of the GPM-C sensors, that scanned the area during the day. The contrast between different air masses enhanced severe instability conditions with large hail production and falls observed on the coastal areas. In Figure 3 six passages of the GPM-C platforms are shown: they well reconstructed the evolution of the hail systems during the day, that affected mainly the central area of the Tuscany coast in the first part of the day and then the southmost areas. It can be seen that only the GMI sensor retrieved the highest hail probability with values up to 0.5 (H), while the probability observed by the other sensors was in the HP range. Ground-radar observations, through POH(VILD) detection results (Figure 5), confirm the area of maximum hail formation, showing a tongue of instability from northern of Corsica towards Tuscany coasts passing over Elba Island, with averaged probability values around 0.5 (H). POH(VILD) results by Aleria observations (Figure 5b) show a more detailed reconstruction of the hailstorm due to the lower signal attenuation in the S- compared to the X-band, also because of the system occurrence very near to the radar site. Only results obtained with POH(VILD) method are shown as they are more accurate than those derived with POH(ΔH) method. The second case study refers to the hailstorm that affected the city of Livorno on 10 June 2020. It was observed by four different passages of the GPM-C platforms, shown in Figure 4. It can be seen

that the storm developed in the night, reached its maximum at around 0330UTC and weakened in the following hours. The difference in the hail probability estimation between GMI (Figure 4a) and F16-SSMIS (Figure 4b) is due mainly to the better horizontal resolution of the former. Also in this case, radar observations (at least for Aleria radar system) detect a long instability tongue that starting from the north of Corsica and passing on the Elba Island extends along the central Tuscany coasts, going inland (Figure 6). A second center of hail formation was detected on the sea in front of the Ligurian coasts. The localization and intensity of hail probability shows a good match between the satellite- and radar-based methodologies, opening up to interesting perspectives for hail detection and its evolution in an operational fashion.

Figure 3
Hail probability reconstructed by the GPM-C sensors on 30 December 2020. a) GPM-GMI at 0830UTC, b) MOB-MHS at 0922UTC, c) F17-SSMIS at 1705UTC, d) N19-MHS at 1759UTC, e) MOC-MHS at 1957UTC and f) MOB-MHS at 2044UTC.

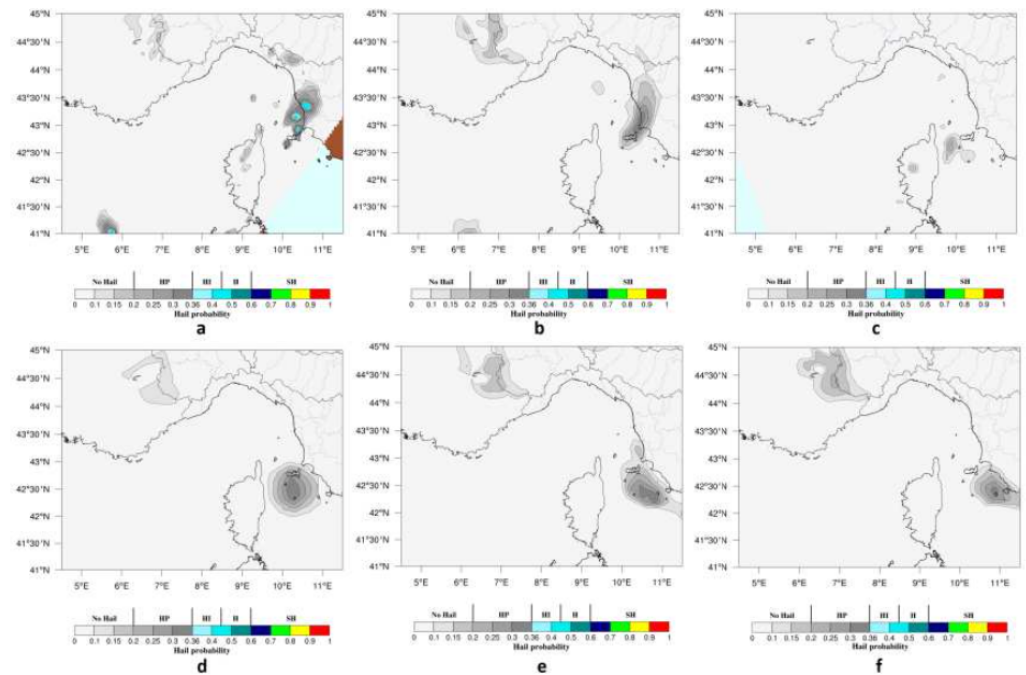


Figure 4
Hail probability reconstructed by the GPM-C sensors on 10 June 2020. a) GPM-GMI at 0335UTC, b) F16-SSMIS at 0340UTC, c) N19-MHS at 0557UTC and d) F17-SSMIS at 0640UTC.

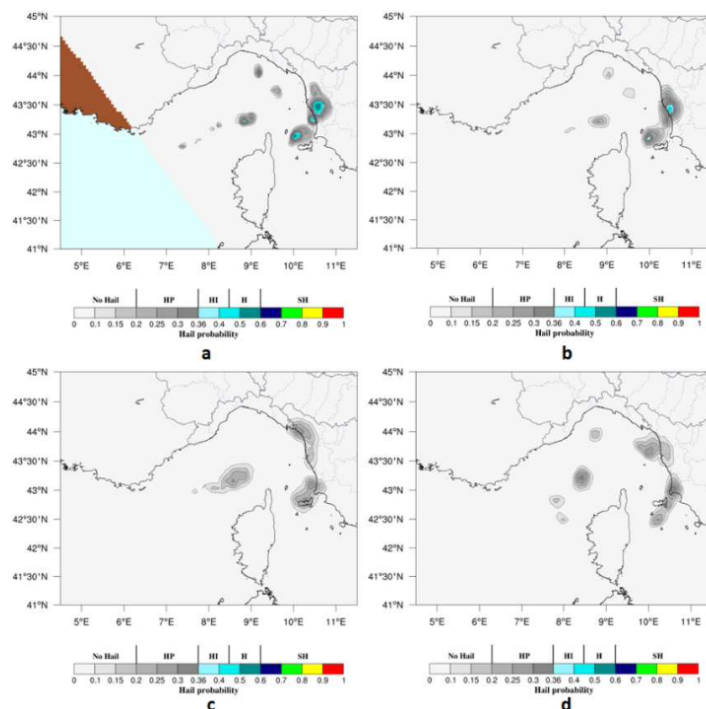


Figure 5
POH(VILD) as computed using the Elba X-band (a) and Aleria S-band (b) radars.
Time: 30/12/2020 8:30 UTC.

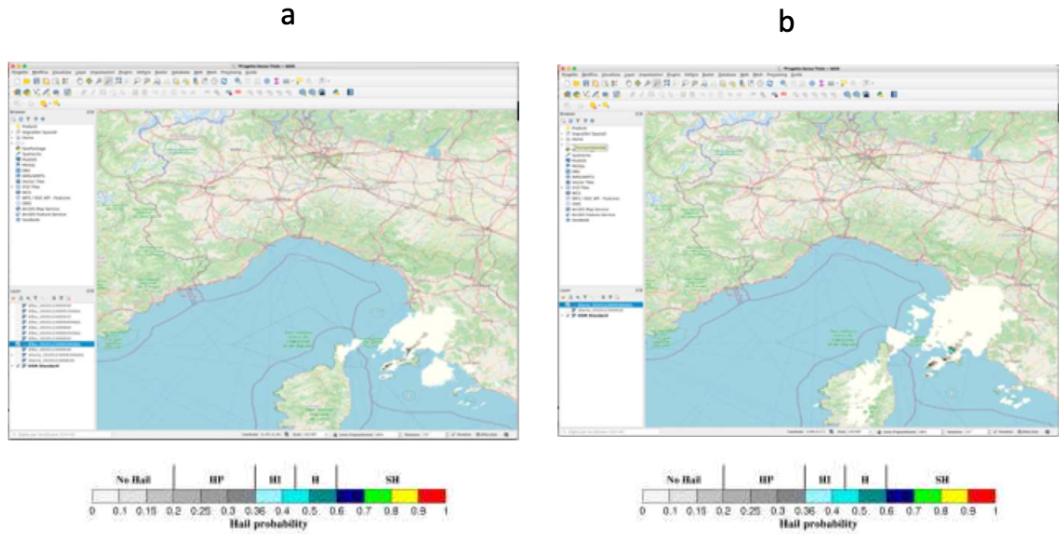
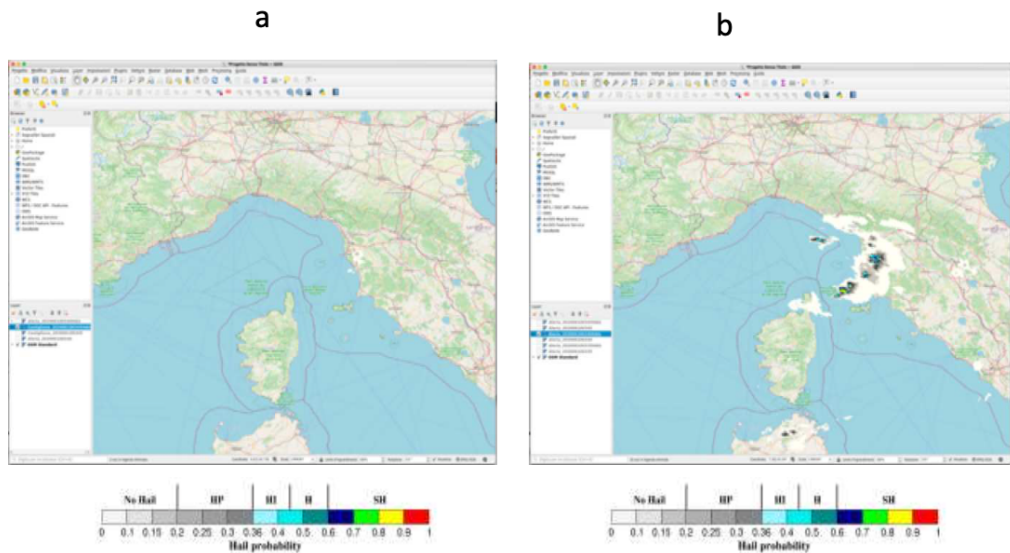


Figure 6
POH(VILD) as computed using the Elba X-band (a) and Aleria S-band (b) radars.
Time: 10/06/2020 3:40 UTC.



4. CONCLUSIONS

The detection and monitoring of the occurrence and intensity of hailstorms are fundamental not only for a deeper understanding of their dynamics, but for an operational context where the nowcasting of such events has a relevant impact on economic, social and human issues. Two methodologies were described for assessing the probability of hail: one based on satellite data, the other on radar observations. The preliminary results comparing the two methodologies for some case studies are encouraging and show good results in terms of cross consistency in the core and shape localization of the severe systems and in the quantification of the hail probability, even with single-polarization radar systems. To explore and further evaluate the potential of such algorithms and how their synergy could benefit the hail detection, other case studies should be systematically examined, enlarging the number of recorded hail cases. A great contribution was made by piezoelectric impact sensors mounted on board of a ship-based GNSS-meteo observation network, which have detected some hailstorms even on the sea where the measurements are almost totally absent or poorly reported, offering a unique opportunity to study their formation and evolution in the sea-atmosphere dynamics framework.

REFERENCES

- Amburn, S., and P. Wolf: VIL Density as a Hail Indicator. *Weather And Forecasting* (12), 473-478, 1997.
- Auer Jr., A.: Hail Recognition through the Combined Use of Radar Reflectivity and Cloud-Top Temperatures. *Monthly Weather Review*, 2218-2221, 1994.
- Capozzi, V., E. Picciotti, V. Mazzarella, G. Budillon, and F. Marzano: Hail storm hazard in urban areas: identification and probability of occurrence by using a single-polarization X-band weather radar. *Hydrology and earth System Science Discussions* [preprint], <https://doi.org/10.5194/hess-2016-177>, 2016.
- Delobbe, L., and I. Holleman: Uncertainties in radar echo top heights used for hail detection. *Journal Meteor. Appl.*, 361-374, 2006.
- Greene, D., and R. Clark: Vertically Integrated Liquid Water - A new analysis tool. *Monthly Weather Review*, 548- 552, 1972.
- Holleman, I.: Hail detection using single polarization radar. KNMI number: WR-200101, 2001. Laviola S., V. Levizzani, R. R. Ferraro, and J. Beauchamp: Hailstorm Detection by Satellite
- Microwave Radiometers, *Remote Sens.*, 12(4), 621, <https://doi.org/10.3390/rs1204062>, 2020a. Laviola S., G. Monte, V. Levizzani, R. R. Ferraro, and J. Beauchamp: A new method for hail detection from the GPM constellation. A prospective for a global hailstorm climatology, *Remote Sens.*, 12(21), 3553; <https://doi.org/10.3390/rs12213553>, 2020b.
- Verhulst, P.-F. *Recherches mathématiques sur la loi d'accroissement de la population*. *Nouv. Mémoires l'Académie R. Sci. Belles-Lett. Brux.* 1845, 18, 14-54. Available online: <http://eudml.org/doc/182533>.
- Waldvogel, A., B. Federer, and P. Grimm: Criteria for the Detection of Hail Cells, *J. of Applied Meteor. and Clim.*, 18(12), 1521-1525, 1979.

HARDWARE, CALIBRATION AND MONITORING

Climatology of the “monitoring signals” to support maintenance

Monitoring Bright Ground Clutter Targets in the Canadian Weather Radar





CLIMATOLOGY OF THE “MONITORING SIGNALS” TO SUPPORT MAINTENANCE

Maruri Mercedes^{1,2}, Alkiza A³, Gaztelumendi Santiago¹, Aranda Jose Antonio³

August 1, 2022

¹*Tecnalia Basque Research and Technology Alliance (BRTA)- Meteo & Climate Area, Zamudio, Spain*

²*University of the Basque Country UPV/EHU, Bilbao, Spain*

³*DAEM / Basque Meteorology Agency*

ABSTRACT

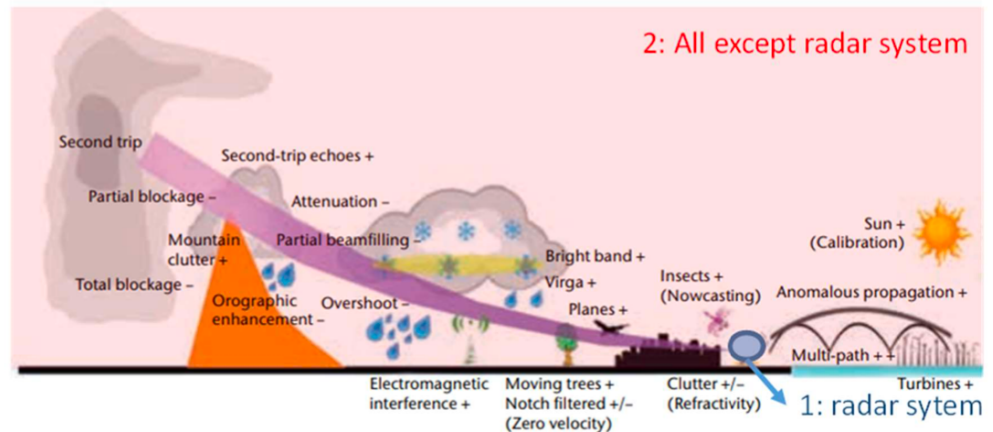
The daily routine of monitoring the weather radar is a useful systematic task for detection of malfunction of the system. In addition, old systems require advance-monitoring tasks to maintain the best quality of data that it is possible to register. The unusual, incoherent or strange signals are always a source of interest because they respond to some uncontrolled target or situation. The quality of the final products is associated in many studies to a well list of sources of errors and this is an indicator of the quality and representative of the data registered in a particular meteorological phenomenon, in space and time. There are new sources of errors that start to appear with the life of the radar, what happens with old systems and the subtle imbalance in hardware error? The role of the monitoring signals, their studies and experiences of the past, give a good approximation of the deviations in the present situation. The present study shows how useful it is to study trends of these monitoring signals to find deviations in the operation, which could have an impact in the final products and sometimes require an immediate maintenance action that could reduce, solve the present trend. The signature patterns of the monitoring signals help to find these changes in time. This work shows some of the experiences of the identification of these irregularities of the monitoring signals in the historical monitoring signals and how it proceeded.

1. INTRODUCTION

There are many studies in the past that identify sources of error in radar data (Germann, y otros, 2022), (WMO, 2014), (Osródka & Szturc, 2022). These sources of error are associates with the return signal containing information from targets other than the desired hydrometeor target, or that the sampling volume is not representative of the precipitation content at that point in space. In general, it can be stated that the return signals from these systems are complex and the sources of error appear in combination with each other and with the desired target (hydrometeors). Assigning an index of quality of the data is not an easy task (Zhang, Youcun, Langston, & Kaney, 2011) instead, it is important to understand the mathematical concept of distance or uncertainty, which are known, as the closeness between the measured data and the truth data. Any of the cases above,

in absence of correction (Harrison, Driscoll, & Kitchen, 2000), (Bech, 2001) lead to a bad estimation of the "quantitative precipitation estimation-QPE and quantitative precipitation forecast-QPF", if it is not controlled at the product level. In general, all the radar products require specific corrections according to the site. However, the concept of quality is always associated with the data and its application and therefore what is valid for one application does not necessarily have to be useful for another. The corrections subject to the error detected, involves a manipulation of the record in order to bring the data closer to the real data.

Figure 1
Error sources Figure
modified from the
bibliography. 1.-Radar
system vs 2.-Comple-
mentary to radar
system.



The Kapildui radar, which belongs to the hydrological observation network of the Basque Government, particularly the Directorate of Attention of Emergency and Meteorology (DAEM), was installed in 2005 in complex terrain. It is a Selex Gematronik's polarimetric radar, more precisely a METERO 1500C model, C-band, Doppler, and a Klystron type transmitter. Among the polarimetric radars it is an old model and the hardware is only capable of measuring the polarimetric variable "horizontal reflectivity" ZDR (dB). This system has shown another way of viewing the precipitation field over the years and has enabled the monitoring of very severe atmospheric phenomena in the Basque Country, with two episodes of tornadoes, never recorded and validated before, being particularly noteworthy (Gaztelumendi, Egaña, Martija, & Palacio, 2015) (Gaztelumendi, Egaña, & Aranda, 2019) (Maruri, y otros, 2014). The operational and maintenance experience of more than 16 years and more than 10 years of hours of such a robust system in operation and maintenance has extended the concept of quality described above. Weather radar is a system that requires a monitoring and operational strategy coordinated due to the service it provides, to ensure, availability and the best data at the most adverse weather time (EUMETNET OPERA 5-Work Package OA1, 2020). These data are fed into the decision making chain which, together with other observations, prediction models and own experience from similar situations, allows the best decision to be made in many different situations (Binetti, Campanale, Massarelli, & Uricchio, 2022), (Federal Aviation Administration, 2022), (Doksaeter & Dankert, 2016). The aim of this paper is to present in an organised way the study of the signals that are carried out during the monitoring process and which alert the need for maintenance to ensure the best possible future data recording. The context and motivation for this work is to show the importance of monitoring in systems older than 10 years and how past experience can be used in new installations in the future.

2. METHODOLOGY

The methodology is based on the analysis of the information recorded in the monitoring tasks. These tasks are performed on the raw data: Zh, ZDR and Vr, the BiTE of the control, and the system log file and consist, of a visual and numerical inspection of these data. The aim is to identify the routine checks that must be carried out to ensure and verify that the assurance of raw data recorded are correct because there is not any irregularity in the acquisition of the system.

The following are some of the statements and definitions that have been used.

The methodology assumes that the best recorded data only depends on the correct functioning of the system, given that, if a source of error is detected in the radar, the impact in the quality of the data must be assessed. For example, a biological target is systematically detected in certain periods of the year, a system failure is, not detect it, in a certain migration period without filtering procedures, but detecting it ensures the correct functioning of the system, although the finally quality of the hydrological data will depend on the filtering processes. The methodology consider that, as system age, the frequency and type of maintenance increases, and monitoring becomes more important in operational systems. Therefore, maintenance and monitoring are dynamic systems whose control tools are adjusted to the situation derived from maintenance and monitoring history itself. As a result, reporting and maintenance are becoming more relevant.

Monitoring Works with the concepts of "outliers", "anomalous", "differences" in a qualitative evaluation.

The following definition is used for "data quality"; the data is divided in two parts, data that is verified and good because it has been recorded after having validated the correct functioning of the system and data quality according to the representativeness in a specific application Fig 1.

Definition to the concept "monitoring signal" vs "strange signal". There are signals that are sought to verify the correct functioning of the system and these are the "monitoring signals" and then the signal is validated according to its application, if atmospheric signals are sought, the rest are discarded, but sometimes, biological signals are sought and they must be separated from the atmospheric signals. Nevertheless, there are some cases where the target is not identified and these are called "strange signals".

"Differences" refer to sudden changes in signals. Sometimes they have an explanation, but sometimes you have to work together with maintenance to address the situation. Finally, manual monitoring (visual and numerical) is done globally by assigning qualitative value that allows to work later on the quality of data and to modify the data according to the local meteorological characteristics. Any correction must be studied to know whether or not it can be applied to a specific radar, due to its technical characteristics, scanning and local environment.

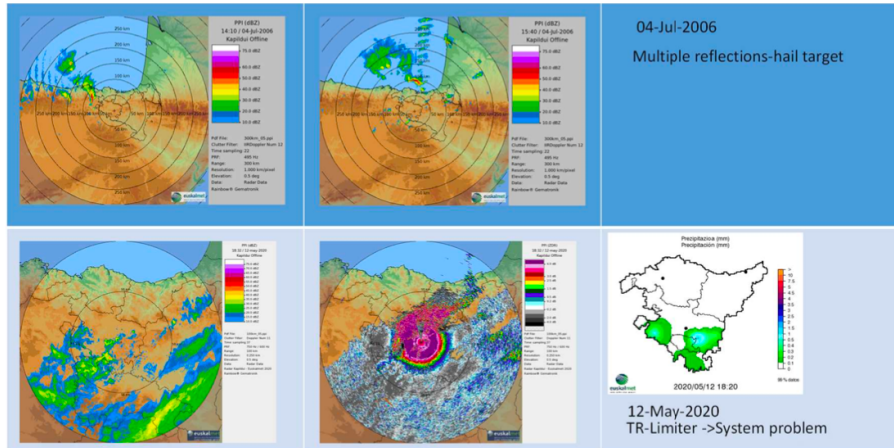
The results are presented as a selection of examples from the database recorded in the monitoring tasks, and correspond to different moments of the Kapildui radar from 2005 to the present that have been considered as "outliers", "anomalous", "differences" and the impact they have had on the operation of the system. At the end of the results a verification scheme of signals is presented, which should be looked for to ensure the correct functioning of the system.

3. RESULTS

The results is a selection of a rare or unique images detected during the study years and a scheme of the monitoring process.

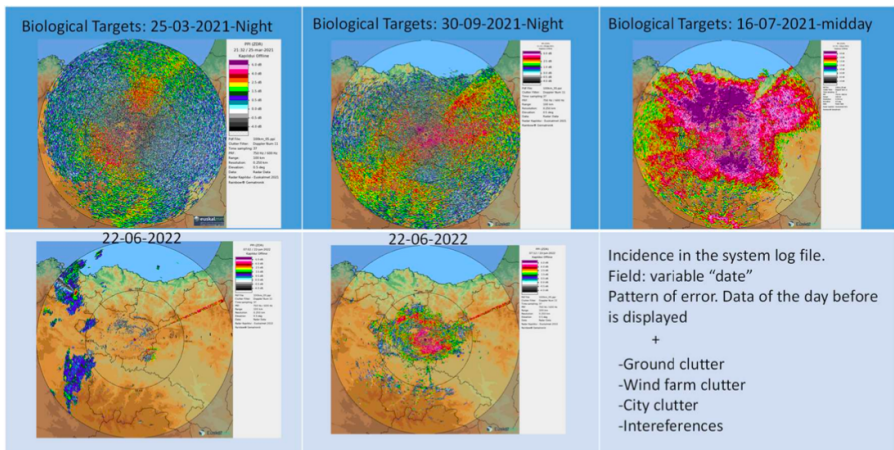
Example 1

Figure 2
Hail Target (First line).
TR-Limiter Problem
(Second line)



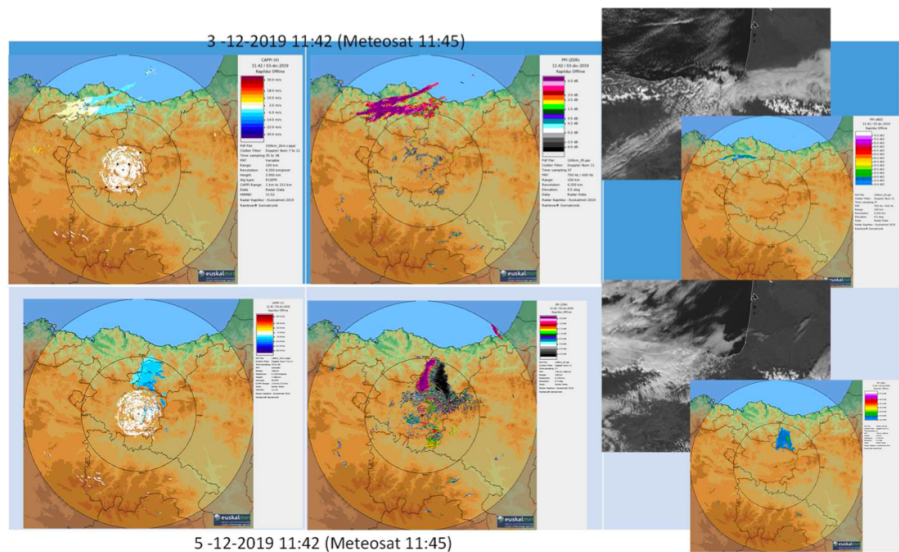
Example 2

Figure 3
Different biological
patterns (First line).
Common Clutter
signals and a system
log file problem, wrong
registered date
(Second line).



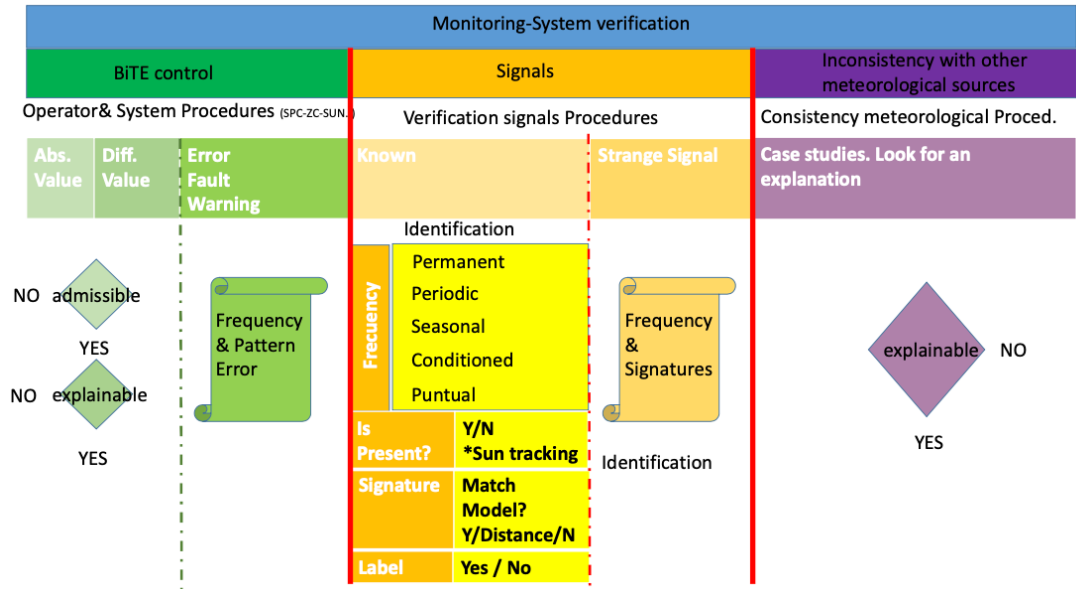
Example 3
Strange signals.

Figure 4
Strange signals.



The results of the present study are presented in a decision making diagram. This monitoring process is an adaptation of bibliographic monitoring documents to the daily routines in a regional meteorological.

Figure 5
Scheme of the
Monitoring&System
verification.



4. CONCLUSIONS

In general, any type of measuring instruments has a variable behaviour over time. Depending on the time scale used, it would be more accurate to speak of life periods. Monitoring and maintenance must be adjusted to these periods in order to always record the best data. Over the years, the operation and monitoring of data in real time has taught you to see radar in a wide range of weather situations. The numerous case studies that have been presented at this conference have helped to better understand the interaction between radar and Basque meteorology, and actions at different levels, operational, anticipating possible malfunctions and poor quality products for different applications, improving or creating new products more in line with the needs and requirements of customers. There is currently a catalogue of "strange signals", unresolved or whose frequency has been unique. Experience over the years indicates that, even if BiTE does not indicate substantial changes, sharp variations in signal are always an indication of bad performance because these are not explained in meteorological terms. There has to be a correlation between signals and BiTE. As has been seen in some of the examples presented. Frequency Development of new tools involving very methodical and regular procedures, as well as the adaptation of operations to radars that are more than 10 years old. Documenting signals and studying the signatures and behaviour of situations not only helps to better understand the meteorology but also to optimise monitoring by maximising the availability of verified data for other applications. The monitoring task is a complex procedure that it has been adapted to the resources of a regional meteorological service. But, the experience of more than 10 years of operation is enough to know and follow the operation behaviour of the radar and to identify abnormal execution sequences in time in the log files. Theses abnormal tasks are equivalent to instabilities in the operation of the radar.

ACKNOWLEDGMENTS

This paper is a reflection of many years of monitoring the data from the Kapildui radar, which would not have been possible without the trust placed in it by the DAEM, the meteorology area of TECNALIA and the final degree projects of students from the Bilbao School of Engineering UPV/EHU.

REFERENCES

- *Bech, J. (2001). ANOMALOUS PROPAGATION EFFECTS ON WEATHER RADAR BEAM BLOCKAGE CORRECTIONS. Proceedings- 30th International Conference on Radar Meteorology, 2.*
- *Binetti, M., Campanale, C., Massarelli, C., & Uricchio, V. (2022). The Use of Weather Radar Data: Possibilities, Challenges and Advanced Applications. Earth, 157-171.*
- *Doksaeter, A., & Dankert, S. (2016). Use of online weather information in everyday decision-making by laypeople and implications for communication of weather information. Meteorological Applications, 650-662. doi:DOI: 10.1002/met.1588*
- *EUMETNET OPERA 5-Work Package OA1. (2020). Monitoring of weather radars: lessons learned from WXRCalMon17 & WXRCalMon19, and recommendations. Geneva: Eumetnet. Obtenido de https://www.eumetnet.eu/wp-content/uploads/2021/07/opera_monitoring_recommendations_1_21.pdf*
- *Federal Aviation Administration. (29 de 07 de 2022). Next Generation Weather Radar (Nexrad). Obtenido de https://www.faa.gov/air_traffic/weather/nexrad/*
- *Gaztelumendi, S., Egaña, J., & Aranda, J. (2019). A study of a tornado event in Basque Country: the 4th July 2018 case. European Conference on Severe Storms, (pág. 1). Poland. doi:DOI:10.13140/RG.2.2.20693.14560*
- *Gaztelumendi, S., Egaña, J., Martija, M., & Palacio, V. (2015). Storms with very heavy showers and hail in Basque Country: 23 Jun 2014 case. European Conference on Severe Storms. Viena: Proceedings.*
- *Germann, U., Boscacci, M., Clementi, L., Gabella, M., Hering, A., Sartori, M., . . . Calpini, B. (2022). Weather Radar in Complex Orography. Remote Sensing, 40. doi:<https://doi.org/10.3390/rs14030503>*
- *Harrison, D., Driscoll, S., & Kitchen, M. (2000). Improving precipitation estimates from weather radar using quality control and correction techniques. Meteorological Applications 6, 135-144.*
- *Maruri, M., Etxezarreta, A., Aranda, J., Martija, M., Iturrirxa, E., Eguiara, I., . . . Gaztelumendi, S. (2014). Study on Radar Signatures of Hail in the Basque Country. ERAD 2014-THE EIGHTH EUROPEAN CONFERENCE ON RADAR IN METEOROLOGY AND HYDROLOGY (pág. 10). Garmisch-Partenkirchen: Proceedings.*
- *Osródka, K., & Szturc, J. (2022). Improvement in algorithms for quality control of weather radar data (RADVOL-QC system). Atmospheric Measurement Techniques, 261-277. doi:<https://doi.org/10.5194/amt-15-261-2022>*
- *WMO. (2014). WMO GUIDE TO METEOROLOGICAL INSTRUMENTS AND METHODS OF OBSERVATION. (the CIMO Guide). WMO-No. 8 (2014 edition, Updated in 2017). Geneva: WMO. Obtenido de <https://community.wmo.int/activity-areas/imop/cimo-guide>*
- *Zhang, J., Youcun, Q., Langston, C., & Kaney, B. (2011). Radar Quality Index (RQI) – a combined measure for beam blockage and VPR effects in a national network. Weather radar and Hydrology, 6.*

MONITORING BRIGHT GROUND CLUTTER TARGETS IN THE CANADIAN WEATHER RADAR

Norman Donaldson¹, Daniel Michelson¹

July 26, 2022

¹King Weather Radar, Environment and Climate Change Canada, Toronto, Canada

ABSTRACT

Strong ground clutter targets can provide signals related to radar performance. Rinehart (1978) is one of the most cited early proponent of using such targets to monitor changes in radar calibration. A number of studies, such as Silberstein (2008) and Wolff et al (2015), have proposed increasingly sophisticated methods for monitoring calibration with ground clutter, often referred to as relative calibration adjustment (RCA). Typically, results have been presented for only a few radars. Here a slightly less sophisticated tool, spun off from a pre-existing statistical study, looks at bright clutter targets across the operational Canadian Weather Radar Network. The returns from clutter in a specific radar sample area should remain constant provided four things do not change over time: the target(s), the illumination of the target(s), the radar electronics, and the radar processing. If any three are constant, one can monitor changes in the fourth. In this exploratory study, monthly statistics of echoes around a radar were used to find relatively steady strong targets around that radar and then the mean properties of this collection were monitored over several years. One main difference from most of the previous studies was that larger distances were used, because many radars had too few targets within 10-15 km. The study shows that diurnal and seasonal variations in illumination were a significant source of variability in the target collections used, with the variability itself changing between climate regimes. The results suggest operational implementation of clutter monitoring across a continental scale radar network can be problematic

1. INTRODUCTION

Environment and Climate Change Canada (ECCC) is in the final stages of its Canadian Weather Radar Replacement Program (CWRRP), which features a change from a diverse collection of C-band weather radars to a uniform network of S-band dual polarization radars. This has led to a desire to monitor the ongoing quality of the data from the new network. The radars themselves have massively improved built-in test equipment (BITE) but there is still a need for methods based on final data reported in output files. For example, BITE essentially ends before the antenna so there is no direct way to assess pointing errors with hardware nor can it detect

issues resulting from sampling and signal processing. Three methods have been explored to monitor on-going radar performance from output data: 1) detection of the sun in operational scans, based on a variation on the method of Huuskonen et al (2016) 2) monitoring of differential reflectivity in light precipitation, similarly to Zittel et al (2014) and 3) monitoring of returns from ground clutter. The first two methods are fairly well established and seem to be working well. For example, reported pointing biases in solar data have been followed up with on-site antenna calibrations that verified and corrected the biases. This work discusses the exploration of the possibilities for monitoring changes in radar calibration based on reported reflections from ground clutter targets. Rinehart (1978) is probably the most cited early proponent of using such targets to monitor changes in radar calibration. A number of studies, such as Silberstein (2008) and Wolff et al (2015), have proposed increasing sophisticated methods for monitoring calibration with ground clutter, often referred to as relative calibration adjustment (RCA). RCA monitors the high end of the cumulative distribution function of echoes from a collection of targets at a given time. The approach here is simpler and monitors the deviation of reflectivity from individual strong targets relative to a reference reflectivity for each target. It is worth noticing that the objective of the monitoring at this time is to detect long-term trends in the radars' performance, and not to attempt scan-by-scan corrections as some teams have done.

2. DISCUSSION OF CLUTTER ECHOES

2.1 UNDERLYING IDEA

The underlying idea behind monitoring ground clutter is to monitor changes in reflectivity from a static reference. Unlike the monitoring of solar data, this test involves both the receive and transmit sides of the radar system. On the other hand, the method can only detect changes, since the absolute values of reflectivity from ground clutter have no particular meaning.

2.2 COMPLICATIONS AND LIMITATIONS

The reported reflectivity from a specific clutter target will only be constant if several factors are themselves constant. The four primary factors are 1) the target's radar cross section, 2) the illumination of the targets, 3) the radar electronics, and 4) the radar signal processing. If any three are constant, one can monitor changes in the fourth. For radar monitoring, constancy of processing is controlled, and the primary desire is to assess the electronics changes. The illumination factor includes antenna pointing so interpretation of any changes includes crosschecking the solar pointing results. Illumination of the target involves a number of other sub-issues including beam width, atmospheric refraction and masking of the target by things like vegetation and precipitation. An objective of this study was to try to assess to what degree these different factors can be unravelled. Changes in antenna pointing can be due to actual biases arising in the antenna's hardware and can be crosschecked against solar pointing assessments. In addition to pointing biases in the hardware, there is a question of reproducibility. At many of ECC's older C-bands the antenna controllers did not do a good job of settling on the requested elevation angles and monitoring of clutter constancy was dismissed on this basis alone. Constancy of azimuthal pointing becomes more critical as antenna beam width narrows. With the narrower 0.67° beams in the C-band network this was more of an issue than for the new 0.87° beams, and all indications

are that azimuthal pointing has been very consistent with the new radars, although solar data at one radar do suggest small changes. Variability of masking of the target also needs to be considered. Attenuation by precipitation is a known factor in all weather reflectivity measurements and can be identified quite reliably from data between the radar and the target. Deciduous trees around the radar or the target have potential to make seasonal changes to the radio energy getting to and from a target. When temperatures are near freezing build-up of wet snow on radomes is another known issue with Canadian radars. The reflectance of targets themselves could also be affected by wetting or snow build-up. Changes in the height of the centre of the beam when it reaches the target is a significant concern, especially if a target is being illuminated by the edges of the radar beam where angular gradients of the gain are large. Large changes in the near surface profile of atmospheric refractivity can result in massive changes in distant targets, but even targets near the radar can be affected. Changes in the targets themselves are possibly the least important factor for this study. Almost all of the targets that were selected in the analysis were man-made, such as communication towers and farm silos. These tend to have binary changes, due to construction or removal. One minor consideration is whether the selection of bright targets very close to the radar might saturate the radars' receivers. More generally, the analysis of echoes from strong targets assumes that the receiver outputs are linear in received power so the results apply to echo powers more typical of precipitation. Neither issue seems to apply to the ECCC S-band radars but more careful assessment is required. The final, non-trivial complication is the availability suitable targets in sufficient numbers to do meaningful statistics. In the ECCC weather network the number of targets selected in this study varied from hundreds at some radars to a hand-full at others. The current study is intended to provide a preliminary assessment of how these complications would express themselves on a continental scale across the new Canadian weather radar network.

3 MONITORING OF BRIGHT CLUTTER TARGETS

3.1 TARGET SELECTION

The first step in the analysis procedure is to select targets. The objective is to find strong targets that will not be significantly affected by additional reflectivity from transient targets like precipitation or migrating birds. An on-going analysis of radar output builds monthly distributions of corrected and uncorrected horizontal reflectivity reported for each ray (azimuth) and range bin. A reference period of two or three months was selected for each radar. Bins were selected where 99 percent of reflectivity values were above 50 dbZ for an entire month, within of 20 km of the radar. The lowest common elevation sweep of the S-band network, 0.4°, was used for the clutter selection and analysis. Past experience with strong echoes shows that some can arise from highly variable targets like traffic on highways, so an additional restriction was placed on the inter-quartile range. Once a target was selected, its median reflectivity for the month was recorded. The result of clutter selection is a list of (range, azimuth) locations with their median reflectivity. The technique does not produce identical results from month to month, with differences in both selected points and median reflectivities. Taking this in mind, the final reference list was built by concatenating results from two or three reference months to give a list with most locations appearing multiple times from each of the initial monthly analyses.

3.2 DATA EXTRACTION AND PRELIMINARY PROCESSING

Given the reference list of clutter locations, scans were analyzed once per hour since the beginning of 2020. A dedicated extraction program finds the uncorrected reflectivity at each location in the reference list and calculates the difference from the reference reflectivity. There is a crude rejection test for rain attenuation. If more than four intervening bins have high co-polar correlation coefficient ($\rho_{hv} > 0.8$) and corrected reflectivity above 20 dBZ then that difference is not considered in subsequent calculations. Although the initial selection of clutter locations went to a maximum range of 20 km, a shorter range can be specified at this point. At each time, the average difference is calculated. The variability of this average across time and geography is the primary subject of the current study.

3.3 ANALYSIS

Analysis was in the form of temporal plots. At a given radar the calculated hourly differences were plotted as hourly points for a year or month. A more easily interpreted summary display of annual data was box-and-whisker plots that summarize the median and range of the data month by month. Since diurnal variations were present at some radars, the data from individual months at each radar were also plotted as hourly box plots. For the box plots all the observations at a given hour of the day were collected for the entire month and plotted.

4 RESULTS

4.1 OVERVIEW

Dozens of plots were created and inspected visually. It was immediately obvious that the most changes of reflectivity from the reference state occurred during servicing at the sites, due to changes of reflectivity calibration or changes to antenna pointing. Some radars produced results with quite constant differences from the reference state between known hardware changes, while others produced changes that have yet to be explained.

4.2 ANNUAL PLOTS

Annual plots of the difference from the reference show that a) some radars are quite steady, such as CASBV in Fig 1, b) some seem to have a reasonably constant difference but with a large number of deviation at scales from hours to weeks, see CASSU in Fig 2, and c) some have trends that have not yet been explained, for example CASET in Fig 3. One obvious feature in the plots is occasional jumps caused during servicing at the radars. Servicing usually involves adjusting both calibration and pointing offsets after work is completed. For example, at CASSU (Fig 2) in late July 2021 the technical staff were trying to resolve an issue with ZDR and solar data suggest a slight change in azimuthal pointing also resulted. The cumulative effect was a change of 4 dB with respect to the reference.

Figure 1
Average of difference of uncorrected reflectivity from the reference. Radar CASBV data each hour for 2021.

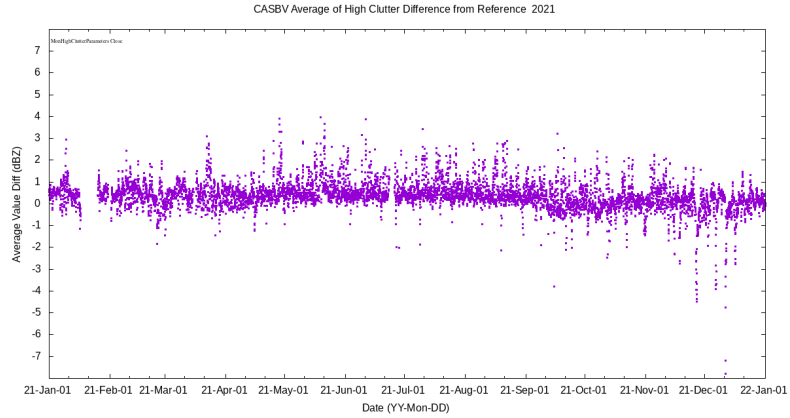


Figure 2
Average of difference of uncorrected reflectivity from the reference. Radar CASSU data each hour for 2021.

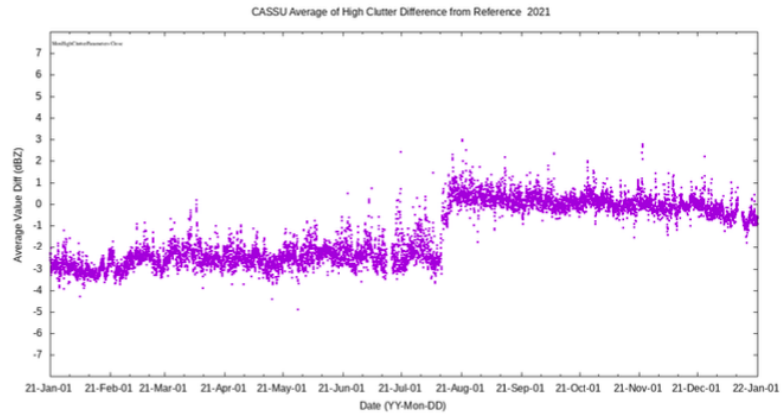
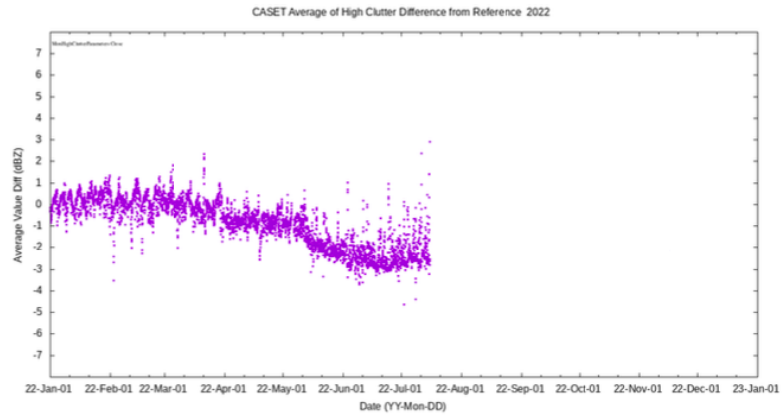


Figure 3
Average of difference of uncorrected reflectivity from the reference. Radar CASET, data each hour for 2022.



4.2 DIURNAL PLOTS

It was obvious early in the analysis that there was some diurnal "signal" in the differences during some periods. Fig 4 shows box-and-whisker plots of average difference from the reference for January and August 2021 at the CASET radar by hour of the day. In winter there is little diurnal variation but in August the difference are much more variable at night (00-11 UTC) with largest value occurring slightly after dawn. This radar is in farm country between the Great Lakes and is known for having anomalous propagation around dawn in summer. In contrast, CASDR, Fig 5, is a northern radar with no large bodies of water nearby and it shows relatively little diurnal variation in summer or winter. Some experiments, not shown, were undertaken to restrict the maximum range of the analysis at radars with large numbers of targets, with the thought that "beam bending" would be more important at longer ranges. Changing the maximum analysis range from 20 km to 10 km did reduce the overall variability of the differences but the summertime diurnal trend was still present.

Figure 4
Box plots of differences from reference, organized by hour for CASET radar. Left January 2021 and right August 2021.

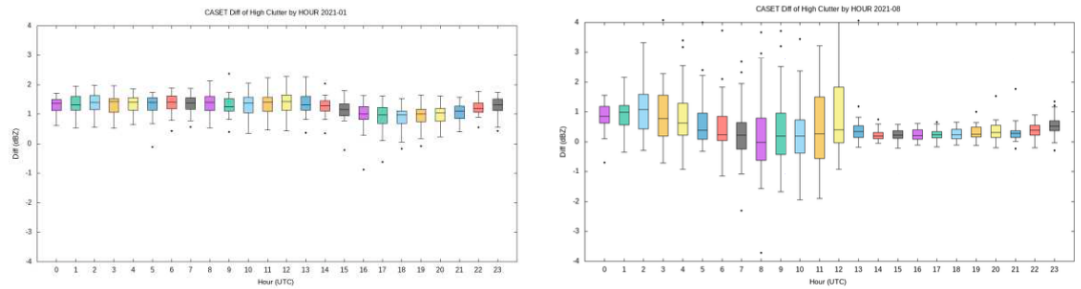
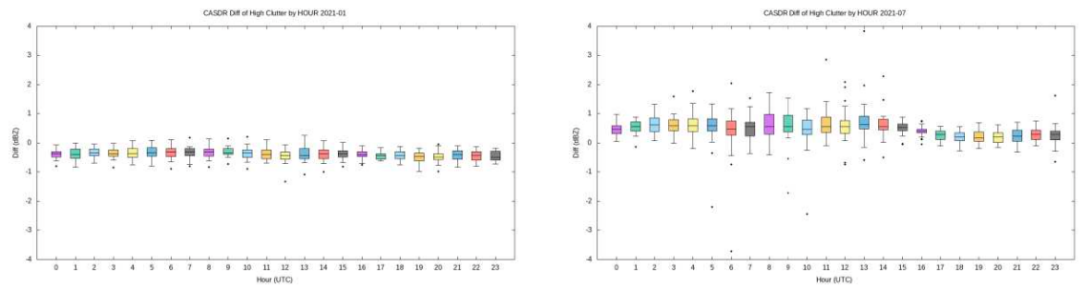


Figure 5
Box plots of differences from reference, organized by hour, for CASDR radar. Left January 2021 and right July 2021.



5. CONCLUSIONS

This study was an exploratory assessment of the feasibility of monitoring radar calibration changes across the Canadian Weather Radar Network using strong clutter targets. The preliminary conclusion is that the clutter monitoring method described is not suitable for monitoring radar calibration in the Canadian weather radar network as whole. Some radars seem to work well, but at the opposite extreme, some very rural radars have too few suitable targets to generate reliable statistics. The constancy of clutter varied seasonally across the network, with higher diurnal variability in summer at radars in climates where larger changes in the low-level refractivity profile are expected. It is possible that a more sophisticated method such as RCA (Wolff et al, 2015) would give more consistent results, but it is not yet clear whether that would be the case for all radars. The small number of selected clutter locations at many radars could be improved somewhat by selectively loosening the clutter selection criteria, but in very rural locations most of the potential targets are already being selected. Possibly the greatest hindrance to using the method is successfully eliminating the potential complicating factors as sources of change in reported reflectivity from strong ground clutter targets. A large drift of the average clutter reflectivity should cause staff to double check that issues are not being reported in BITE and solar data, but if those do not show indicate issues, it is unclear how to isolate radar changes from external changes. With reference to past studies, the results in this test of concept study seem to be better in situations that more closely resemble those in reported successful studies, such as numerous man-made targets scattered uniformly, close to the radar. Other radar sites in the ECCC network without many of those targets were more problematic. Anecdotally, other teams have had mixed results using clutter to monitor reflectivity, and this study hints that this is could be related to the local clutter regime, both in terms of targets and changes in illumination of those targets. For the ECCC operational network a clutter search range of 20 km failed to find enough suitable targets at many radars and only a few had enough targets within 10 km. For comparison, Borowska and Zrnić (2012) found enough clutter targets for their study within 7 km of the Norman, OK, USA, radar but needed to use 20 km for another radar near Bonn, Germany.

ACKNOWLEDGMENTS

The authors would like to acknowledge Environment and Climate Change Canada for funding this work. Input from Sudesh Boodoo, Stephen Holden and Qian Li was very valuable.

REFERENCES

- Borowska, L., and Znić D.: Use of ground clutter to monitor polarimetric radar calibration. *J. Atmos. Oceanic Technol.*, 29, 159–176. <https://doi.org/10.1175/JTECH-D-11-00036.1>, 2012
- Huuskonen, A., and I. Holleman: Improved analysis of solar signals for differential reflectivity monitoring. *Atmos. Meas. Tech.*, 9, 3183–3192. <https://doi.org/10.5194/amt-9-3183-2016>, 2016
- Rinehart, R. E.: On the use of ground return targets for radar reflectivity factor calibration checks. *J. Appl. Meteor.*, 17, 1342–1350. [https://doi.org/10.1175/1520-0450\(1978\)017<1342:OTUOGR>2.0.CO;2](https://doi.org/10.1175/1520-0450(1978)017<1342:OTUOGR>2.0.CO;2), 1978.
- Silberstein, D. S., Wolff D. B. , Marks D. A. , Atlas D. , and Pippitt J. L.: Ground clutter as a monitor of radar stability at Kwajalein, RMI. *J. Atmos. Oceanic Technol.*, 25, 2037–2045. <https://doi.org/10.1175/2008JTECHA1063.1>, 2008
- Wolff, David B., Marks, David A., and Petersen, Walter A.: General Application of the Relative Calibration Adjustment (RCA) Technique for Monitoring and Correcting Radar Reflectivity
- Calibration, *Journal of Atmospheric and Oceanic Technology* Vol. 32, No. 3, pp 496, 1520-0426 <https://doi.org/10.1175/JTECH-D-13-00185.1>, 2015
- Zittel, W. D., J. G. Cunningham, R. R. Lee, L. M. Richardson, R. L. Ice, and V. M. Melnikov, 2014: Use of hydrometeors, Bragg scatter, and sun spikes to determine system ZDR biases in the WSR- 88D fleet. Extended Abstracts, Eighth European Conf. on Radar in Meteorology and Hydrology (ERAD 2014), Garmisch-Partenkirchen, Germany, DWD and DLR, DAC. P12, 2014



HYDROLOGICAL APPLICATIONS

A flash flood warning system for ungauged basins in the tropical context of Reunion island





A FLASH FLOOD WARNING SYSTEM FOR UNGAUGED BASINS IN THE TROPICAL CONTEXT OF RÉUNION ISLAND

Pierre Javelle¹, Didier Organde², Julie Demargne², Philippe Cantet², Maxime Jay-Allemand², Anthony Roulenq³,
David Villani³, Florent Baby³, Claire Latestere³, Pierre-Andre Garambois¹

August 2, 2022

¹INRAE-RECOVER, Aix-Marseille University,
Aix-en-Provence, France

²Hydris-hydrologie, Montferrier-sur-Lez, France

³DEAL Re union/SPRINR/CVH, La Re union,
France

ABSTRACT

To better anticipate flooding events on the French island of La Reunion (Indian Ocean) and help mitigate damages, the French environmental agency of la Reunion (DEAL Reunion) is currently developing a flash flood warning system for small-to-medium ungauged basins (with a catchment area from 8 to 220 km²). The system is based on a conceptual distributed model called SMASH (Spatially-distributed Modelling and ASsimilation for Hydrology, Jay-Allemand et al, 2020), run at a 250-m spatial resolution and a 15-min time step. The flow simulations are estimated in real-time by ingesting high-resolution radar-gauge rainfall grids produced by Meteo-France (product called ANTILOPE). The comparison of these discharges with reference flood quantiles (defined for different return periods) leads to identify real time maps of potential flooding. This communication aims to present the methodology developed to set up the warning system, and the first results obtained in real time during the 2021-2022 tornado season. Interests and limits of the current warning system will be discussed, as well as future planned operational enhancements.

1. INTRODUCTION

Flash floods are typically triggered by severe rainfall events, and their early detection is still challenging due to large meteorological and hydrologic uncertainties at fine spatial and temporal scales (Borga et al., 2010). In the meantime, it is predicted that flood-related impact will significantly increase by the end of the century (Alfieri et al., 2015). In this context, radar-based warning systems can help authorities to better anticipate Flash flood and reduce their impacts (Creutin and Borga, 2003; Collier, 2007). The present communication aims at presenting the flash flood system warning currently implemented by the authorities in charge of flood warning at the Reunion island. Those developments are in relation with the flash flood warning system previously developed in France (Javelle et al., 2016). The Reunion island has an area of 2 512 km² and is located in the Indian Ocean. Its highest point culminates at 2 632 meters. Extreme rainfall are regularly observed, with an annual total amount above 8 000 mm/year on its most exposed east side.

2. DATA AND METHODS

2.1 DISTRIBUTED MODELLING WITH SMASH

SMASH is a computational software framework dedicated to Spatially distributed Modeling and data ASSimilation for Hydrology, enabling to tackle high dimensional inverse problems with adjoint-based variational method, developed by Jay-Allemand et al. (2020). This modular platform contains conceptual representations and numerical approximations of dominant hydrological processes while aiming to maintain a relative parsimony. SMASH works on a regular grid and runs continuously. For each time step, it takes as inputs rainfall and potential evapotranspiration grids, and outputs a field of routed discharges following a drainage grid. As shown by Fig. 1, the model structure tested in this work has 4 components per cell: a production store, two transfer stores (for slow and rapid flow) and a simple cell to cell routing scheme to convey the discharge downstream. The production and transfer stores are similar to the stores implemented in GR4J model (Perrin et al., 2003), while the routing store is a simple linear reservoir. After different tests to better cope with specificities of Reunion island, the model has been adapted to a 15-min time step and a 250-m spatial resolution. Furthermore, it has been added a leaking function from the production reservoir. Finally, five parameters per cell have to be calibrated: C_p , β , C_{tr} , α and C_r .

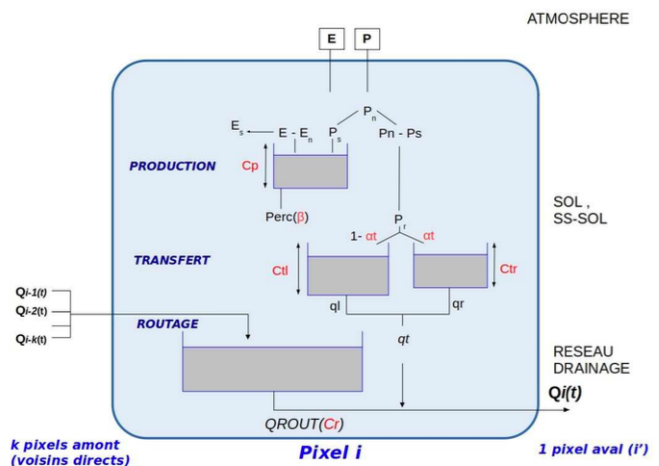


Figure 1
Model structure tested

2.2 FORCING DATA AND TIME PERIOD

The forcing data is constituted by a radar product called ANTILOPE-15MN made available by Météo France for the 2015-2021 period. This product merges in real time quantitative precipitation estimates (PQE) obtained from 2 radars located on the island, and rain gauges. Potential-Evapo-transpiration (PET) is also used as input by the model. Those grids are simply obtained from inter-annual interpolated values in order to simplify the operational chain.

2.3 REGIONAL CALIBRATION

In this study, 5 parameters per cell are calibrated over the 2015-2021 period: C_p , β , C_{tr} , and C_r . To reduce the dimension of the problem, it was considered in a first approach to impose uniform parameters per hydrological areas. Six hydrological station groups have been defined on expert considerations and represented on Fig. 5. Note that to improve the robustness, stations can be including in two different group.

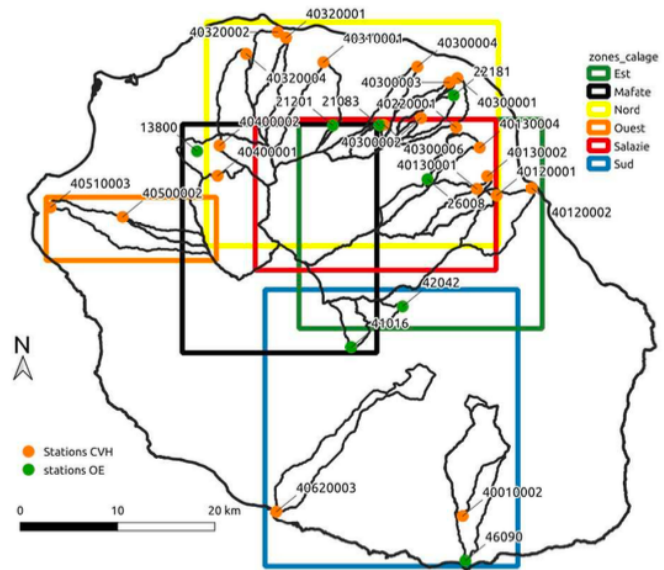


Figure 2
Hydrological station grouping for regional calibration

3. RESULTS

3.1 MODEL CALIBRATION ON GAUGED STATIONS

Tab. 1 indicates the calibrated parameters for each hydrological group. Different performance criteria have been considered. Contingency scores, such as the POD (probability of detection), SR (success rate), CSI (critical success index) is well suited for threshold detection. Scores of Tab. 2, for example, assess to the ability of the model to detect a 2-year threshold (ie the flood having each year one chance over two to be exceeded). Result are quite good and similar on all the groups, except in the South where a lot of false alarms are observed (SR=0.5).

Group	Cp (mm)	alpha	Ctr (mm)	beta
Nord	1580	0.43	104	/
East	4035	0.52	86	/
Salazie	1309	0.32	115	/
Mafate	2021	0.42	97	/
West	480	0.6	1	2.4
Sud	4075	0.9	58	5.8

Table 1
Model uniform parameters per hydrological group.

Group	POD	SR	CSI	Nb of events
Nord	0.8	0.7	0.6	79
East	0.7	0.8	0.6	41
Salazie	0.8	0.7	0.6	14
Mafate	0.8	0.8	0.6	38
West	0.9	0.6	0.6	17
Sud	0.8	0.5	0.4	10

Table 2
Contingencies scores per hydrological group: POD (probability of detection), SR (success rate), CSI (critical success index) and number of events (one event is defined when the observed peak discharge is greater than 2-year)

3.2 TOWARD A QUALITATIVE REAL-TIME EVALUATION OF THE IMPACTS

Based on the developed model described in the previous sections, a real time flash flood monitoring system has been made operational for the 2021-2022 cyclonic season. The system interface, called CartoSMASH is presented Fig. 3. It enables the model to be run in real time, with different futures rainfall scenarios: zero future rainfall (PPo), constant future rainfall (PPC), and AROME prediction Batsirai is the most important cyclone observed this 2021-2022 season on the Reunion island. It has impacted the island between the 2 and 4 February 2022. More than 1 500 mm of precipitation were observed on the Piton de la Fournaise, with wind exceeding 150 km/h. Even if no casualties were identified, many impacts were reported on infrastructure networks (road, electricity, water...). Fig. 4 presents a comparison of the total QPE measured in real time by Meteo-France (right) and a post-event estimation (left). It can be observed some small differences, also observable in Fig. 5 showing the maximal hydrological qualification by the system during the event (hazard expressed in term of flood peak return). Analysis is still on-going to compare this hazard map with impacts on the field. The idea is to create a damage database using past events, enabling to establish a relation between impact and hazard on different places of the island (called "site of interest").

Figure 3
Operational system
made available for the
2021-2022 season
(CartoSMASH)

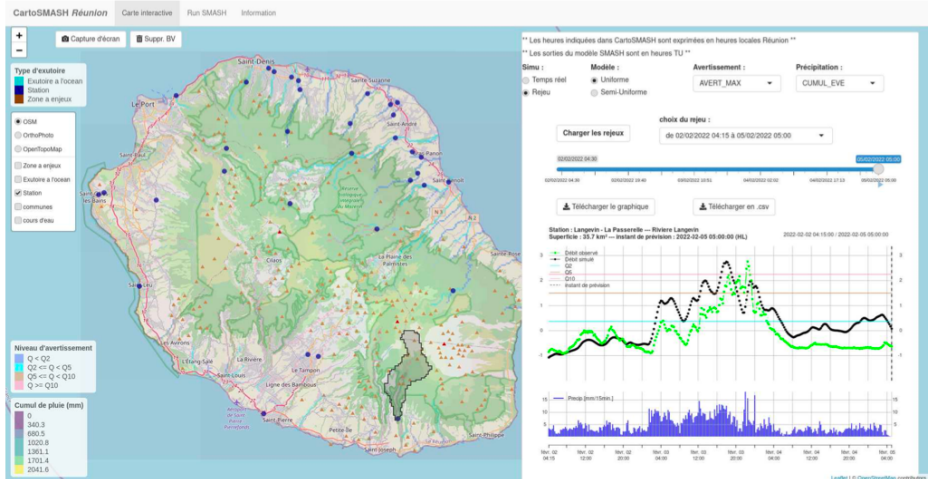


Figure 4
Comparison between
the post-event (left)
and real time (right)
ANTILOPE QPEs
during the cyclone
Batsirai (2-4 Feb. 2022)

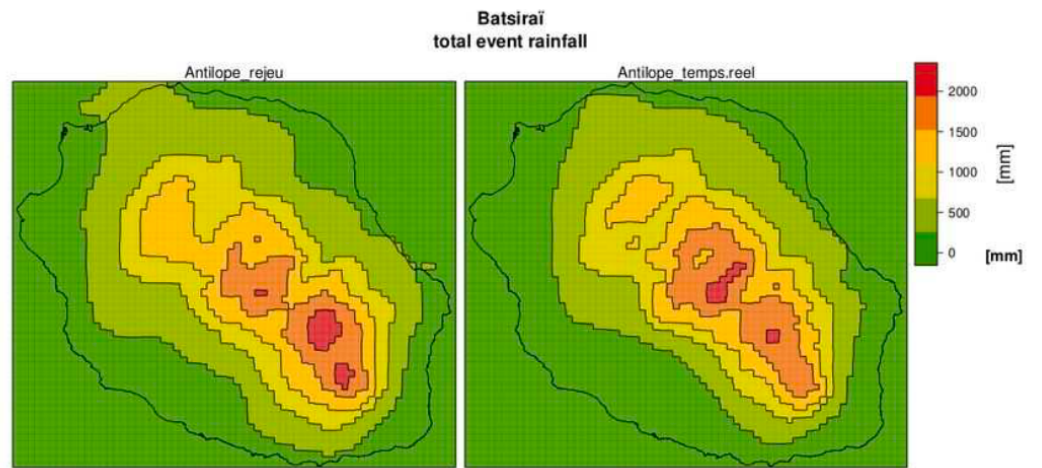
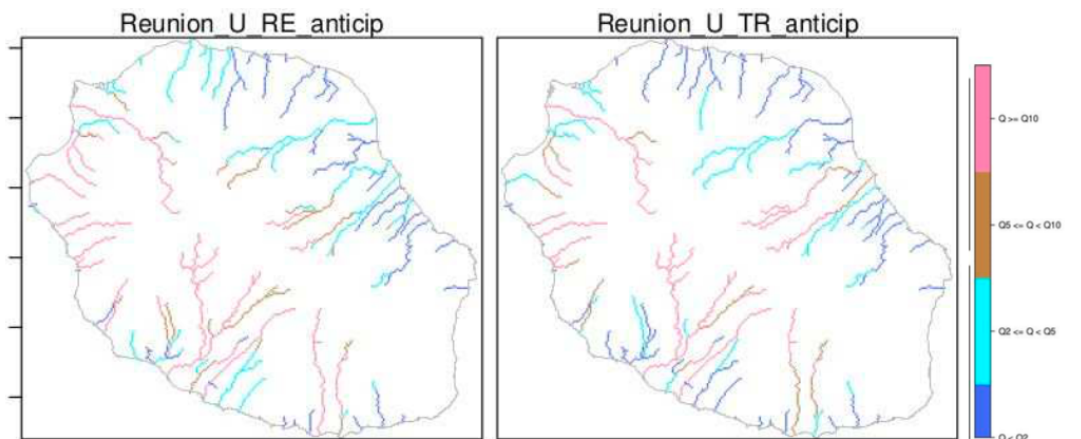


Figure 5
Comparison between
the post-event (left)
and real time (right)
SMASH hazard maps,
ex- pressed in return
period (2, 5, 10-year),
during the cyclone
Batsirai (2-4 Feb. 2022)



4. DISCUSSION AND CONCLUSIONS

As presented in this short paper, the flash flood warning system first tested in real time on the Reunion island for the 2021-2022 season demonstrates a real progress, since authorities has now flood hazard estimations on rivers not covered by hydrometric gauges. Nevertheless some points need to be further investigated.

- First, the question of evaluation on un-gauged location is crucial, since it will provide guidelines to improve the model regionalisation. Observed impacts are a good way to collect "proxy" information on the flood intensity. This information needs to be collected in a geo-referenced data base, for past and future events, as it is currently done on the Reunion island by the DEAL.
- A second point to be mentioned is that the method is only based on hazard estimation. This is a first step, but to be fully efficient, it needs to also provide information on predicted impacts. Impact models to be developed has to be "simple" to be operational in real time. They can be "local" and based only on past observation, if available. But they could also include simplified hydraulic modelling and validated using the impact database described in the previous point.
- A last point to improve, is the forecasting capabilities. In particular, nowcasts must be developed, merging radar observation and numerical weather models, as it is already done in other systems (STEPS for instance).

REFERENCES

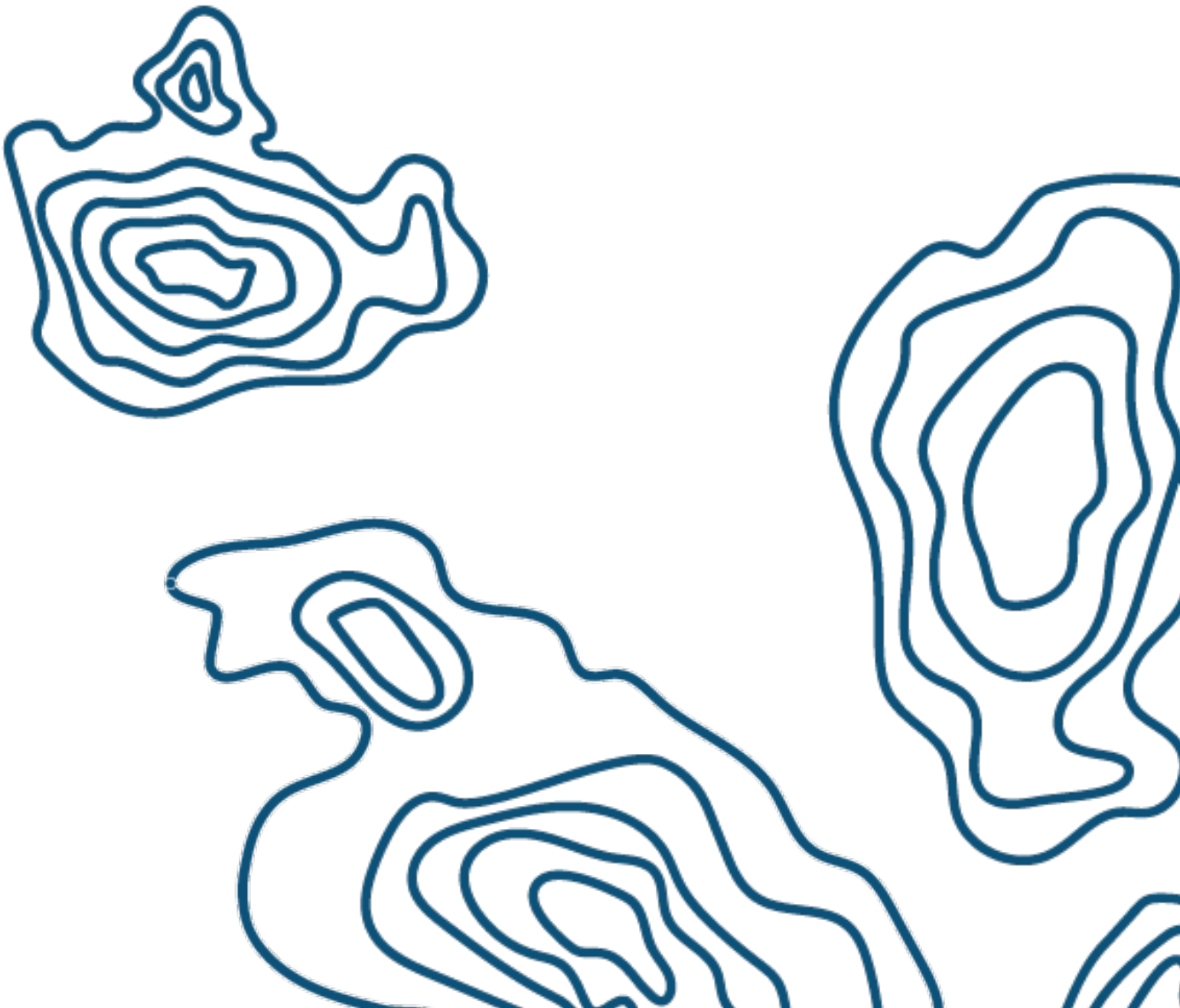
- Alfieri, L., Burek, P., Feyen, L., and Forzieri, G.: Global warming increases the frequency of river floods in Europe, *Hydrology and Earth System Sciences*, 19, 2247–2260, <https://doi.org/10.5194/hess-19-2247-2015>, 2015.
- Borga, M., Anagnostou, E., Blošchl, G., and Creutin, J.-D.: Flash floods: Observations and analysis of hydro-meteorological controls, *Journal of Hydrology*, 394, 1–3, <https://doi.org/10.1016/j.jhydrol.2010.07.048>, 2010.
- Collier, C.: Flash flood forecasting: What are the limits of predictability?, *Quarterly Journal of the Royal Meteorological Society*, 133, 3–23, <https://doi.org/10.1002/qj.29>, 2007.
- Creutin, J.-D. and Borga, M.: Radar hydrology modifies the monitoring of flash-flood hazard, *Hydrological Processes*, 17, 1453–1456, <https://doi.org/10.1002/hyp.5122>, 2003.
- Javelle, P., Organde, D., Demargne, J., Saint-Martin, C., De Saint-Aubin, C., Garandeau, L., and Janet, B.: Setting up a French national flash flood warning system for ungauged catchments based on the AIGA method, in: *E3S Web of Conferences*, vol. 7, <https://doi.org/10.1051/e3sconf/20160718010>, 2016.
- Jay-Allemand, M., Javelle, P., Gejadze, I., Arnaud, P., Malaterre, P.-O., Fine, J.-A., and Organde, D.: On the potential of variational calibration for a fully distributed hydrological model: application on a Mediterranean catchment, *Hydrology and Earth System Sciences*, pp. 1–24, <https://doi.org/10.5194/hess-24-5519-2020>, 2020.
- Perrin, C., Michel, C., and Andre`assian, V.: Improvement



NOWCASTING OF CONVECTION AND THUNDERSTORMS

Meteorological Algorithm Requirements for Disaster Early Warning and Decision Support

Using Dual-Polarization Radars to Nowcast Severe Weather Events





METEOROLOGICAL ALGORITHM REQUIREMENTS FOR DISASTER EARLY WARNING AND DECISION SUPPORT

Emre Çiftçi¹, Yücel Özdemir¹, Ergenekon Hassoy¹, Murat Başaran¹

March 21, 2022

¹RST Inc, Ankara, Turkey

ABSTRACT

In this paper, meteorological algorithm requirements currently under development for Disaster Early Warning and Decision Support studies in the concept of weather radars are described, along with the design and implementation issues on the polarimetric X-Band radar system, namely Turkish METRAD system.

1. INTRODUCTION

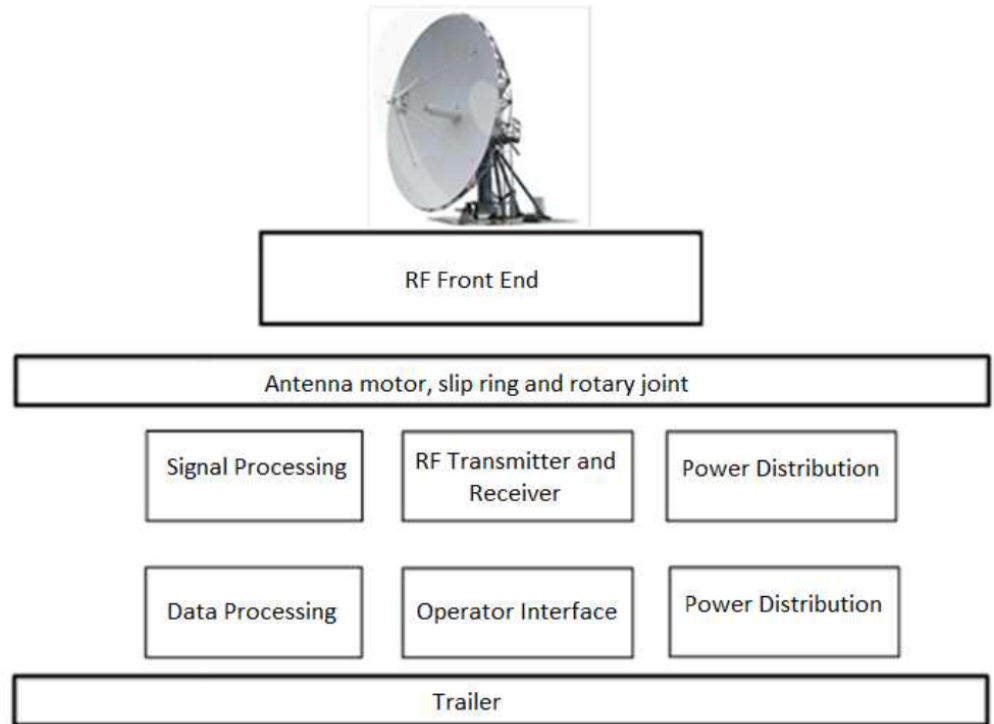
RST Inc, established in 2012 is a technology developer company for radar, RF and electronic warfare systems. Company specializes in system, hardware and software engineering for system and sub- system design, test equipment and consultancy. METRAD System is the X band polarimetric weather radar developed under governmental support and named as national weather radar in Turkey. System provides the user with raw moments of meteorology regime such as reflectivity and velocity which are produced from digital I/Q data produced by Signal Processing Unit from the received x-band radar signal reflections. Meteorological regime products to be used in emergency hazard detection and prevention are produced from these raw moments.



Figure 1
Transportable METRAD System

2. METRAD SYSTEM

Figure 2
METRAD System
Components



The hardware supplies the signals to custom developed signal processor cards shown in Figure 3, which transform the signals to base meteorological moments and then makes the following meteorological products available in METRAD user interface, as listed in tables below, as defined by Chandarsekar (2004) and Zhang (2016).

Base Moment	Moment Description
Z	Reflectivity (clutter corrected)
T	Total Reflectivity (not clutter corrected)
ZDR	Differential Reflectivity
Vel	Radial Velocity
Width	Spectral Width
∅DP	Differential Phase Shift
KDP	Specific Differential Phase
TV/ZV	(Total) Reflectivity in vertical channel

Table 1
Calculated Meteorological Base Moments after Signal Processing

Meteorological Product	Product description
PPI	The rate of precipitation received by horizontal scanning (reflectivity)
CAPPI	The amount of precipitation at a certain height
PCAPPI	The amount of precipitation at a certain height (with interpolation for regions with no signal)
MAX	The height with the heaviest precipitation, on the vertical axis for each coordinate
VIL	The total amount of precipitation between the two heights
RHI	The rate of precipitation of all elevation levels, received by a vertical scan

Table 2
Validated Meteorological Products in METRAD System

For validation of METRAD algorithms, we have performed many tests in the field, especially near the General Directorate of Meteorology (MGM) site in Elmadağ, Ankara. Transportable METRAD system is left for operation for months at Elmadağ radar site, and the data obtained is compared with MGM live radar data on the web. Results from standard C-band radars and METRAD are similar, with METRAD giving much more in depth meteorological information as it is operating at a higher frequency band, namely X-band.

3. NEW METEOROLOGICAL RADAR REQUIREMENTS FOR DISASTER EARLY WARNING

RST has performed years of hard work on developing the transportable meteorological solution. In the first phase of project, system hardware and meteorological baseline is established. Second phase added advanced software capabilities to METRAD System, most of which was a success. These advanced software algorithms are operational in X-band METRAD System, as of 2021. METRAD system is in a third phase of development as of 2022, in which phase disaster early warning capabilities and decision support tools for disaster teams are being added to the system. "Seeing the wind" as performed by <https://uubf.itu.edu.tr/akademik/meteoroloji-muhendisligi> is necessary for emergency early detection and decision support, but also in near future we will add capabilities as explained by John Y. N Cho, Robert G. Hallowel, Mark E. Weber explained (2008), as also defined in MGM Requirements (2017). Detection of the smoke plumes caused by grass fire, brush fire, and forest fire to locate the flame center of emergency fires is key to fire hazard early detection and elimination. Detection of dense clouds as well as the calculation of flood risk of clouds from a medium distance is also of utmost importance for flood warning systems. The system not only gives alerts for fire/flood events, but also tries to give decision support to emergency teams about the regions where the disaster can spread with the radar's wind vision. Decision support helps emergency teams with firefighting location suggestions protecting team from dangers of fire spread. Alerting new flood events while the emergency teams are in the area can be taken as a similar system capability for flash flood events.

4. CONCLUSIONS

In this third phase of our system development, we are currently adding wind visualization to the system. With artificial intelligence, meteorological algorithms are not only enabling emergency early detection but also "seeing" the wind and knowing the digital map vegetation/urbanization/flood map details, system can "predict" the areas that the fire/flood will spread, which alerts emergency firefighting and flood rescue teams for near future dangers of emergency event, which will save many lives. The capabilities currently added to the system are listed below.

- Precise wind detection and visualization
- Early warning and emergency detection algorithms
 - o Forest and agricultural fires early warning (smoke detection)
 - o Flood prediction and early warning (algorithm design suppresses noise where rain starts/ends)
- Representation of all algorithm outputs on real land and sea maps
- Inter-changeable hydrometeor classification parameters
- Remote control of the system with standard software
- Ability to save screenshots / visual 3D radar display videos.

Also, one of the main objectives of this work is to ensure that meteorology engineers directly participate in algorithm design and development activities. For this purpose, a wide range of university-industry cooperation and remote access capabilities are planned for data recording and playback including scenario studies on laboratory hardware prototypes for software development.

ACKNOWLEDGMENTS

We hereby acknowledge all of the General Directorate of Meteorology (MGM) and the Disaster and Emergency Management Directorate (AFAD) personnel by giving us their support through years.

REFERENCES

- Chandarsekar V. (2004) *Polarimetric Doppler Weather Radar*
- G. Zhang (2016) *Weather Radar Polarimetry*
- John Y. N Cho, Robert G. Hallowel, Mask E. Weber (2008) *Comparative analysis of terminal wind- shear detection systems.*
- MGM (2017) *Antalya Havalimani LLWAS Requirements*
- <https://uubf.itu.edu.tr/akademik/meteoroloji-muhendisligi>

USING DUAL-POLARIZATION RADARS TO NOWCAST SEVERE WEATHER EVENTS

Charles M. Kuster^{1,2,3}, Jacob Carlin^{1,2,3}, Terry Schuur^{1,2,3}, Randy Bowers⁴, Todd Lindley⁵, Jeffrey Snyder², Jason Furtado³

August 30, 2022

¹Cooperative Institute for Severe and High Impact Weather Research and Operations, Norman, Oklahoma, United States

²NOAA/OAR National Severe Storms Laboratory, Norman, Oklahoma, United States

³University of Oklahoma, Norman, Oklahoma, United States

⁴NOAA/National Weather Service, Indianapolis, Indiana, United States

⁵NOAA/National Weather Service, Norman, Oklahoma, United States

ABSTRACT

Advancements in weather radar, such as dual-polarization capabilities, provide forecasters with new data to diagnose threats posed by thunderstorms. However, uncertainty remains in how these new data can explicitly be used by forecasters to inform warning decisions especially when so many factors compete for forecaster attention. Therefore, an analysis of multiple storm modes and hazards across severe and nonsevere thunderstorms was conducted to examine potential uses and benefits of dual-polarization data for anticipating hazardous weather. These analyses show that 1) Z_{DR} columns are stronger and larger for severe storms than nonsevere storms and develop earlier than -20°C reflectivity cores, 2) K_{DP} cores are a reliable downburst precursor that can increase confidence in predicting downburst development and provide some information about an impending downburst's intensity, and 3) K_{DP} cores and drops precede QLCS mesovortex development and K_{DP} cores are typically stronger for tornadic mesovortices than nontornadic ones.

1. INTRODUCTION

Advancements in weather radar, such as dual-polarization technology and rapid-updates provided by phased-array radar systems, can provide forecasters with additional information that can aid in issuing warnings and advisories for hazardous weather (e.g., Heinselman et al. 2008; Kumjian 2013; Van Den Broeke 2017). Potentially useful features include the differential reflectivity (Z_{DR}) column (e.g., Illingworth et al. 1987; Kumjian et al. 2014), Z_{DR} arc (e.g., Kumjian and Ryzhkov 2008a), and specific differential phase (K_{DP}) core (e.g., Kuster et al. 2021). However, despite the advances in technology, uncertainty remains on how to best apply the new data to real-time decision making. Are new data better or more useful than existing data? Is it worth incorporating new data into decision making especially when so many factors compete for forecaster attention? How can new data best be incorporated into existing scientific conceptual models that play a vital role in decision making (e.g., Andra et al. 2002)? Therefore, the purpose of this work is to examine potential benefits of dual-polarization features in short-term prediction of hail, downbursts, and tornadoes. Specifically, we use dual-polarization data from the operational radar network

in the United States as well as rapid-update data (i.e., volumetric update times of two minutes or less) collected by a research S-band radar (KOUN) in central Oklahoma to quantify the evolution of Z_{DR} columns and K_{DP} cores in severe (i.e., produces 2.5+ cm hail, 26+ ms⁻¹ wind, or a tornado) and nonsevere thunderstorms. We then compare this evolution to reports of severe weather and radar features forecasters typically use to make warning decisions (e.g., upper-level reflectivity cores, tornado vortex signature, etc.) to determine potential ways to incorporate new radar features into existing conceptual models.

2. DATA AND METHODS

Data were gathered for three different studies regarding Z_{DR} columns in severe and nonsevere thunderstorms, K_{DP} cores in downburst-producing thunderstorms, and dual-polarization features associated with quasi-linear convective system (QLCS) mesovortices. For the Z_{DR} column study, rapid-update data were collected using KOUN for 45 storms, of which 20 were supercells and 25 were single- or multicell thunderstorms. Z_{DR} column evolution was quantified using a Z_{DR} column depth algorithm (Snyder et al. 2015) and using base radar data that is currently available to forecasters during real-time operations (Kuster et al. 2020). For the K_{DP} core study, data were collected using KOUN, but the relatively small rapid-update dataset was supplemented with data from the operational radar network maintained by the National Weather Service. Of the 81 downbursts studied, KOUN data were used for 16 of them. K_{DP} cores ($K_{DP} \geq 1.0^{\circ}\text{km}^{-1}$) were quantified at elevation angles from the first above the environmental melting layer—height determined using a combination of observed soundings and radar observations—to the one closest to three km below the environmental melting layer. Evolution of magnitude, size (i.e., areal extent), and vertical gradients were then examined over time. For the QLCS study, data from the operational radar network was primarily used, though rapid-update KOUN data were collected for 5 of the 120 mesovortices studied (77 tornadic and 43 nontornadic). For all mesovortices, several dual- and single-polarization features were quantified using operationally-available base data, but here we focus on K_{DP} cores near the melting layer and at the 0.5° elevation angle, as well as a low-level feature called a K_{DP} drop.

3. Z_{DR} COLUMNS IN THUNDERSTORMS

Kuster et al. (2019, 2020) provides detailed results regarding Z_{DR} column evolution in severe and nonsevere thunderstorms and compares that evolution to -20°C reflectivity (Z) core and mesocyclone evolution. In summary, Z_{DR} columns are likely helpful to use when anticipating large hail and damaging winds because they are stronger and larger in severe thunderstorms compared to nonsevere thunderstorms. In addition, Z_{DR} columns tend to develop and intensify about 5–10 minutes prior to -20°C Z cores, which could give forecasters additional time to diagnose storm severity and potentially issue warnings a few minutes earlier. Rapid-update data is also important in observing Z_{DR} columns because it samples changes in Z_{DR} column strength earlier and provides a more complete picture of Z_{DR} column evolution including peaks in magnitude that tend to occur before reports of large hail and damaging winds.

4. K_{DP} CORES AND DOWNBURSTS

Kuster et al. (2021) provides detailed results regarding K_{DP} cores associated with wet downbursts across the southern and southeastern United States. In summary, K_{DP} cores are likely a reliable downburst precursor because K_{DP} cores preceded all 81 downbursts studied and had a consistent signal of developing and intensifying prior to downburst development. In addition, no null events (i.e., K_{DP} core near the melting layer with no near-surface downburst) were identified, though all cases were from days where environmental conditions were at least somewhat favorable for downburst development. Anticipating downburst intensity using K_{DP} cores appears more challenging as there is overlap between the distributions of K_{DP} core magnitude between strong (report of severe winds or max 0.5° radial velocity ≥ 23 ms $^{-1}$) and weak (no report of severe winds and max 0.5° radial velocity < 23 ms $^{-1}$) downbursts, but in general, stronger K_{DP} cores are more likely to be associated with a strong downburst. Combining environmental information with K_{DP} data also proves useful in that 1) differences in the distributions of K_{DP} core magnitude between strong and weak downbursts were greater when split out based on environmental parameters (e.g., low-level lapse rate), and 2) K_{DP} cores tended to be stronger in environments that were less supportive of downburst development (e.g., smaller low-level lapse rates), so a forecaster could adjust expectations for what K_{DP} magnitudes might be associated with a strong downburst based on environmental conditions. Based on feedback received from forecasters, additional work has been done since Kuster et al. (2021) to quantify Z_{DR} , correlation coefficient (phv), and Z within K_{DP} cores. When comparing vertical profiles of various radar variables between strong and wet downbursts, K_{DP} has the largest differences of all the analyzed variables (Fig. 1). There are few differences when looking at the other variables, though Z is somewhat higher in strong downbursts than weak ones (Fig. 1d), which provides additional evidence that K_{DP} could be the most helpful radar variable when diagnosing a storm's downburst potential.

Figure 1
Vertical profiles of a) K_{DP} , b) Z_{DR} , c) correlation coefficient, and d) reflectivity for strong (black line) and weak (red line) downbursts relative to the environmental melting layer (0 km on y-axis is melting layer height).

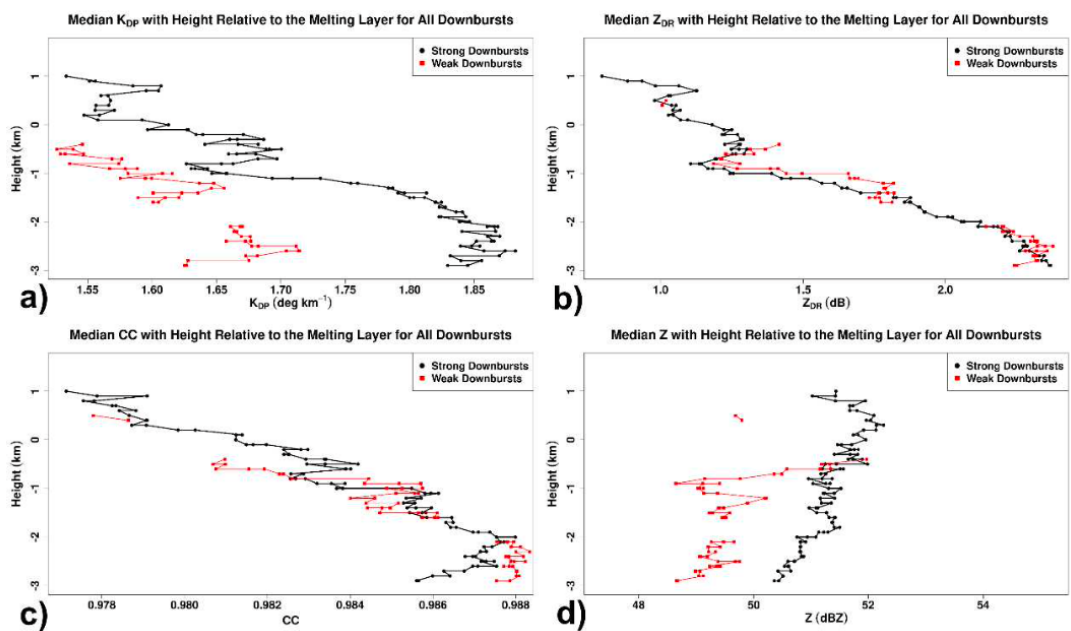
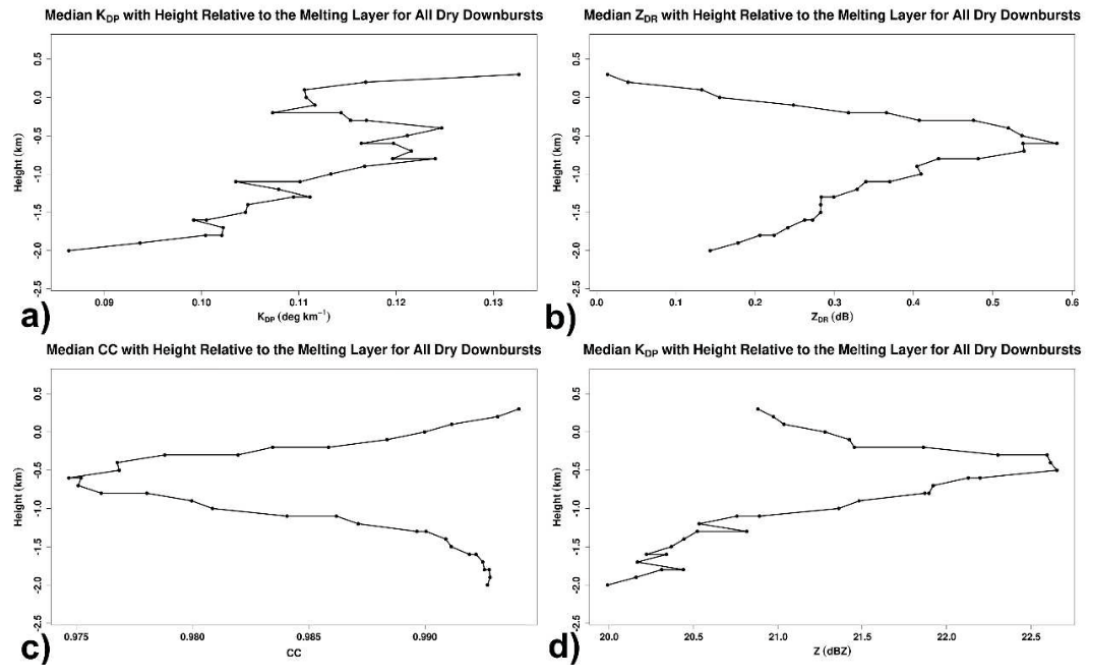


Figure 2
Vertical profiles of a) K_{DP} , b) Z_{DR} , c) correlation coefficient, and d) reflectivity for eight dry downbursts in Colorado relative to the environmental melting layer (0 km on y-axis is melting layer height).



Forecaster feedback also led to the analysis of eight dry downbursts (max $Z < 40$ dBZ) in Colorado that are much more representative of downbursts typically observed in the western United States (e.g., Wakimoto 1985, Roberts and Wilson 1989). As expected, dry downbursts typically have no or very weak K_{DP} cores due to much lower liquid water contents within the storm compared to wet downbursts. Using K_{DP} to predict dry downbursts is likely very difficult or not possible. Vertical profiles and gradients of other radar variables, especially Z_{DR} , may prove useful as there is evidence of evaporation (e.g., decreasing Z_{DR} , K_{DP} and Z with decreasing height) below the melting layer in the dry downburst events we studied (Fig. 2). However, the magnitude of the vertical change in any radar variable is small, which would likely make using the features challenging in real-time operations. Nevertheless, more research is warranted in this area.

5. DUAL-POLARIZATION FEATURES WITH QLCS MESOVORTICES

Recent work on the Three Ingredients Method framework provides forecasters with a strong foundation for understanding and anticipating mesovortex development via a combination of environmental conditions and single-polarization radar features (e.g., Schaumann and Przybylinski 2012; Gibbs et al. 2021). Predicting QLCS mesovortices and tornadoes is still a significant forecast challenge, so we are looking into additional dual-polarization features that could increase confidence in mesovortex development and whether or not that mesovortex will produce a tornado. Our analysis so far has shown that Z_{DR} columns and 50+ dBZ -20°C Z cores do not provide much information about mesovortex development or intensity, but low-level (i.e., 0.5° elevation angle) areas of enhanced spectrum width, low- and midlevel K_{DP} cores, and low- level K_{DP} drops do. Here, we focus on the K_{DP} features.

5.1 LOW- AND MIDLEVEL K_{DP} CORES

In our analysis of 120 mesovortices so far, the biggest differences, and therefore greatest statistical significance, in the distributions of feature magnitude between tornadic and nontornadic mesovortices occurs with low- and midlevel K_{DP} cores (Fig. 3). To quantify these features, we determine the maximum value of K_{DP} within the K_{DP} core ($K_{DP} \geq 1.0^{\circ}\text{km}^{-1}$) for all volume scans between the time of feature development and mesovortex dissipation. Midlevel K_{DP} cores are measured at the elevation angle closest to, but not above the environmental melting layer—determined using a combination of observed soundings and radar observations—and at a constant altitude planned position indicator (CAPPI) at the height of the environmental melting layer. Low-level K_{DP} cores are simply measured at the 0.5° elevation angle. About 74% of mesovortices are associated with a midlevel K_{DP} core and 78% are associated with a low-level K_{DP} core. In addition, significant differences existed for low- and midlevel K_{DP} core magnitude between tornadic and nontornadic mesovortices. Therefore, it is possible that forecasters could use K_{DP} cores to anticipate not only mesovortex development but also whether or not that mesovortex will be tornadic or not. This is especially true of midlevel K_{DP} cores that typically develop at least 10 minutes prior to a mesovortex, whereas low-level K_{DP} cores typically develop around the same time as the mesovortex—but typically before a tornado develops. One caveat to this idea is that there is some overlap between the distributions of K_{DP} core magnitude for tornadic and nontornadic mesovortices (Fig. 3a, b). K_{DP} cores of nontornadic mesovortices can sometimes be just as strong if not stronger than those associated with tornadic mesovortices. However, in general, if a midlevel K_{DP} core has max values over about $4.9^{\circ}\text{km}^{-1}$ (the upper quartile for nontornadic mesovortices), a forecaster could be more confident that a mesovortex will produce a tornado, especially since this value is also just below the lower quartile for tornadic mesovortices (Fig. 3b). In addition, low- and midlevel K_{DP} core magnitude tends to be stronger for tornadoes with a higher rating on the Enhanced Fujita (EF) scale (Fig. 3c, d).

6. CONCLUSIONS

Through various studies examining dual-polarization radar features, we suggest that incorporating these features into existing conceptual models applied by forecasters while issuing severe weather warnings and advisories would help increase forecaster confidence in those warnings and advisories. Z_{DR} columns develop prior to -20°C Z cores and tend to be stronger and taller for severe thunderstorms. K_{DP} cores are a reliable and consistent downburst precursor that may help forecasters anticipate downburst intensity especially when combined with environmental information. Lastly, stronger low- and midlevel K_{DP} cores tend to be associated with tornadic QLCS mesovortices, while low-level K_{DP} drops frequently precede mesovortex development and give some indication as to where a mesovortex is going to develop. Further research and larger sample sizes are needed to verify this work, but early results suggest dual-polarization features can help forecasters with various forecast challenges posed by hazardous weather.

Figure 3. Violin plots for maximum K_{DP} within the a) low-level (i.e., 0.5° elevation angle) and b) midlevel (i.e., elevation angle closest to but below the environmental melting layer) K_{DP} core for tornadic and nontornadic mesovortices and for c) low-level and d) midlevel K_{DP} cores for tornadoes of various EF scale ratings (NA are nontornadic mesovortices). P values indicating statistical significance (< 0.05 considered significant) are included in a) and b) and number of mesovortices (n) included for all panels.

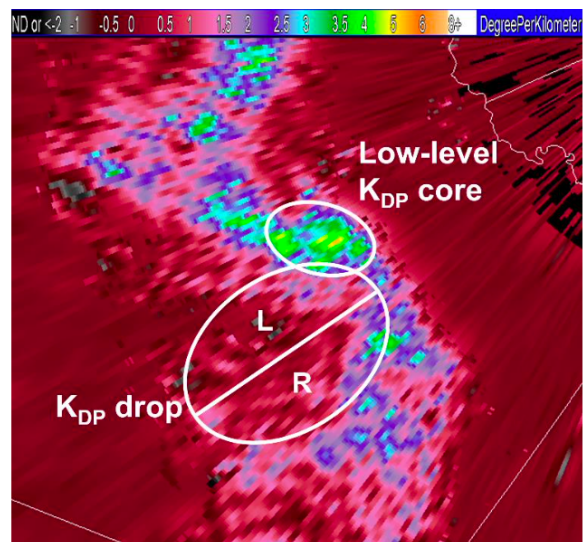
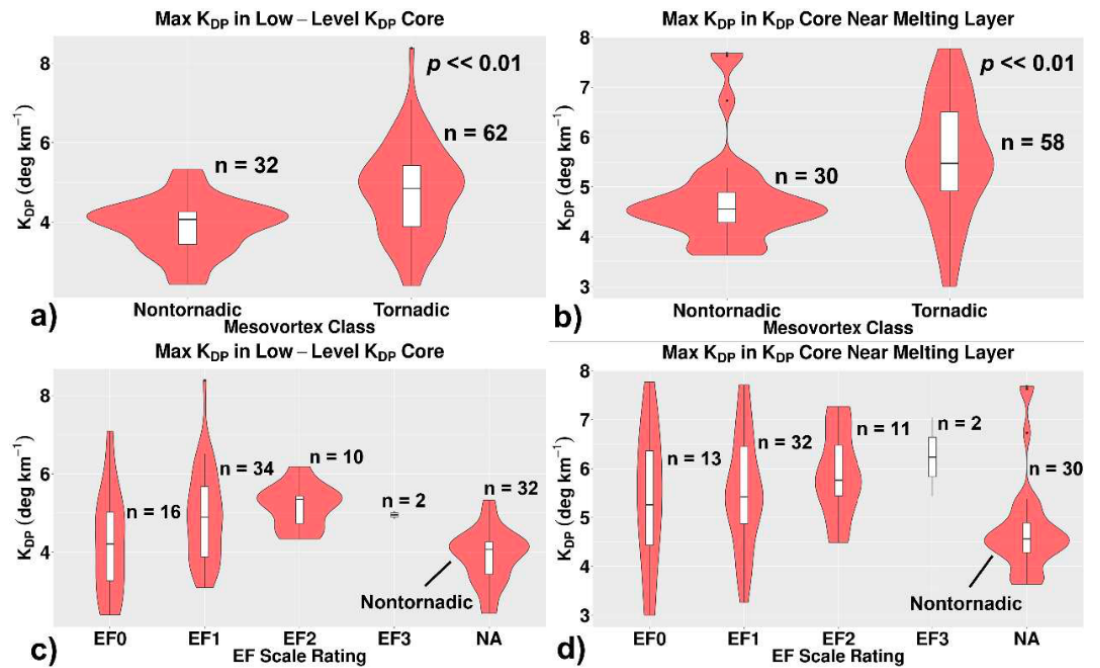


Figure 4. Snapshot of K_{DP} during a QLCS event on 20 February 2017 in Texas. Approximate locations of a K_{DP} drop and low-level K_{DP} core are highlighted by ovals, and left and right side of K_{DP} drop are indicated.

ACKNOWLEDGMENTS

CK thanks God for providing the opportunities and talented research teams to accomplish this work. We also thank Andy Dean for help with gathering environmental data, Jason Schaumann for help with the Three Ingredients Method framework and guidance about useful dual-polarization radar features, Eddie Forren for help with processing KOUN data, Jeff Brogden and Robert Toomey for help with radar viewing software, Danny Wasielewski, Michael Shattuck, Chad Smith, Felicia Woolard, Allen Zahrai, and Rafael Mendoza for help with KOUN data collection, everyone at NSSL IT, all administrative staff within CIWRO and NSSL, and many National Weather Service forecasters who provided input and guidance throughout the research process.

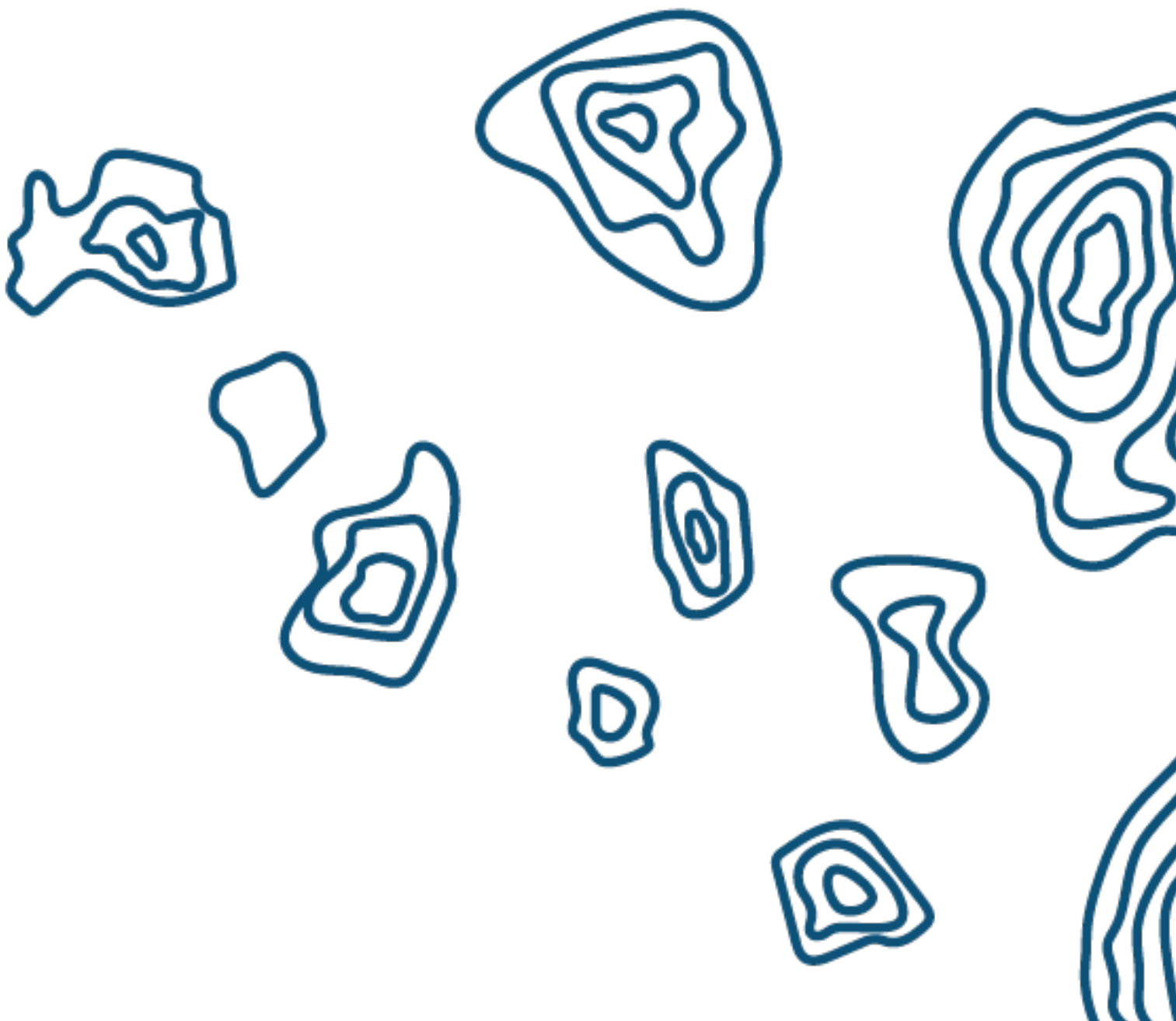
REFERENCES

- Andra, D. L., Quoetone, E. M., and Bunting, W. F.: Warning decision-making: The relative roles of conceptual models, technology, strategy, and forecaster expertise on 3 May 1999. *Weather and Forecasting*, 17, 559–566, [https://doi.org/10.1175/1520-0434\(2002\)017<0559:WDMTRR>2.0.CO;2](https://doi.org/10.1175/1520-0434(2002)017<0559:WDMTRR>2.0.CO;2), 2002.
- Gibbs, J. G.: Evaluating precursor signals for QLCS tornado and higher impact straight-line wind events, *Journal of Operational Meteorology*, 9, 62–75, <https://doi.org/10.15191/nwajom.2021.0905>, 2021.
- Illingworth, A. J., Goddard, J. W. F., and Cherry, S. M.: Polarization radar studies of precipitation development in convective storms, *Quarterly Journal of the Royal Meteorological Society*, 113, 469–489, <https://doi.org/10.1002/qj.49711347604>, 1987.
- Heinselman, P. H., Priegnitz, D. L., Manross, K. L., Smith, T. M., and Adams, R. W.: Rapid sampling of severe storms by the National Weather Radar Testbed Phased Array Radar, *Weather and Forecasting*, 23, 808–824, <https://doi.org/10.1175/2008WAF20070711>, 2008.
- Houze, R. A., Rutledge, S. A., Biggerstaff, M. I., and Smull, B. F.: Interpretation of Doppler Weather Radar Displays of Midlatitude Mesoscale Convective Systems, *Bulletin of the American Meteorological Society*, 70, 608–619, [https://doi.org/10.1175/1520-0477\(1989\)070<0608:IODWRD>2.0.CO;2](https://doi.org/10.1175/1520-0477(1989)070<0608:IODWRD>2.0.CO;2), 1989.
- Kumjian, M. R.: Principles and applications of dual-polarization weather radar. part II: Warm and cold season applications, *Journal of Operational Meteorology*, 1, 243–264, <http://dx.doi.org/10.15191/nwajom.2013.0120>, 2013.
- Kumjian, M. R. and Ryzhkov, A. V.: Polarimetric signatures in supercell thunderstorms, *Journal of Applied Meteorology and Climatology*, 47, 1940–1961, <https://doi.org/10.1175/2007JAMC1874.1>, 2008a.
- Kumjian, M. R. and Ryzhkov, A. V.: Rapid-scan observations of a bow echo storm with a dual-polarization WSR-88D, 24th Conference on Severe Local Storms, Savannah, GA, 27–31 October 2008, https://ams.confex.com/ams/24SLS/techprogram/paper_141915.htm, 2008b.
- Kumjian, M. R., Khain, A. P., Benmoshc, N., Ilotoviz, E., Ryzhkov, A. V., and Phillips, V. T. J.: The anatomy and physics of ZDR columns: Investigating a polarimetric radar signature with a spectral bin microphysical model, *Journal of Applied Meteorology and Climatology*, 53, 1820–1843, <https://doi.org/10.1175/JAMC-D-13-0354.1>, 2014.
- Kuster, C. M., Snyder, J. C., Schuur, T. J., Lindley, T. T., Heinselman, P. L., Furtado, J. C., Brogden, J. W., and Toomey, R.: Rapid-update radar observations of ZDR column depth and its use in the warning decision process, *Weather and Forecasting*, 34, 1173–1188, <https://doi.org/10.1175/WAF-D-19-0024.1>, 2019.
- Kuster, C. M., Schuur, T. J., Lindley, T. T., and Snyder, J. C.: Using ZDR columns in forecaster conceptual models and decision-making, *Weather and Forecasting*, 35, 2507–2522, <https://doi.org/10.1175/WAF-D-20-0083.1>, 2020.
- Kuster, C. M., Bowers, B. R., Carlin, J. T., Schuur, T. J., Brogden, J. W., Toomey, R., and Dean, A.: Using KDP cores as a downburst precursor signature, *Weather and Forecasting*, 36, 1183–1198, <https://doi.org/10.1175/WAF-D-21-0005.1>, 2021.
- Przybylinski, R. W.: The Bow Echo: Observations, Numerical Simulations, and Severe Weather Detection Methods, *Weather and Forecasting*, 10, 203–218, [https://doi.org/10.1175/1520-0434\(1995\)010<0203:TBEONS>2.0.CO;2](https://doi.org/10.1175/1520-0434(1995)010<0203:TBEONS>2.0.CO;2), 1995.
- Roberts, R. D. and Wilson, J. W.: A proposed microburst nowcasting procedure using single-Doppler radar, *Journal of Applied Meteorology and Climatology*, 28, 285–303, [https://doi.org/10.1175/1520-0450\(1989\)028<0285:APMNPV>2.0.CO;2](https://doi.org/10.1175/1520-0450(1989)028<0285:APMNPV>2.0.CO;2), 1989.
- Schaumann, J. S. and Przybylinski, R. W.: Operational application of 0–3 km bulk shear vectors in assessing QLCS mesovortex and tornado potential, 26th Conference on Severe Local Storms, Nashville, TN, 4–8 November 2012, <https://ams.confex.com/ams/26SLS/webprogram/Paper212008.html>, 2012.
- Van Den Broeke, M. S.: Polarimetric radar metrics related to tornado life cycles and intensity in supercell storms, *Monthly Weather Review*, 145, 3671–3686, <https://doi.org/10.1175/MWR-D-16-0453.1>, 2017.
- Wakimoto, R. M.: Forecasting dry microburst activity over the high plains, *Monthly Weather Review*, 113, 1131–1143, [https://doi.org/10.1175/1520-0493\(1985\)113<1131:FDMA-OT>2.0.CO;2](https://doi.org/10.1175/1520-0493(1985)113<1131:FDMA-OT>2.0.CO;2), 1985.



POLARIMETRY

Refraction of radar beams in precipitation





REFRACTION OF RADAR BEAMS IN PRECIPITATION

Valery Melnikov^{1,2}

August 3, 2022

¹University of Oklahoma, Cooperative Institute for Severe and High Impact Weather Research and Operations, Norman, OK, USA

²NOAA/OAR National Severe Storms Laboratory, Norman OK, USA

ABSTRACT

Refraction (bending) of radar beams in the atmosphere free from precipitation is well known. A usual manifestation of this phenomenon in radar meteorology is anomalous propagation. Refraction of radar beams in precipitation is considered in this communication by analyzing radar images from X and S band radars. The refractivity of precipitation is derived and shown that it is much smaller than refractivity of humid air. Qualitative explanations of observed radar patterns are given, but quantitative descriptions do not fit the observations well.

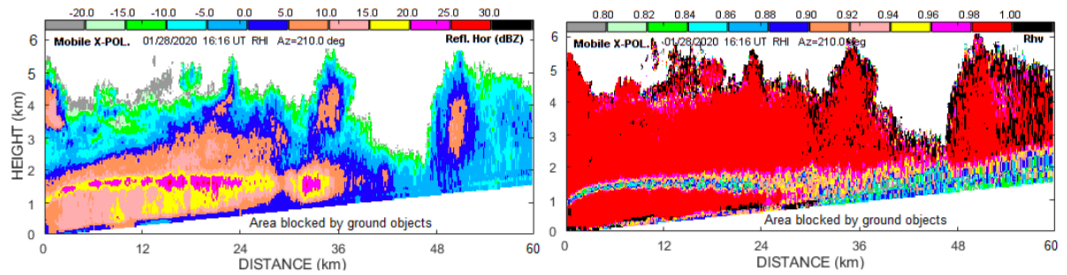
1. INTRODUCTION

Theory of refraction of electromagnetic waves in the atmosphere free from clouds and precipitation is well developed (e.g., Bean and Dutton 1968). The intensity of radio waves in the free atmosphere can be obtained from the parabolic differential equation (e.g., Levy 2000). For narrow radar beams typically used in radar remote sensing, the ray tracing approach is utilized (e.g., Bean and Dutton 1968, Doviak and Zrnic 2006, section 2). This approach allows obtaining a path of radar beam in the atmosphere at a given refraction index n along the path. In free atmosphere, n is a function of atmospheric pressure, temperature, and humidity. These parameters vary with height that leads to variations in n and cause refraction (bending) of radar beams. Various height profiles of n cause phenomena called sub-refraction, normal refraction, super-refraction (also known in radar meteorology as anomalous propagation), and ducting of radar beams (Doviak and Zrnic 2006, section 2). Refraction of radar beams in the free atmosphere manifests itself as radar echoes from the ground in areas where no echoes are observed under typical atmospheric conditions. Anomalous propagation of radar beams is caused by temperature and humidity inversions. For our knowledge, refraction of radar beams in precipitation has not been considered in the literature. In the next section, some characteristics of radar images which could be caused by refraction are discussed. In section 3, the contributions to refraction from humid air and hydrometeors are considered.

2. POSSIBLE MANIFESTATIONS OF REFRACTION IN PRECIPITATION
2.1 VISUAL BENDING OF THE MELTING LAYER

Figure 1 presents vertical cross sections (RHI) of reflectivity and correlation coefficient collected with the NSSL's mobile X band radar 28 January 2020. The radar was sitting low, therefore, the echoes from low elevations were blocked. The melting layer (ML) is seen as enhanced reflectivities (the left panel) and decreased correlation coefficients (the right panel) at the heights of 1-1.7 km. One can see bending of the ML at high antenna elevations. Such bending is observed in stratiform precipitation and is not caused by a drop of temperature in precipitation right above the radar.

Figure 1
 RHIs of (left) reflectivity and (right) correlation coefficient collected 28 January 2020 at 1616 UTC at an azimuth of 210o.



Visual bending of the ML can be qualitatively explained with the Snell's refraction law. It is customary to assume that the refraction index n decreases with height because the temperature, humidity, and pressure typically drop with height. Changes in the radar beam path in two layers having indexes n_1 and n_2 ($n_1 > n_2$) are shown in Figure 2a, which illustrates the Snell's law: $\sin\theta_1/\sin\theta_2 = n_2/n_1$. Because $n_1 > n_2$, then $\theta_1 < \theta_2$. We can apply this law to a stratiform rain schematically shown in Figure 2b. The ML is shown in the figure with the horizontal red line. The true radar beams are shown with the black curves. The launch radar angles are presented with the white straight lines. All measured radar data are placed on the launch paths. At vertical incidence, the true beam path coincides with the launch path because $\theta_1 = \theta_2 = 0$, i.e., this beam does not experience refraction. The very right actual radar beam (Figure 2b) enters the melting layer at the very right red dot, but this dot is placed on the very right launch path as the very right magenta dot because the radial distances to these dots from radar should be equal. Similar considerations hold for other true beam's paths. So, the apparent melting layer on a radar display is seen as the bent brown line. Such an ML's bending is seen in Figure 1.

Figure 2 (a)
 Illustration of the Snell's refraction law for two layers with $n_1 > n_2$

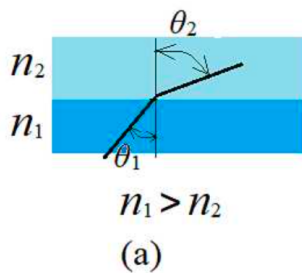
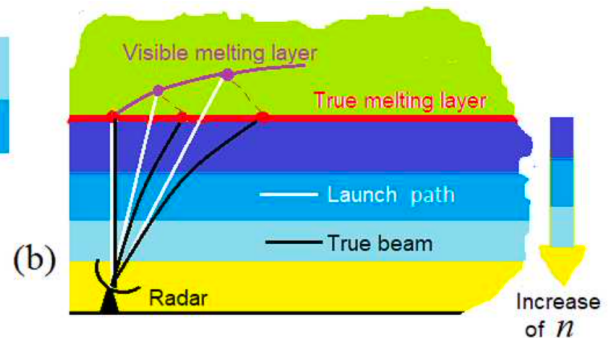


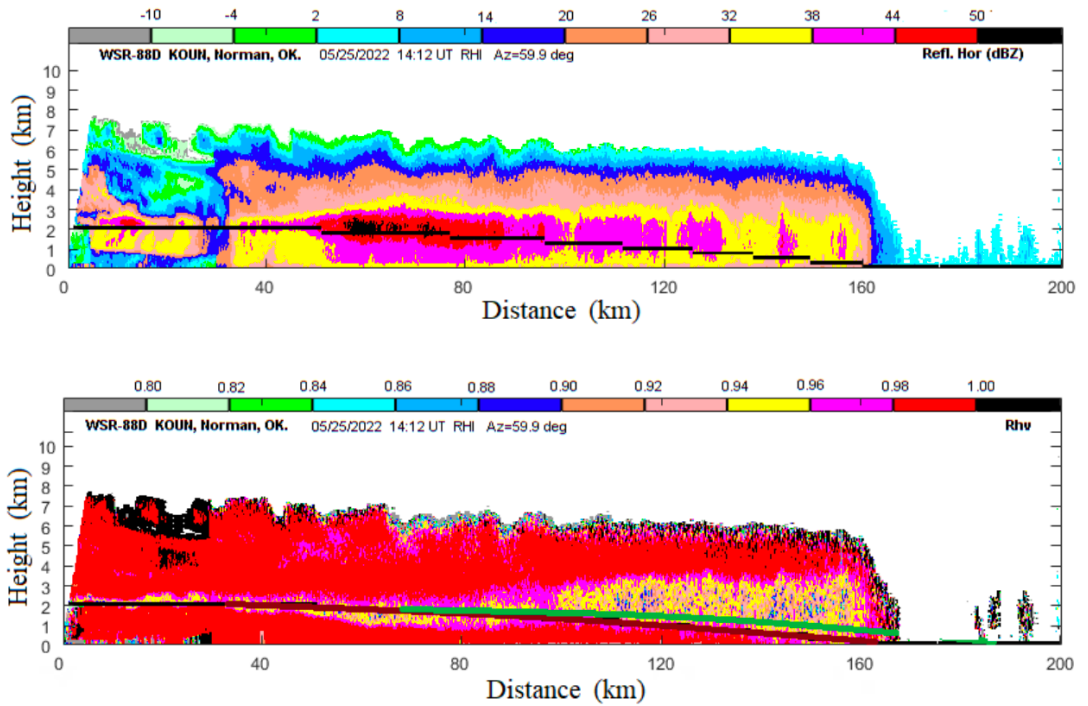
Figure 2 (b)
 To the explanation of bending of the visible ML (see the text).



2.2 AN EXAMPLE FROM S BAND RADAR

Figure 3 presents an RHI collected with S band WSR-88D KOUN 25 May 2022. The radar is located in Norman, OK, USA. These are widespread precipitation with a well visible ML. The visible ML widens with range because the radar beam widens. The mean ML's height is seen at a height of about 2 km at the large distances. The black line at short ranges from the radar lay at the ML's height obtained from the image of correlation coefficient. The black line shows the height of melting layer if there is no refraction of radar beams. The melting layer located at a height of 2.2 km as in the figure would touch the ground at 160 km in a case of no refraction. One can see that the center of visible ML is located above the black line at ranges beyond 100 km that points to strong refraction of the radar beams. Qualitatively, the higher locations of the visible ML can be explained with the Snell's law, as it was done for Figure 1. An attempt to obtain the location of melting layer by considering refraction of radar beams in precipitation is described in the next section. The result is shown in the figure with the green line, which lays below the mean visible ML's heights.

Figure 3
RHI of (top) reflectivity
and (bottom) correlation
coefficient
collected with KOUN
25 May 2022 at 1412
UTC at an azimuth of
59.9°.



3. SOURCES OF REFRACTION

The path of a radar beam in precipitation depends on the change in the refractive index, which depends on the temperature, humidity, and pressure in the atmosphere as well as on the presence of rain drops. The refractivity N of humid air can be obtained as (e.g., Doviak and Zrnica, 2006, chapter 2), green line, which lays below the mean visible ML's heights.

$$N = 77.6 P/T + 3.73 \times 10^5 e/T^2, \quad (1)$$

where T is the temperature in K, P and e are pressure of humid air and water vapor in hPa (= mb).

Refractivity of hydrometeors can be obtained from the decrease of group velocity of electromagnetic (EM) waves in rain. The decrease manifest itself in the differential phase measured between the waves at orthogonal polarizations. The group velocity of the waves is c/n , where c is speed of the waves in vacuum (e.g., Born and Wolf 1980) The reduced phase speed of EM waves in a medium leads to a decrease in its wavelength λ_m compared to that in vacuum $\lambda = 2\pi/k$, where k is the corresponding wavenumber. The decrease in the wavelength is equivalent to an increase in the wave number k_m in the medium. The wavenumber in a medium containing scattering particles can be written as (e.g., Oguchi 1981, Bohren and Huffman 1983, section 2.8; Bringi and Chandrasekar 2001, section 1.10.1),

$$k_m = k + \lambda \rho f \quad , \quad (2)$$

where ρ is the number concentration of the particles and f is their mean forward scattering amplitude. The plane coherent EM wave E_m traveling in a medium in the z direction can be described as, $E_m = \exp(jk_m z - j\omega t)$ with ω and t being the frequency of the wave and time and j is imaginary one. The amplitude f in (2) is complex; therefore, the phase change is described by the real part of k_m , which is

$$k_{mr} = k + \lambda \rho \text{Re}(f) \quad . \quad (3)$$

The imaginary part of f describes attenuation of the wave. The K_{mr} can be related to the wavelength in the medium as, $\lambda_m = 2\pi/k_{mr}$, which can be linked to the speed of the wave $v_m = c\lambda_m/\lambda = c/n$. From the latter, the refraction index for the scattering medium follows

$$n = \lambda/\lambda_m = 1 + (\lambda^2 \rho / 2\pi) \text{Re}(f). \quad (4)$$

If the medium contains particles having the size distribution $M(D)$, where D is a characteristic particles' size (e.g., the equivolume diameter of raindrops), then the refractivity of rain N_r is

$$N_r = 10^6 (\lambda^2 / 2\pi) \int M(D) \text{Re}[f(D)] dD. \quad (5)$$

The refractivity (5) corresponds to the coherent wave in the medium; therefore, it should be applied in situations where the amplitude of noncoherent part of the wave (emerging from multiple scattering in all directions but the forward one) is weaker than the amplitude of the coherent wave. The latter situation frequently occurs at S and C frequency bands and at short distances in precipitation at higher frequencies. Figure 4 shows a dependence of the rain refractivity N_r on the rain rate. N_r reaches 1 at a rain rate of 120 mm/h. Since the refraction index in rain is the product of refraction indexes of humid air and raindrops, then the refractivity in rain is the sum of N and N_r . Therefore, refraction in precipitation is determined by humid air because $N \gg N_r$ (the typical N values are 200-300 at heights close to the ground).

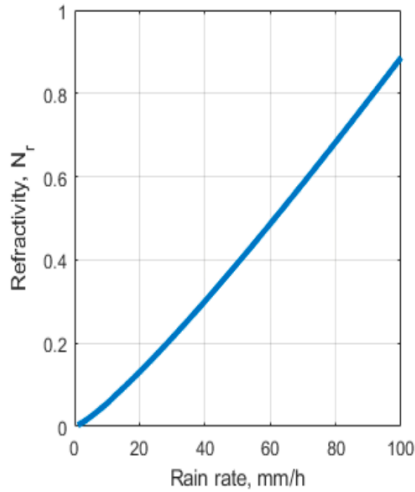


Figure 4
Refractivity N_r of rain.

One can estimate the refractivity for the case in Figure 3. Relative humidity in precipitation is higher than 96%. Therefore, propagation of radar waves in the saturated humid air can be considered. Pressure of water vapor e can be obtained from relative humidity (RH in %) and saturated water pressure (P_w) as,

$$N = 77.6 P/T + 3.73 \times 10^5 e/T^2, \quad (1)$$

where T_c is the temperature in $^{\circ}\text{C}$ (Buck 1981). In rain, $\text{RH} > 96\%$ and, therefore, $e = P_w$. To obtain the paths of radar beams in areas below the melting layers, one needs the values of pressure and temperature in the areas. These parameters can be obtained from soundings. For the case in Figure 3, the sounding data at 12 UTC for the KOUN location are: $P = 966$ hPa and $T_c = 12.4^{\circ}\text{C}$ on the ground; at the height of melting layer ($H = 2.2$ km), $P = 778$ hPa and $T_c = 0^{\circ}\text{C}$. The refractivity is obtained from eqs. (1) and (7): $N = 269.2$ on the ground and $N = 224.2$ in the melting layer. Assuming a linear decrease of N in the first two km above the ground (e.g., Bean and Dutton, 1968), the refractivity gradient is $(269.2 - 224.2)/2.2 = 20.5 \text{ km}^{-1}$ in N units. Using this gradient for the whole distance in Figure 3, the corresponding apparent height of the melting layer has been obtained and is shown with the green line. It is seen that this line is located lower than the mean visible heights of the melting layer. That is, refraction in the precipitation is stronger than that obtained from eqs. (1-7) and the given temperatures and pressures. The presented calculation results do not quite correspond to the observed locations of the ML. Similar results have been obtained for other stratiform precipitation cases.

4. CONCLUSIONS

Refraction of radar beams in precipitation can be observed from apparent bending of the melting layers on radar vertical cross sections. Such bending can be caused by changing temperatures in atmospheric fronts as well as refraction of radar beams. The analyzed examples show that in widespread precipitation, bending of the melting layer is caused by refraction of radar beams. Refraction can be induced by humid air in precipitation and hydrometeors. The refractivity of hydrometeors N_r is derived in section 3, and it appears to be much smaller than that of humid air. Therefore, refraction of radar beams in precipitation is mostly determined by saturated humid air. Refraction of radar beams in precipitation can be qualitatively explained with the Snell's law, but it is hard to quantitatively describe apparent locations of the melting layer because a fine structure of temperature in precipitation could be needed. An incorrect account for refraction of radar beams in precipitation can lead to incorrect measurements of the height of melting layers and ZDR and KDP columns observed through extensive stratiform precipitation.

REFERENCES

- Bean, B. R., and E. J. Dutton: *Radio Meteorology*. Dover Publications, 435 pp, 1968
- Bohren, C.F., and D.R. Huffman: *Absorption and Scattering of Light by Small Particles*, John Wiley and Son, San Diego, CA. 530 pp, 1983.
- Born, M., and E. Wolf: *Principles of Optics*. Pergamon Press, N.Y., 808 pp, 1980.
- 65
- Bringi, V. N., and V. Chandrasekar: *Polarimetric Doppler Weather Radar. Principles and Applications*. Cambridge University Press. 636 pp, 2001
- Buck, A. L. 1981: *New equations for computing vapor pressure and enhancement factor*, *J. Appl. Meteorol.*, 20: 1527–1532.
- Doviak, R. J. and D. S. Zrnic: *Doppler radar and weather observations*, 2nd ed., Academic Press, 562 pp, 2006.
- Levy, M.: *Parabolic equation methods for electromagnetic wave propagation*. Institution of Electrical Engineers, UK, 336 pp, 2000.
- Oguchi, T.: *Summary of studies on scattering of centimeter and millimeter waves due to rain and hail*. *Ann. Telecommunic.* 36, 383 – 399, 1981.

QUANTITATIVE PRECIPITATION ESTIMATION

Supporting Weather Radar Observations with the Vaisala FD70





SUPPORTING WEATHER RADAR OBSERVATIONS WITH THE VAISALA FD70

Dirk Klugmann¹, Lasse Kauppinen¹, Robinson Wallace², Jordan Santillo^{1,3}

March 29, 2022

¹Vaisala Oyj, Vantaa, Finland

²Vaisala Inc, Boulder, CO, USA

³University of Helsinki, Helsinki, Finland

ABSTRACT

We introduce the Vaisala Forward Scatter Sensor FD70 as a tool for improving the quality of Quantitative Precipitation Estimation (QPE) and hydrometeor classification with weather radar. After an introduction into the topic of QPE and hydrometeor classification, we describe the Vaisala FD70 and detail the parameters observed by it. Then we touch on observables from polarimetric weather radar, before we move on to applications of the Vaisala FD70 in this context. Outlook for the study and our conclusions round off this contribution.

1. INTRODUCTION

Since the introduction of weather radar, attempts have been made to utilize weather radar derived Quantitative Precipitation Estimation (QPE). The first approach to QPE based on weather radar observations is described by Marshall and Palmer (1948), where they define a relationship between radar reflectivity factor Z and rainfall rate R in the form:

$$Z = a \cdot R^b$$

An important issue with utilizing Z-R relationships is the notorious variability of the associated empirically determined constants applied to R . Four sets of constants a and b for the Z-R relationship are listed already in Marshall and Palmer (1948), and many more have been added since. In spite of the challenges associated with radar derived QPE, radars still provide invaluable benefits to QPE. The most significant benefits include the wide areal coverage and the remote sensing capabilities, which cannot be provided by rain gauges. Thus, data collected by radars cannot be discounted. This is especially true given the historical and ongoing development of weather radars. Weather radars were initially improved by introducing Doppler capability (e.g. Heiss et al. (1990)). However, this added capability alone did not substantially improve the measurement to QPE. Instead, better QPE performance came from the combination of observations from weather radar and ground based rain gauges (e.g. Wilson (1970); Brandes (1975); Krajewski (1987); Matsoukas et al. (1999)). Even further

improvements in QPE capabilities came with the subsequent development of polarimetric weather radar (e.g. Matrosov et al. (2002); Brandes et al. (2003); Ryzhkov et al. (2005)). Despite these advancements, rainfall rate relationships using state-of-the-art weather radars are still imperfect. Such relationships are often empirically derived, use data averaged over long periods of time, and assume a specific shape to the drop size distribution (DSD). Each of these assumptions can affect QPE accuracy. This poses the question whether QPE can be accurately determined over short time periods without assuming a specific shape to the DSD. To answer this question, a quality instrument that allows comparing radar derived QPE and ground based precipitation measurements is required. This contribution will show how the Vaisala Forward Scatter Sensor FD70 can be used to calibrate radar parameters and develop an accurate rainfall rate relationship utilising observables from polarimetric weather radar.

Figure 1
Geometrical layout
of the Vaisala FD70
versions.

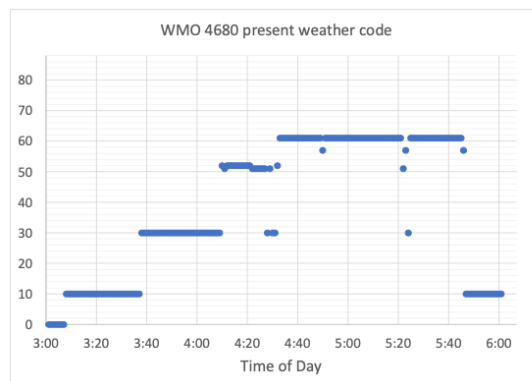


(a) Two-headed (single receiver)

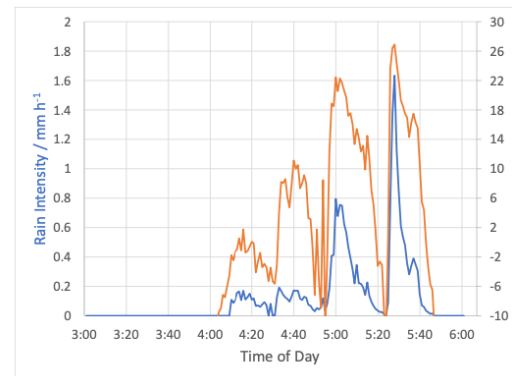
(b) Three-headed (two receivers)

2. VAISALA FORWARD SCATTER SENSOR FD70

Figure 2
Three hours of
observations from
Vaisala FD70 located
at Vaisala Helsinki Test
Site on 12/09/2021.



(a) SYNOP messages



(b) Rain intensity and radar reflectivity factor

The Vaisala Forward Scatter Sensor FD70, as introduced by Heyn (2019), combines forward Rain Intensity / mm h⁻¹ Radar Reflectivity Factor / dBZ scatter and optical disdrometer technologies. It employs the novel use of a single thin light sheet instead of the conventional light cone, and utilizes look-down forward scatter geometry. This results in high detection sensitivity, which enables scatter-property analysis of each single particle and allows detection of even the smallest drizzle droplets. In the standard configuration displayed in Fig. 1(a), the receiver measures forward scattered light at an angle of 42°. The extended version, shown in Fig. 1(b),

features a second sensor head measuring light scattered at an angle of 90° . This latter version assures enhanced visibility measurement in dusty conditions and provides improved identification of freezing precipitation. Both versions of the Vaisala FD70 utilise a look-down geometry to minimize measurement disturbances. They support precipitation type identification, intensity, and accumulation with superior liquid / frozen differentiation and an exceptional precipitation detection sensitivity. All droplets with a diameter exceeding 0.1 mm are detected, while the WMO requirement prescribes a detection limit for droplets of 0.2 mm diameter. Both Vaisala FD70 configuration versions provide information on drop size distribution (DSD) and radar reflectivity. The observation parameters provided by the Vaisala FD70 with a Measurement cycle of 5s are listed in Table 1. Examples for observations generated on 12/09/2021 by a Vaisala FD70 at the Vaisala Helsinki Test Site in routine operation are shown in Fig.2(a) and Fig. 2(b). The former displays three hours of surface synoptic observations (SYNOP), demonstrating the capability of the system for observing the present weather, with a time resolution of 1 minute selected for the displayed graph. The latter displays three hours of rain rate and radar reflectivity factor observations, again with 1 minute time resolution. From the prior, the rain accumulation over any longer time period can be calculated.

Parameter	Reporting Range	Resolution
Visibility (MOR)	1 m–100 km	1 m
Present weather (SYNOP)	WMO table 4680	
Present weather (METAR)	WMO table 4678	
Precipitation intensity	0.01–999.99 mm/h	0.01 mm/h
Precipitation accum.	0.01–999.99 mm	0.01 mm
DSD (diameter)	0.1–35 mm	41 classes
Fall speed distribution	0–10(+) m/s	26 classes
Radar reflectivity fact.	-9.9–99.9 dBZ	
Kinetic energy	0–999.999 J/m ² × h	

Table 1

Weather parameters observed by Vaisala FD70.

3. POLARIMETRIC WEATHER RADAR OBSERVABLES

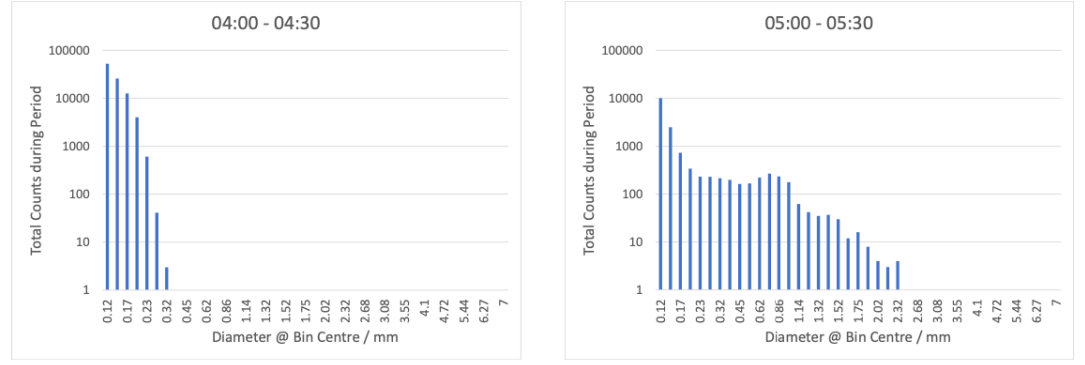
3.1 RADAR REFLECTIVITY FACTOR

The generic value for the radar reflectivity factor at horizontal polarisation for raindrops z_h can be calculated from the sixth moment of the DSD:

$$z_h = \int_0^{\infty} N(D) D^6 dD \quad (2)$$

where z_h is in mm⁶ m⁻³. Here D is the diameter and $N(D)$ is the number concentration of raindrops with diameter D . To convert z_h to Z_h in units of dBZ, as used in Eq. (1):

Figure 3
Drop size distributions (total counts) for two 30-minute periods observed on 12/09/2021 by Vaisala FD70 at Vaisala Helsinki Test Site.



(a) 12/09/2021, 04⁰⁰ - 04³⁰

(b) 12/09/2021, 05⁰⁰ - 05³⁰

$$Z_h = 10 \cdot \log_{10} (z_h)$$

3.2 DIFFERENTIAL RADAR REFLECTIVITY

An accurate calculation of the differential radar reflectivity ZDR which respects the backscatter cross section in each polarization requires the knowledge of the drop axis ratio r. For drop diameter D < 1 mm or D > 4 mm a relation from Beard and Chuang (1987) can be used to calculate r, while an equation from Chandrasekar et al. (1988) can be used for 1 mm < D < 4 mm. Derived from this, the value of z_{dr} (in linear units) for a DSD eventually can be calculated via the following:

$$z_{dr} = \frac{\int_0^\infty N(D) D^6 \left| \frac{\epsilon_r - 1}{1 + \frac{1}{2}(1 - \lambda_z)(\epsilon_r - 1)} \right|^2 dD}{\int_0^\infty N(D) D^6 \left| \frac{\epsilon_r - 1}{1 + \lambda_z(\epsilon_r - 1)} \right|^2 dD} \tag{4}$$

where ϵ_r is the permittivity of water. λ_z is the depolarizing factor (Bringi and Chandrasekar (2001)), which dependent on r. The Differential Radar Reflectivity ZDR in units of dB is obtained from:

$$Z_{DR} = 10 \cdot \log_{10} (z_{dr})$$

3.3 SPECIFIC DIFFERENTIAL PHASE

The Specific Differential Phase K_{DP} in ° km⁻¹ can be calculated using:

$$K_{DP} = \left(\frac{180}{\lambda} \right) \cdot C \cdot \left(\frac{W}{\rho_w} \right) \left[1 - \frac{\int_0^\infty r N(D) D^3 dD}{\int_0^\infty N(D) D^3 dD} \right] \tag{6}$$

where λ is the radar wavelength. Furthermore, C is a constant, for which Gorgucci et al. (2002) assume C = 3.75, valid for hydrometeors measured at microwave frequencies in the range from 3 GHz to 30 GHz. Finally, W is the total rain water content, given by:

$$W = \frac{\pi}{6} \rho_w \int_0^\infty N(D) D^3 dD \tag{7}$$

Here ρ_w is the density of water in g m⁻³. According to Bringi and Chandrasekar (2001), Eq. (6) is valid for microwave frequencies up to 13 GHz.

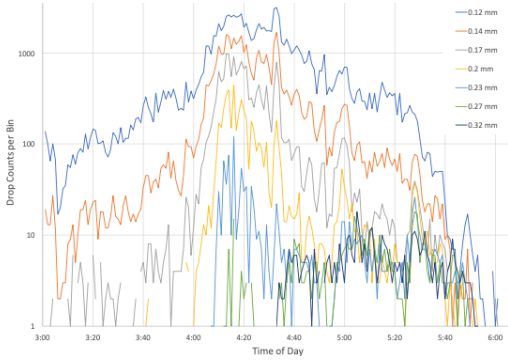


Figure 4
Three hours of 1-minute FD70 drop number observations in individual bins on 12/09/2021 at Vaisala Helsinki Test Site. Only the graphs for the bins of the seven smallest droplet diameters are displayed.

3.4 INFORMATION DERIVED FROM POLARIMETRIC OBSERVABLES

A wide range of information can be derived from the polarimetric weather radar observables introduced in the previous subsections. These include rain rate R (often also referred to as rain intensity) and hydrometeor class (typically rain, snow, wet snow, graupel, hail, and non-meteorological targets). Here we focus on the deriving rain rate. An algorithm for this purpose described in Ryzhkov et al. (2005) first identifies a rain rate using a conventional z - R relationship:

$$R(z) = 1.70 \cdot 10^{-2} \cdot z^{0.714} \quad (8)$$

where z is in linear units of $\text{mm}^6 \text{m}^{-3}$.

Following the calculation of $R(z)$ from Eq.(8), a specific dual-polarization parameter rain rate relationship is selected per an algorithm. The algorithm is as follows:

For $R(z) \leq 6 \text{mmhr}^{-1}$:

$$R(z, z_{\text{dr}}) = \frac{R(z)}{0.4 + 5.0 |z_{\text{dr}} - 1|^{1.3}} \quad (9)$$

For $6 \text{mmhr}^{-1} < R(z) \leq 50 \text{mmhr}^{-1}$:

$$R(K_{\text{DP}}, z_{\text{dr}}) = \frac{R(K_{\text{DP}})}{0.4 + 3.5 |z_{\text{dr}} - 1|^{1.7}} \quad (10)$$

with $R(K_{\text{DP}})$ taken from Eq. (11). For $R(z) > 50 \text{mmhr}^{-1}$:

$$R(K_{\text{DP}}) = 44.0 |K_{\text{DP}}|^{0.822} \quad (11)$$

Note that z_{dr} is in linear units and K_{DP} is in km^{-1} . It also should be recognized that the parameter set for Eqs. (8) to (11) has been derived from data of a single radar collected in one geographical location.

4. APPLICATIONS OF THE FD70

In this section, potential applications of the Vaisala FD70 are discussed. One example of useful observations is provided in Fig. 3, which shows logarithmic-scale histogram plots for drop size distributions (DSDs) of two 30-minute periods (raw counts) with a starting time differing by one hour. These observations were made by a Vaisala FD70 located at Vaisala's Helsinki Testfield. The histogram in sub-plot (a), recorded 12/09/2021, 0400 – 0430, shows a narrow and mono-modal DSD with observed droplet diameters not exceeding 0.53 mm. The histogram in sub-plot (b), recorded 12/09/2021, 0500 – 0530, shows a much wider and presumably bi-modal DSD with observed drop diameters reaching up to 3.31 mm. The averaging period has been chosen in alignment with the time resolution provided by numerous precipitation products generated from satellite observations or weather forecast models. As shown in Table 1, the time resolution of the Vaisala FD70 for drop size observations is much better than the 30 minutes chosen for the observations displayed in Fig. 3. This is demonstrated by Fig. 4, which displays the drop numbers in selected individual drop size bins with a time resolution of 1 minute. The reporting interval of the Vaisala FD70 can be as short as 5 s. These observations form the base for longer

integrated products, e.g. the DSD histograms displayed in Fig. 3.

DSD	$R/\text{mm h}^{-1}$	Z/dBZ	Z_{dr}/dB	$K_{\text{DP}}/^\circ \text{km}^{-1}$
04:00 – 04:30	0.0672	-3.025 (-3.521)	0.017 (-0.030)	0 (-0.001)
05:00 – 05:30	0.416	21.49 (21.59)	0.727 (0.506)	0.0114 (0.0021)
Marshall and Palmer (1948)	0.416	19.16 (19.23)	0.344 (0.239)	0.0133 (0.0018)

Table 2
Polarimetric observables for S-band weather radar calculated from DSDs presented in Fig. 5 and according to Marshall and Palmer (1948). Values for Z, ZDR and KDP calculated according to Bringi and Chandrasekar (2001), values in brackets calculated by T-Matrix method according to Mishchenko et al. (1996).

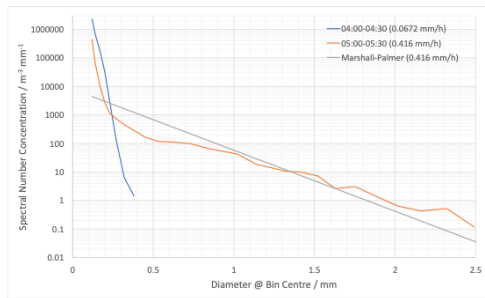


Figure 5
Graphs of spectral number concentrations derived from the FD70-observed 30-minute size distributions displayed in Fig. 4. A distribution after Marshall and Palmer (1948) has been added for reference.

4.1 CALIBRATION AND VALIDATION

Weather radar observations are frequently validated and corrected using rain gauge and disdrometer observations. This approach also can benefit from the superior performance, reliability, and accuracy of the Vaisala FD70. Specifically for rain rate retrievals based on polarimetric radar observables, information on the drop size distribution of the observed precipitation can provide improvements in QPE quality not achievable with plain rain gauges. An example for this can be derived from Fig. 5. This shows two spectral drop number concentrations derived from the observations with a Vaisala FD70 displayed in Fig. 3, and a theoretical spectral drop size concentration according to Marshall and Palmer (1948) for the same rain rate as the DSD recorded later. The rain rates given for the observations are taken from the output of the Vaisala FD70. From these three DSDs, the values for Z, ZDR and KDP for S-band radar have been calculated according to Bringi and Chandrasekar (2001) and with code based on Mishchenko et al. (1996), respectively. Both methods provide nearly identical results for Z, while the values for ZDR already differ noticeably. The values for KDP differ by nearly one order of magnitude. For both calculation methods, the difference of the results for the DSD observed 05:00 – 05:30 clearly differs from those of the DSD according to Marshall and Palmer (1948) in spite of the identical rain rate. Using the parameter set provided by Ryzhkov et al. (2005), the rain rates retrieved with the values for polarimetric observables for these two DSDs are $R_{\text{DSD,obs}} = 0.61 \text{ mm h}^{-1}$ and $R_{\text{DSD,MP}} = 0.67 \text{ mm h}^{-1}$. These results differ from each other in the order of 10%, but diverge even more significantly from the value $R_{\text{FD70,obs}} = 0.416 \text{ mm h}^{-1}$ listed in Table 1 directly observed by the Vaisala FD70. In the same way as the observed DSD differs from the theoretical one, individual DSDs also differ – even for identical rain rates. These differences are caused by many factors including location, season, and prevailing weather situation. Furthermore, rain rates derived from polarimetric radar observables with pre-set parameter sets for the retrieval algorithm can deviate substantially from directly observed values. Rain rates derived from polarimetric observables deviate from those directly reported by the Vaisala FD70, though the utilised polarimetric observables have been calculated using DSDs from the same data set. Therefore it would improve the QPE quality if a flexible, more accurate parameter set for QPE based on polarimetric observables could be implemented. The Vaisala FD70 can be a valuable tool for achieving this goal.

5. OUTLOOK

The approach presented in Section 4 will be applied to observations from the Vaisala FD70 at widely varying rain rates and with differing accumulation times. Specifically, we intend to compare observations with nearly identical rain rates, and investigate the variation of the calculated polarimetric observables. Then we will calculate the variability of rain rates derived from these using a published retrieval algorithm for polarimetric weather radar. Finally, we want to compare the results from observations recorded by multiple Vaisala FD70 with those derived from observations of weather radars Vaisala operates for research purposes, partially in collaboration with Helsinki University.

6. CONCLUSIONS

After an introduction into the topic of QPE, we described the Vaisala Forward Scatter Sensor FD70. It has been shown that this observing system can be a valuable tool for supporting Quantitative Precipitation Estimation (QPE) by weather radar. We demonstrated the deviation of drop size distributions (DSDs) from theoretical functions describing these, and the resulting variation in polarimetric weather radar observables. We also pointed out the risk of substantial difference between the rain rates calculated from polarimetric weather radar observables and rain rates directly observed by a Vaisala FD70. This indicates that the value of the Vaisala FD70 as a valuable tool for supporting calibration and validation for precipitation products, and in applications for augmenting and correcting weather radar QPE.

REFERENCES

- Beard, K. V. and Chuang, C.: A New Model for Equilibrium Shape of Raindrops, *Journal of the Atmospheric Science*, 44, 1509–1524, 1987.
- Brandes, E. A.: Optimizing Rainfall Estimates with the Aid of Radar, *J. Appl. Meteor.*, 14, 1,339– 1,345. [https://doi.org/10.1175/1520-0450\(1975\)014<1339:OREWTA>2.0.CO;2](https://doi.org/10.1175/1520-0450(1975)014<1339:OREWTA>2.0.CO;2), 1975.
- Brandes, E. A., Zhang, G., and Vivekanandan, J.: An Evaluation of a Drop Distribution-Based Polarimetric Radar Rainfall Estimator, *J. Appl. Meteor.*, 42, 652–660, [https://doi.org/10.1175/1520-0450\(2003\)042<0652:AEOADD>2.0.CO;2](https://doi.org/10.1175/1520-0450(2003)042<0652:AEOADD>2.0.CO;2), 2003.
- Bringi, V. N. and Chandrasekar, V.: *POLARIMETRIC DOPPLER WEATHER RADAR*, Cambridge University Press, 2001.
- Chandrasekar, V., Cooper, W. A., and Bringi, V. N.: Axis Ratios and Oscillations of Raindrops, *J. Atmos. Sci.*, 45, 1323–1333, 1988.
- Gorgucci, E., Chandrasekar, V., Bringi, V. N., and Scarchilli, G.: Estimation of Raindrop Size Distribution Parameters from Polarimetric Radar Measurements, *J. Atmos. Sci.*, 59, 2373–2384, 2002.
- Heiss, W. H., McGrew, D. L., and Sirmans, D.: Nexrad: Next Generation Weather Radar (WSR-88D), *J. Meteor.*, 33, 1990.
- Heyn, K.: Performance Limitations of Optical Present Weather and Visibility Sensors under Special Consideration of the Utilized Technology and the Related Measurement Uncertainties, in: *AMS Annual Meeting, Special Symposium on Meteorological Observations and Instrumentation*, American Meteorological Society, American Meteorological Society, 2019.
- Krajewski, W. F.: Cokriging radar-rainfall and rain gage data, *J. Geophys. Res.*, 92, 9,571–9,580, 1987.
- Marshall, J. S. and Palmer, W. M. K.: The distribution of raindrops with size, *J. Meteor.*, 5, 165–166, 1948.
- Matrosov, S. Y., Clark, K. A., Martner, B. E., and Tokay, A.: X-Band Polarimetric Radar

Measurements of Rainfall, J. Appl. Meteor., 41, 2002.

- Matsoukas, C., Islam, S., and Kothari, R.: Fusion of radar and rain gage measurements for an accurate estimation of rainfall, *J. Geophys. Res.*, 104, 31,437–31,450, <https://doi.org/10.1029/1999JD900487>, 1999.
- Mishchenko, M. I., Travis, L. D., and Mackowski, D. W.: T-matrix computations of light scattering by nonspherical particles : A review, *J. Quant. Spectrosc. Radiat. Transfer*, 55, 535–575, 1996.
- Ryzhkov, A. V., Schuur, T. J., Burgess, D. W., Heinselman, P. L., Giangrande, S. E., and Zrnica, D. S.: THE JOINT POLARIZATION EXPERIMENT, *Bull. Amer. Meteor. Soc.*, pp. 809–824, <https://doi.org/10.1175/BAMS-86-6-809>, 2005.
- Wilson, J. W.: Integration of Radar and Raingage Data for Improved Rainfall Measurement, *J. Appl. Meteor.*, 9, 489–497, [https://doi.org/10.1175/1520-0450\(1970\)009<0489:IORARD>2.0.CO;2](https://doi.org/10.1175/1520-0450(1970)009<0489:IORARD>2.0.CO;2), 1970.

RADAR IN NUMERICAL WEATHER PREDICTION

Operational assimilation of radar reflectivity and radial wind volumes in the COSMO model
at Arpae-SIMC





OPERATIONAL ASSIMILATION OF RADAR REFLECTIVITY AND RADIAL WIND VOLUMES IN THE COSMO MODEL AT ARPAE-SIMC

Virginia Poli², Thomas Gastaldo¹, Chiara Marsigli^{1,2}, Davide Cesari², Pier Paolo Alberoni²

August 5, 2022

¹Arpae Emilia-Romagna, HydroMeteorological Structure, Bologna, Italy

²Deutscher Wetterdienst, Offenbach, Germany

ABSTRACT

At Arpae-SIMC, the HydroMeteorological Structure of Emilia-Romagna Region in Italy, radar reflectivity and radial wind volumes are assimilated into the high-resolution limited area COSMO model by means of the Kilometer Ensemble Data Assimilation (KENDA) system based on the Local Ensemble Transform Kalman Filter (LETKF) technique. To evaluate the impact of these observation types, different assimilation configurations have been tested. Verification results, in terms of quantitative precipitation forecasts (QPF) and near-surface and upper-air variables, show an improvement of the quality of forecasts, in particular in the first hours.

1. INTRODUCTION

At Arpae-SIMC, the HydroMeteorological Structure of Emilia-Romagna Region in Italy, an ensemble-based data assimilation system at the convective-scale (KENDA-LETKF) provides the analyses to the high-resolution limited area models: a deterministic forecast, COSMO-2I, and an ensemble forecast system, COSMO-2I-EPS, running both at 2.2 km horizontal resolution. The domain of model integrations covers the entire Italian territory and part of the surrounding countries and seas. With this method, already employed for the operational assimilation of conventional observations, since March 2021 radar reflectivity volumes and, since March 2022, radial wind volumes have been assimilated. The use of these observations is in combination with the assimilation of radar-estimated instantaneous precipitation via latent heat nudging (LHN; Jones and Macpherson, 1997). Volumetric data and instantaneous precipitation are provided by the National Department of Civil Protection. In order to make the assimilation of radar volumes operational, intensive tests have been carried out, verifying the impact of the assimilation of both reflectivities and radial winds on the quality of the analysis and of the forecasts initialized from them. In this work, results in terms of QPF and near-surface variables verification are shown. Upper-air variables verification has also been performed, but results are not reported here for the sake of synthesis.

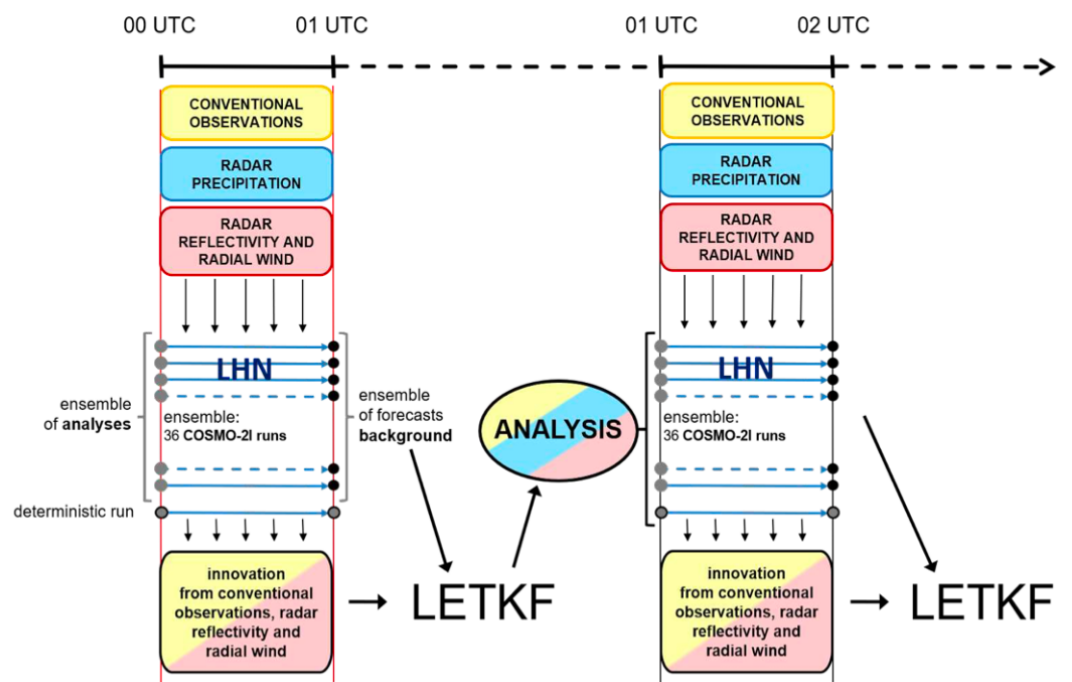
2. DATA ASSIMILATION

To improve weather forecasting, two mutually non-exclusive approaches can be chosen. The first involves improving the physics and dynamics of the model, while the second requires the improvement of the accuracy of the analysis, i.e. the initial condition from which to start the integration of numerical weather prediction (NWP) models. The analysis is achieved by combining the background state, provided by a short-term forecast which carries information from past observations into the current analysis, with observations via a data assimilation system (Kalnay, 2003).

2.1 DATA ASSIMILATION SYSTEM FOR COSMO-21

The Kilometer Ensemble Data Assimilation system (KENDA; Schraff, 2016), developed for the COSMO model by the homonymous consortium, is based on the Local Ensemble Transform Kalman Filter technique (LETKF; Hunt, 2007). Such a system has been implemented at Arpae-SIMC with hourly cycles in which both conventional observations (data from AIREP, TEMP and SYNOP) and radar volumes of reflectivity and radial wind are used. The assimilation ensemble consists of 36 members plus a deterministic run. A detailed description of the KENDA system adopted at Arpae-SIMC, schematized in Figure 1, is provided in Gastaldo et al. (2021).

Figure 1
Scheme of the data assimilation system employed to generate the analyses for COSMO-21 and COSMO-21-EPS at Arpae-SIMC.

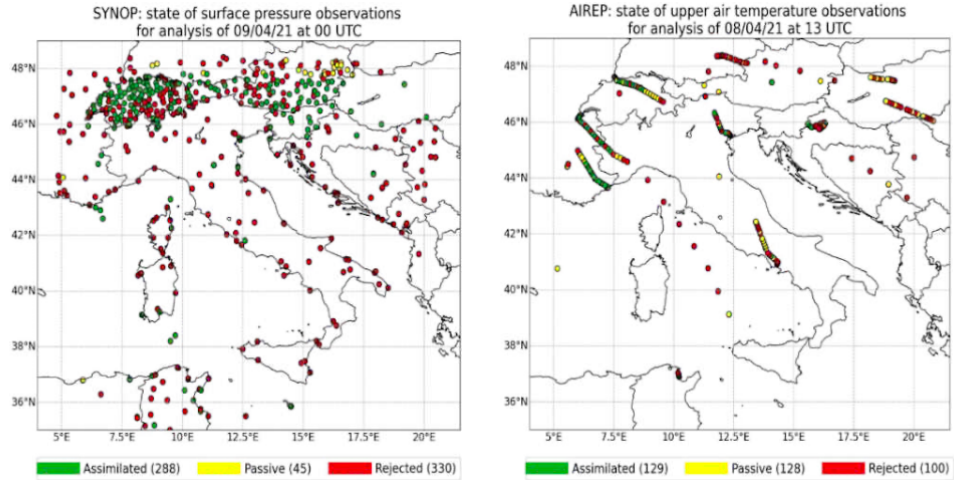


Radar data are not only assimilated as volumes, but also as instantaneous precipitation fields. The surface rainfall intensity (SRI) estimated by radar is assimilated using the latent heat nudging technique described in Stephan et al. (2008). As with any nudging technique, assimilation of this data occurs during the forecast cycle providing a background closer to the true state of the atmosphere.

2.2 ASSIMILATED OBSERVATION

Despite their importance, as they provide information on temperature, humidity and wind, conventional observations are spatially (and temporally) inhomogeneous, as shown in the example reported in Figure 2.

Figure 2
Observations from ground stations (left) and aircrafts (right) for two different moments. In the assimilation system, observations can be assimilated (in green), set to passive and used for diagnostics (in yellow) and rejected (in red).



On the other hand, the radar composite uniformly covers a large part of the integration domain of the model (Figure 3). It has a very high time frequency of 5 minutes and a horizontal resolution of 1 km.

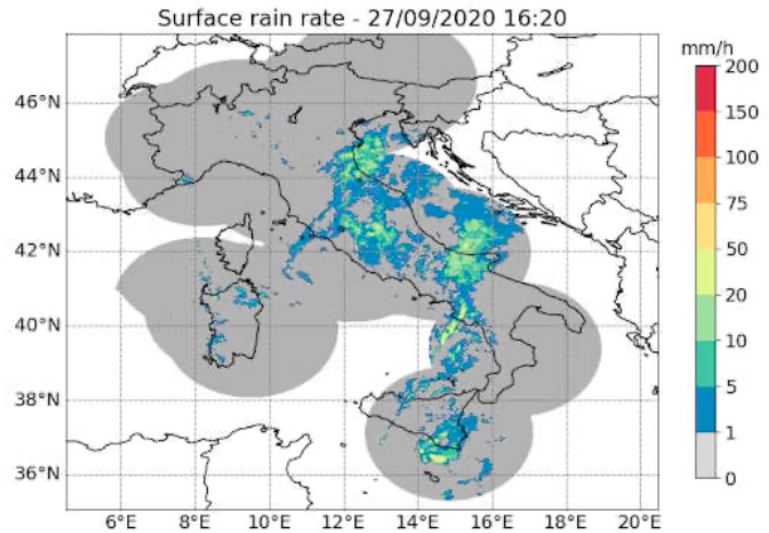


Figure 3
Surface rainfall intensity estimated from the Italian radar composite.

Radar volumes also allow to gather information on the state of the atmosphere in large areas and at high temporal frequency. Moreover, compared to the precipitation radar composite, they provide observations at different altitudes. Radar volumes have an original bin resolution of 1 km, but, due to the hypothesis of uncorrelated observation errors and to time constraints computation, they are superobbed at 10 km. Of the entire Italian radar network, currently, volumes from 11 radars, depicted with solid lines in Figure 4, are assimilated.

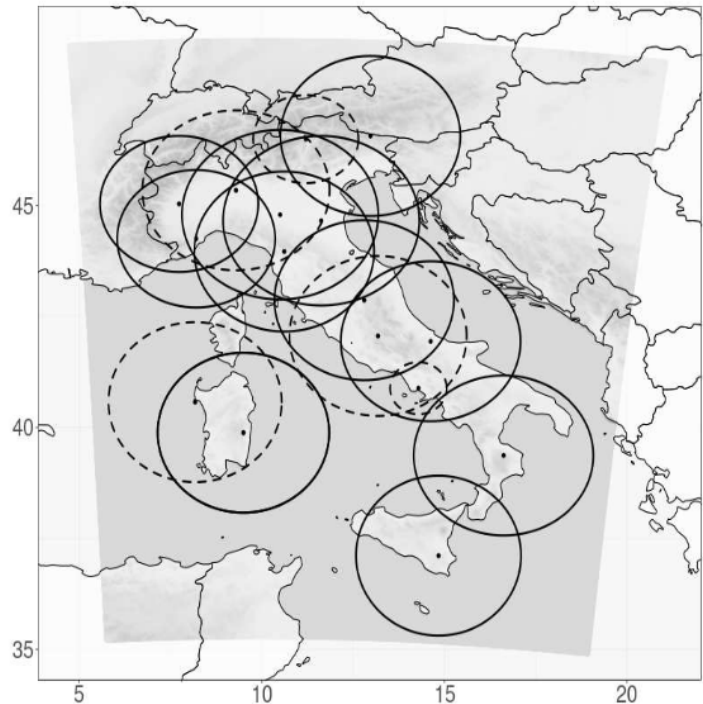


Figure 4

Italian radar network. Solid lines indicate radars for which reflectivity and radial wind volumes are assimilated.

In the assimilation scheme, data are assimilated with different frequencies. Conventional data are all taken into account, while only radar volumes closest to the analysis time are used. In the LHN scheme, the SRI is assimilated every 10 minutes.

3. IMPACT OF DATA ASSIMILATION ON FORECASTS

To evaluate the impact of assimilating different observation types, four configurations have been tested:

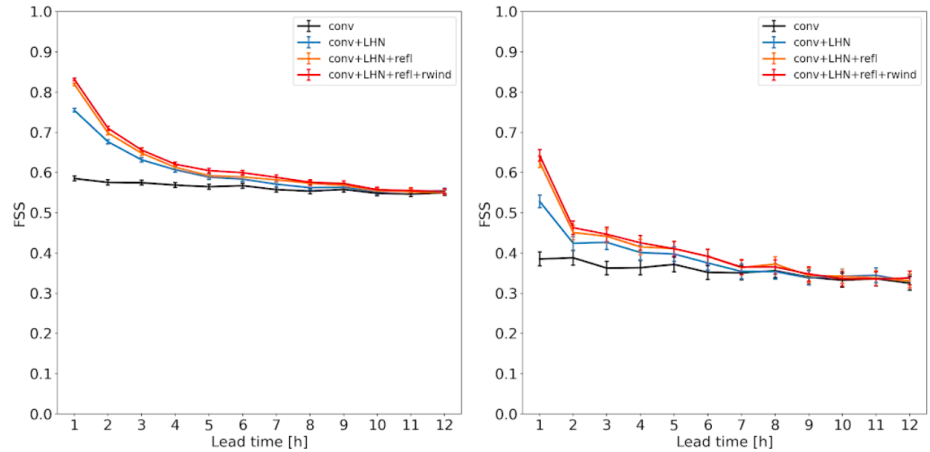
- conv: assimilation of conventional observations only (black);
- conv+LHN: assimilation of conventional observations + LHN of SRI composite (blue);
- conv+LHN+refl: assimilation of conventional observations + LHN of SRI composite + reflectivity volumes (yellow);
- conv+LHN+refl+rwind: assimilation of conventional observations + LHN of SRI composite + reflectivity and radial winds volumes (red).

A deterministic forecast is initialized every 3 hours from the analyses generated by each configuration. In the following, the verification of these forecasts is reported, considering two evaluation periods (one from 19 September 2020 to 20 October 2020, the other from 11 November 2021 to 13 December 2021) characterized by both convective and stratiform precipitation. Results over these two periods are merged to give a single outcome over the whole two-months evaluation period.

3.1 QPF VERIFICATION

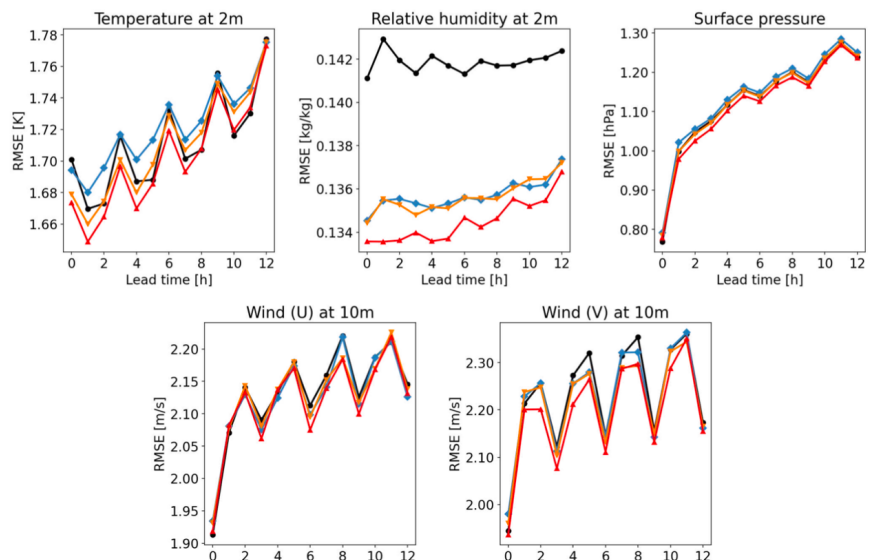
Forecast hourly accumulated precipitation has been verified using the Fractions Skill Score (FSS; Roberts and Lean, 2008) by considering cells with a resolution of 0.2° both in latitude and longitude and different thresholds. A perfect forecast has FSS equal to 1. Radar-estimated precipitation adjusted with rain gauges is employed as observation. Results for the 0.5 and 5 mm thresholds are shown in Figure 5, where the vertical bars at the forecast hours indicate the 95% confidence level estimated by a bootstrap technique.

Figure 5
FSS verification of precipitation over Italy for the threshold of 0.5 mm (on the left) and 5 mm (on the right) for conv (black lines), conv+LHN (blue), conv+LHN+refl (yellow) and conv+LHN+refl+rwind (red) experiments. Vertical bars indicate 95% levels of confidence.



The conv experiment (black line), in which only conventional observations are assimilated, was performed only to quantify the improvement when radar data are also assimilated. The blue line, conv+LHN, was the operational version until March 2021. Compared to the black line, it shows a clear improvement in forecast quality up to the tenth hour for the 0.5 mm threshold and to the seventh hour for the 5 mm threshold. This improvement is statistically significant up to the seventh hour for the lowest threshold and up to the fourth hour for the highest one. In March 2021, the assimilation of reflectivity volumes was implemented operationally, further improving the quality of forecasts in the first hours and in particular for the highest thresholds. For the 5 mm threshold, the most significant improvement is at the first lead time. In March 2022, the further assimilation of radial winds in the operational framework enabled another, albeit minor, improvement, especially for the lower thresholds.

Figure 6:
RMSE for temperature at 2 m (on the top left), relative humidity at 2 m (on the top center), surface pressure (on the top right), and the horizontal components of wind (on the bottom) for conv (black lines), conv+LHN (blue), conv+LHN+refl (yellow) and conv+LHN+refl+rwind (red) experiments.



3.2 NEAR-SURFACE VARIABLES VERIFICATION

In Figure 6 the root mean square errors (RMSE) for surface pressure, temperature and relative humidity at 2 m and horizontal wind components at 10 m are shown for all the different configurations. The assimilation of radar data only via LHN (conv+LHN experiment) improves the RMSE compared to conv for the relative humidity, while it has a negative impact on temperature and a substantially neutral impact on the other variables. A significant improvement in RMSE scores is obtained when also radar volumes are assimilated, especially when both reflectivities and radial winds are employed. In fact, conv+LHN+refl+rwind configuration provides the best RMSE scores for all the variables considered.

4. CONCLUSIONS

The COSMO-2l model is one of the few numerical models in which radar volumes of reflectivity and radial winds are assimilated directly. Assimilation of radar data results in improved forecast quality for precipitation, upper and middle troposphere variables (not shown here) and near-surface variables. More accurate forecasts lead to an improved support to forecasters both in forecasting, with the issuing warnings, and in the monitoring phase, particularly in the case of intense events characterized by rapid evolution. Given the good results obtained, the same type of assimilation will also be implemented for the ICON model, which will replace the COSMO model, while also evaluating the increase in horizontal resolution and the frequency of assimilation cycles.

ACKNOWLEDGMENTS

The authors would like to thank the National Civil Protection Department for providing the data of the national radar network and Dr. Anna Fornasiero for her supply of rain gauge-adjusted radar fields.

REFERENCES

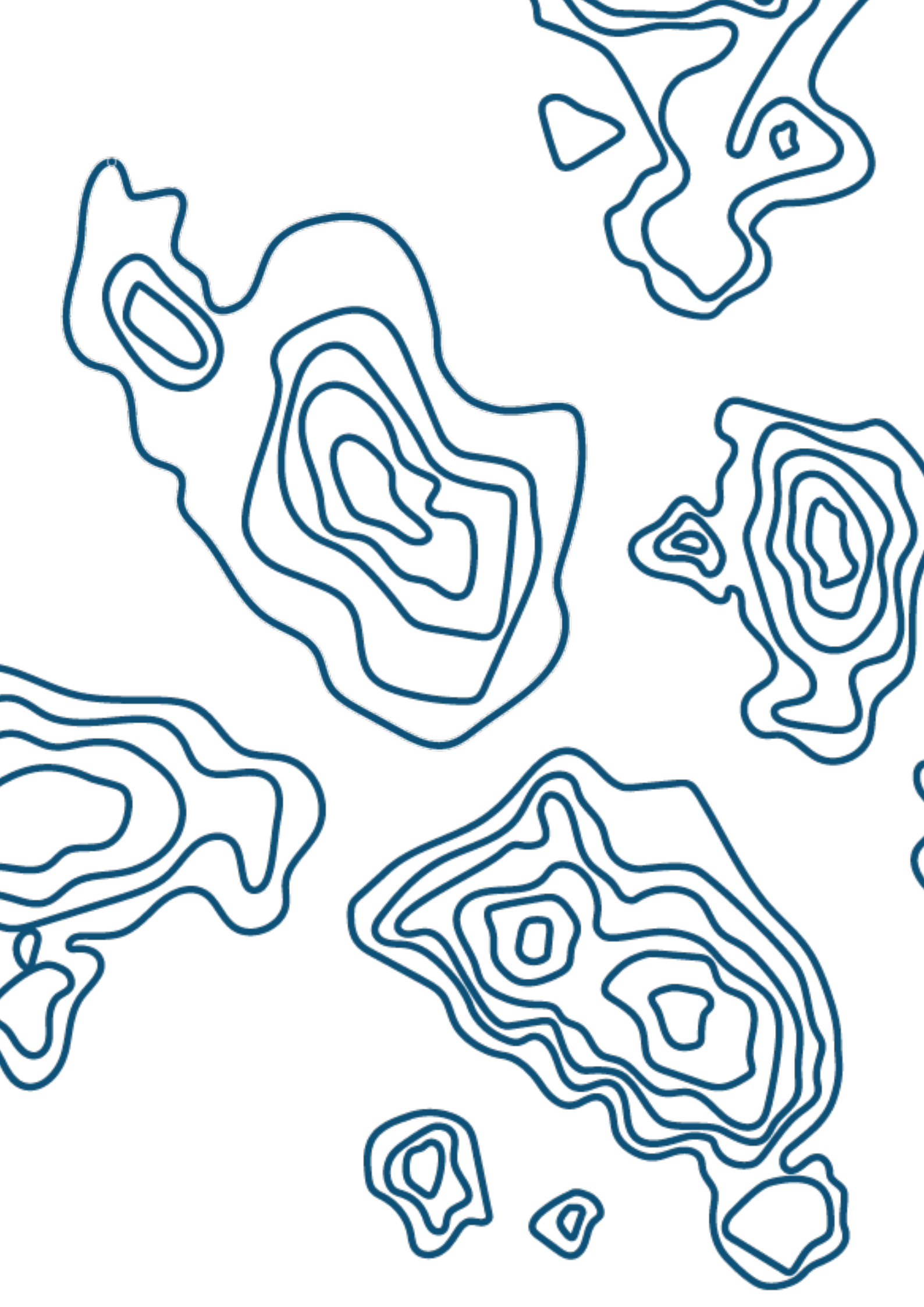
- Gastaldo, T., Poli, V., Marsigli, C., Cesari, D., Alberoni, P.P., Paccagnella, T. Assimilation of radar reflectivity volumes in a pre-operational framework. *Q J R Meteorol Soc.* 2021; 147: 1031–1054. <https://doi.org/10.1002/qj.3957>, 2021.
- Hunt, B. R., Kostelich, E. J., and Szunyogh, I.: Efficient data assimilation for spatio-temporal chaos: A local ensemble transform Kalman filter, *Physica D: Non-linear Phenomena*, 230, 112–126, <https://doi.org/10.1016/j.physd.2006.11.008>, data Assimilation, 2007.
- Jones, C.D. and Macpherson, B. (1997) A latent heat nudging scheme for the assimilation of precipitation data into an operational mesoscale model. *Meteorological Applications*, 4, 269–277.
- Kalnay, E. (2003). *Atmospheric modeling, data assimilation and predictability*. Cambridge university press.
- Roberts, N. M. and Lean, H. W.: Scale-Selective Verification of Rainfall Accumulations from High-Resolution Forecasts of Convective Events, *Monthly Weather Review*, 136, 78–97, <https://doi.org/10.1175/2007MWR2123.1>, 2008.
- Schraff, C., Reich, H., Rhodin, A., Schomburg, A., Stephan, K., Perianez, A., and Potthast, R.: Kilometre-scale ensemble data assimilation for the COSMO model (KENDA), *Quarterly Journal of the Royal Meteorological Society*, 142, 1453–1472. <https://doi.org/10.1002/qj.2748>, 2016.
- Stephan, K., Klink, S. and Schraff, C. (2008) Assimilation of radar-derived rain rates into the convective-scale model COSMO-DE at DWD. *Quarterly Journal of the Royal Meteorological Society*, 134, 1315–1326. <https://doi.org/10.1002/qj.269>.

RADAR OPERATIONS AND NETWORKS

Centralisation in mainland France of the weather radar data processing system for the French overseas territories

Revision of the integration of disdrometers to improve the quality of the products at the coast





CENTRALISATION IN MAINLAND FRANCE OF THE WEATHER RADAR DATA PROCESSING SYSTEM FOR THE FRENCH OVERSEAS TERRITORIES

Dominique Faure¹, Axel Deloncle¹, Isabelle Sanchez², Sylvain Chaumont¹, Jean Millet¹, H el ene Pech², Val erie Vogt¹, B eatrice Fradon¹, Nicolas Gaussiat¹

July 07, 2022

¹Centre de M eteorologie Radar, METEO-FRANCE, Toulouse, France

²MSI (IT department), METEO-FRANCE, Toulouse, France

ABSTRACT

Since April 2018, M et eo-France has been using a new centralised radar data processing system named SERVAL, to concentrate and process the raw polar data provided by the metropolitan France network of 31 weather radars (S, C, and X bands, all Doppler and Dual- Pol). This communication presents the extension of this centralised processing system to the French overseas territories. The concerned territories include French Antilles in the Caribbean Sea, French Guiana in South America, R eunion Island in West Indian Ocean, New Caledonia in the Southwest Pacific Ocean, and Mayotte in the Comoros archipelago in the near future. A real time data transfer was established to concentrate raw data at the Toulouse Radar Center after each radar antenna rotation completed. SERVAL was updated to process metropolitan radar data and overseas radar data in parallel, and to provide composites for each territory. An outbound data transfer delivers the final radar products to the M et eo-France offices and to end users in overseas territories, where these products are available in few minutes. Operational production rates and products delivery times are presented, as the system safety in the event of an interruption of telecommunications between overseas territories and mainland France.

1. INTRODUCTION

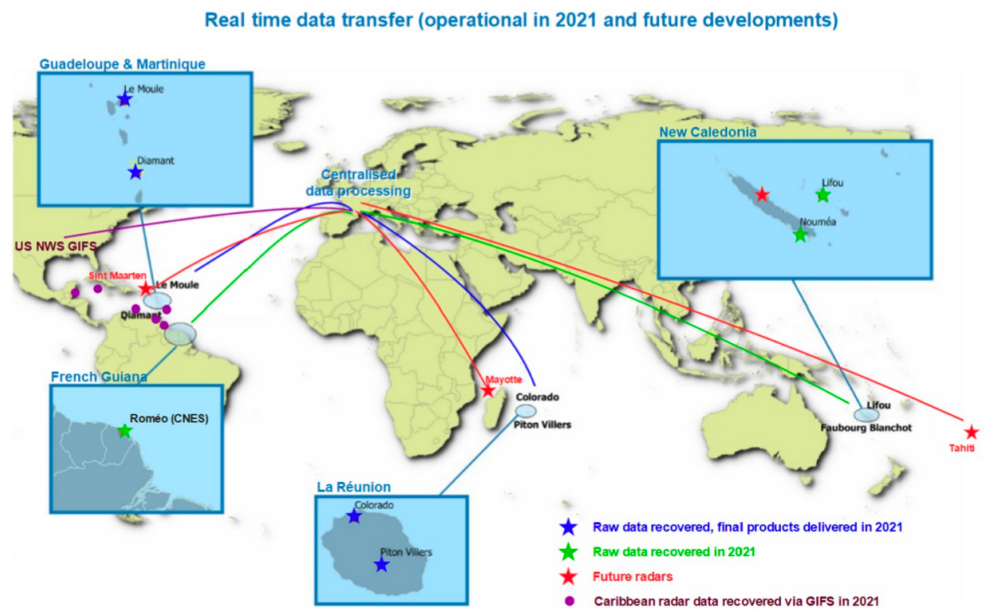
M et eo-France operates a various radar network, with S, C and X band radars, in plains and mountainous region in mainland France, but also in small islands in overseas territories in three oceans. Besides, M et eo-France also uses radar products of partners from neighbouring countries to complete composite products. Historically, the single radar production was realised by the software operating each radar, and the radar composite production was realised in regional centres in metropolitan France and in each overseas territory. Since April 2018, M et eo-France has been using a new centralised radar data processing system named SERVAL (Vogt et al 2018), to concentrate and process in Toulouse (Southwestern mainland France) the raw polar data provided by the metropolitan France network of 31 weather radars. Since September 2021, this centralised processing system has been extended to the French overseas territories. The interests are multiple: facilitating the maintaining and the deployment of

new up-to- date versions of the data processing software, reinforcing the standardisation of the radar products, centralising the IT system of Météo-France. One can note that the context in small islands makes particularly difficult the quantitative precipitation estimation (QPE), on account of small distances between the areas of interest and the radars, an important relief in each island inducing large beam blocking and ground clutters, and a close frontier between maritime and terrestrial domains. R&D works are ongoing to upgrade the QPE process in these small islands.

2. OVERSEAS RADAR NETWORK DESCRIPTION

All the Météo-France overseas radars are S band radars. Météo-France operates radars in French Antilles in the Caribbean (Guadeloupe and Martinique islands), Reunion Island in West Indian Ocean, New Caledonia in the Southwest Pacific Ocean, and concentrate raw data from the CNES radar in French Guiana in South America (Figure 1).

Figure 1
Overseas radar network and data transfer. Remark: in green, raw data is recovered, but the final products are not delivered for now; in red radars planned for the next few years.



Since September 2020, raw radar data has been recovered for all the Météo-France overseas radars (New Caledonia included), and processed at the Centre of Radar Meteorology (CMR) in Toulouse. The final radar products have been delivered in French Antilles and Reunion Island since September 2021. In order to contribute to a Caribbean radar composite, several products from Caribbean radars have been also recovered via the GIFS service (The Global Telecommunications System Internet File Service, provided by the U.S. NWS for WMO Regional Association IV – RA- IV). The SERVAL Caribbean radar composite is pushed to the GIFS service. The system will continue to be extended in the future. After that all three New Caledonian radars will be installed, the radar products for New Caledonia will also be delivered in New Caledonia. A new partner radar will be installed in the Saint Martin Island in the northeastern Caribbean Sea, and two new Météo-France radars will be installed in Mayotte in the Comoros archipelago (Indian Ocean, 2025) and possibly in Tahiti in French Polynesia in the central part of the Pacific Ocean.

3. SYSTEM OPERATION

Météo-France operates all radars with a 3×5 minutes volume scan strategy based on PPIs (plan position indicator). The lowest elevation angles are repeated every five minutes, and the most elevated angles are repeated every fifteen minutes alternating their values each five minutes (example in table 1).

5 minutes sub-cycles	Elevation angles
5 minutes sub-cycle 1	90° / 4.4° / 3° / 1.6° / 0.8° / 0°
5 minutes sub-cycle 2	12° / 4.4° / 3° / 1.6° / 0.8° / 0°
5 minutes sub-cycle 3	6° / 4.4° / 3° / 1.6° / 0.8° / 0°

Table 1

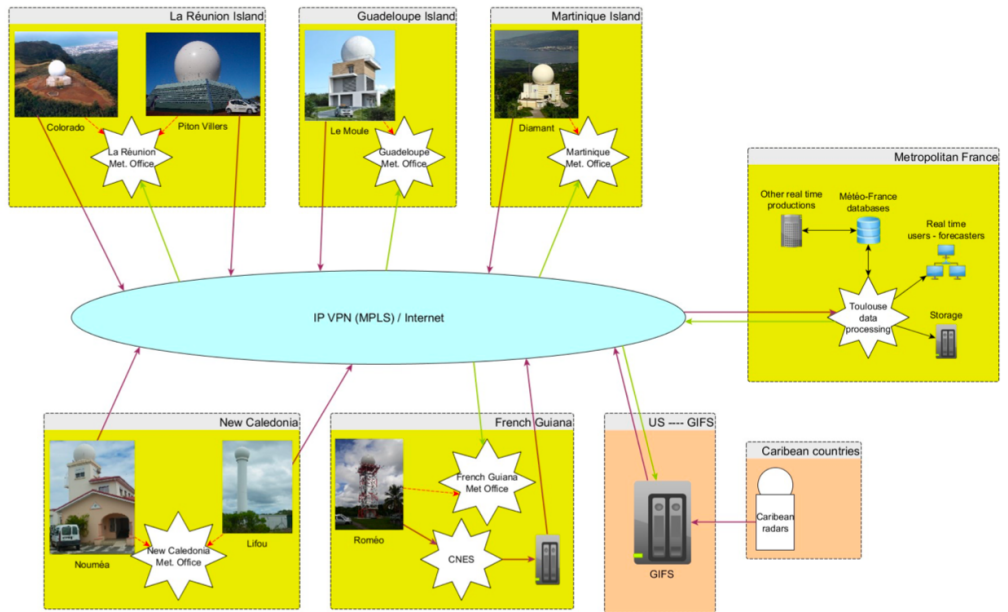
Elevation angles used for Le Moule radar (Guadeloupe).

A continuous data transfer has been established to concentrate each PPI of raw data directly in Toulouse after each radar antenna rotation completed (Fig. 2). The data transfer uses different networks depending on the overseas location (IP VPN (MPLS) or Internet). Every 5 minutes SERVAL processes all the raw volume data received from each radar during the last 5 minutes, with the possibility to use all data available in the Météo-France databases. This data processing provides both volume radar products, and 2D radar products as reflectivity at lowest usable altitude and quantitative precipitation estimation at ground level (Vogt et al 2018). These single-radar products are then merged in composites covering the concerned regions (Antilles, the Caribbean, La Reunion Island, New Caledonia). The final standard radar products are then delivered to each overseas region. These radar products are also directly at disposal in Toulouse for other production tasks, in order to use it into downstream productions designed for specific purposes or customers. In the event of an interruption of telecommunications between an overseas territory and mainland France, a safety product is pushed directly from the radar to the local Météo-France office. One can note that in such a situation, all weather services would rapidly be severely degraded in the concerned territory, so the local radar images become important. One can note that a SQL database and an interactive Web interface has been designed to facilitate SERVAL administration, production supervision and monitoring, with an extensive display of intermediate or final products (more than 220 images by radar every 5 minutes). This is a great improvement for the overseas radar production. SERVAL also easily allows to realise an off line data processing (time-deferred), for studies, reanalysis, or R&D works.

4. SYSTEM PERFORMANCE

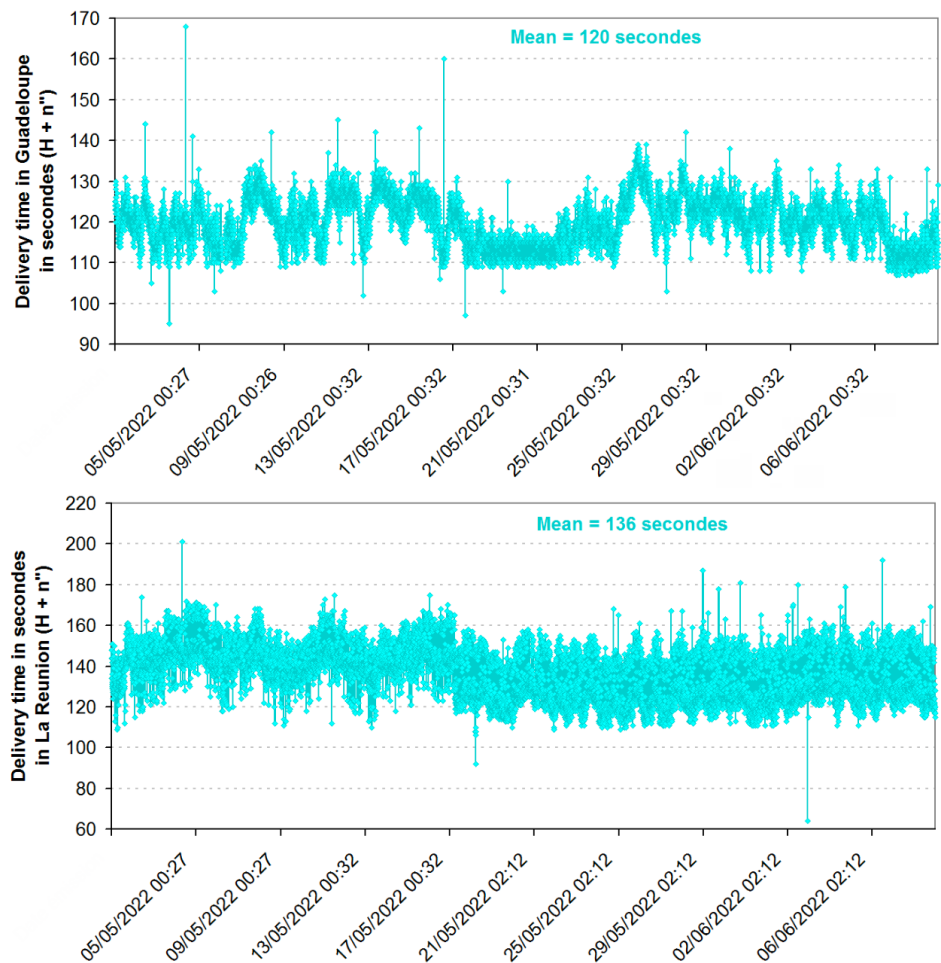
Each 5 minutes SERVAL processes the raw data received during the last 5 minutes from H-5' to H (H standing for the time step considered). The time when the last PPI is received in Toulouse depends on the number of PPI constituting the 5 minutes raw volume data for a radar. With 5 PPI or less, in general the last PPI is received before the time H because the radar acquisition ends early. For six PPI per 5 minutes, the last PPI is received in Toulouse few seconds after the time H. After the processing, the final standard products are available in Toulouse before H+2.5' (depending on the amount of precipitation), and available in overseas territories before H+2.5' or H+3' (H+2'40" in La Reunion during the intense tropical cyclone Batsirai, 2 February 2022). Figure 3 give two examples of delivery time for

Figure 2
IT structure. In brown, raw data transfers to Toulouse after each antenna rotation. In green, final standard radar products sent from Toulouse every 5 minutes. In red, the safety products in case of interruption of telecommunications between mainland France and an overseas territory. For New Caledonia, the final radar products are not delivered for now.



single-radar products in May 2022. Until the end of the year 2022, the two productions will be delivered in parallel to help the users to move from the old products to the new products, which allows to compare the rate of the two productions. The centralised production rate is virtually the same as the previous local production rate in each overseas territory (table 2).

Figure 3
Delivery time of the 5min-1km QPE products, at the top for Le Moule radar in May 2022 (mean time = $H+2'$), at the bottom for Piton Villers radar in May 2022 (mean time = $H+2'16''$).



Radar: product	New rate/old rate
Le Moule: 5min-1km QPE (Guadeloupe)	100.27%
Diamant: 5min-1km QPE (Martinique)	100.06%
Colorado: 5min-1km QPE (La Réunion)	100.03%
Piton Villers: 5min-1km QPE (La Réunion)	99.78%

Table 2

New centralised production rate when the radar is running, in comparison with the old one (ratio of the two production rates: new production rate / old production rate, stated in percent). Example for the quantitative precipitation estimation (QPE) by radar (October – December 2021).

5 CONCLUSIONS

The extension of the centralised processing system SERVAL to the French overseas territories has been completed for Antilles and La Reunion, and is underway for the French Guiana where the CNES is changing its radar. For New Caledonia, all raw data is retrieved in Toulouse, but the finalisation of the transition is postponed until the current old radars are replaced. The results of this project show a performance at least at the level of the preceding production system in terms of production rate (only a few images are missing by month when the radar is running), and the delivery time of the final products is lower than the one requested. Besides, the move to the SERVAL software for the data processing conduces to observe an increase in quality of the radar products, the preceding local software having not evolved for many years. Now, all the productions or services using overseas radars products are evolving to assimilate the new SERVAL products to replace the old ones, the expected deadline for this moving being the end of 2022. Until this deadline, the two productions will continue to be delivered in parallel.

ACKNOWLEDGMENTS

About thirty teams from different department of Météo-France were involved in this project, in Toulouse in metropolitan France and in Guadeloupe, Martinique, or La Réunion. Without each of them this project could not have been realized.

REFERENCES

• V. Vogt, N. Gaussiat, M. Martet, J. Millet, I. Pfaffenzeller, S. Chaumont, B. Fradon, *SERVAL: a centralized processing platform for the French radar network*, 10th European Conference on Radar in Meteorology & Hydrology (ERAD2018), 1-6 July 2018, Netherlands.

REVISION OF THE INTEGRATION OF DISDROMETERS TO IMPROVE THE QUALITY OF THE PRODUCTS AT THE COAST

Maruri MaM^{1,2}, Barturen M², Aranda J^{3,4}, Gaztelumendi S¹, Orúe J¹

August 5, 2022

¹Tecnalia Basque Research and Technology Alliance (BRTA)- Meteo & Climate Area, Zamudio, Spain

²University of the Basque Country UPV/EHU, Bilbao, Spain

³DAEM / Basque Meteorology Agency, Gasteiz, Spain

ABSTRACT

It is not easy to find a site to install a weather radar in a complex terrain. Besides there are many regulations that it must obey, and no site fulfills 100% of the hydrometeorological objectives. The site of Kapildui is one of these cases. After more than fifteen years of operation, optimization of the operation, improvements in the lightning protection system, new products adapted to the needs, and a large historical database, today there is still an increase in new users and applications. The Basque Country is located at the north of the Iberian Peninsula. The higher density population is at the coast. At the north of the region is placed one of the great maritime Port of Spain, "Bilbao Port", but the Kapildui weather radar is at the south, at the top of the Kapildui Mountain. The view of the coastal hydrometeorological phenomenon is limited for the geometry of the radar beam and the scan operation (that avoid the obstacles of a complex terrain). For this reason, the weather data from Kapildui needs other meteorological sources such as, a high dense hydrometeorological network, other radars, and recently is being evaluated the integration of disdrometers to improve the quality of the data at this distance and at this point. The huge amount of data registered from the disdrometers at the coast combined with the complexity integration of weather radar data, demand a study in two directions, validation of the quality of the disdrometers data and analyze the best way to integrate both systems, in different meteorological conditions. The present work studies, the issues found and the benefits of using this data in maritime applications.

1. INTRODUCTION

The radar of Kapildui was installed in 2005, is a Meteor 1500C weather radar, C band, Doppler and polarimetric. However, it has a polarimetric limitation due to the hardware features, the signal processor can only process differential reflectivity (Aranda & Morais, 2006) (Gaztelumendi, y otros, 2006). The Basque Country has a complex topography, and this makes it very difficult to implement observation systems that have a good representativeness of their measurements for the whole region. Amongst the observation systems of the directorate attention of emergency and meteorology, DAEM, is the Kapildui weather radar, which complements its

information with the Jata weather radar located on the coast (Gaztelumendi, Otxoa de Alda, Egaña, & Gelpi, 2006) (AEMET, 2022), and there is also a dense network of automatic surface stations with more than 100 points distributed throughout the region (Gaztelumendi, y otros, 2012). Within the large network of stations, only a few, those that best meet WMO specifications, are considered benchmarks and these are being configured to provide high quality and high-resolution information, adding new observation systems such as disdrometers (Euskalmet, 2022) (Nemeth & Martin, OTT PARSIVEL ® Enhanced precipitation identifier for present weather, drop size distribution and radar reflectivity - ott messtechnik, germany, 2006).

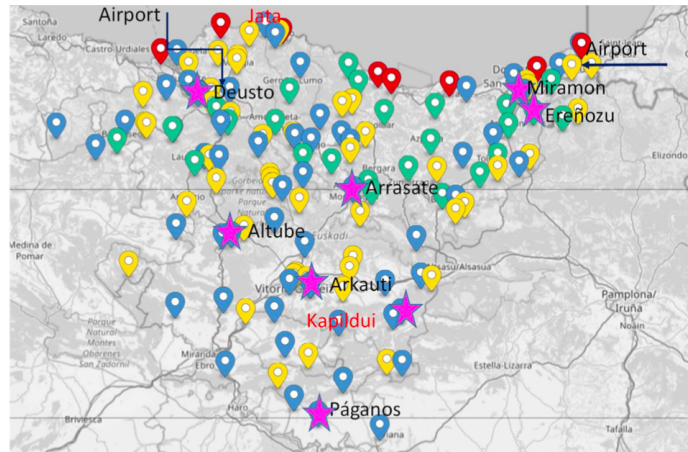


Figure 1
Automatic Weather Stations network (DAEM). Red Text (Weather radars). Black Text (Disdrometers). Arrows (Airports)

Numerous efforts have been made to obtain the best data for the monitoring and surveillance of adverse episodes that can lead to floods, traffic accidents, etc., but always accompanied by material losses and damage. As can be seen in the graph and regardless of the negative growth of recent years, the population is distributed near the capitals (Eustat. Instituto Vasco de Estadística, 2022), in the valleys, while the accumulated rainfall is greater in the north where the largest population centres are located in the greater Bilbao and Donosti (San Sebastian) and one of the busiest ports in Spain, the "Port of Bilbao" (Puerto de Bilbao, 2022).

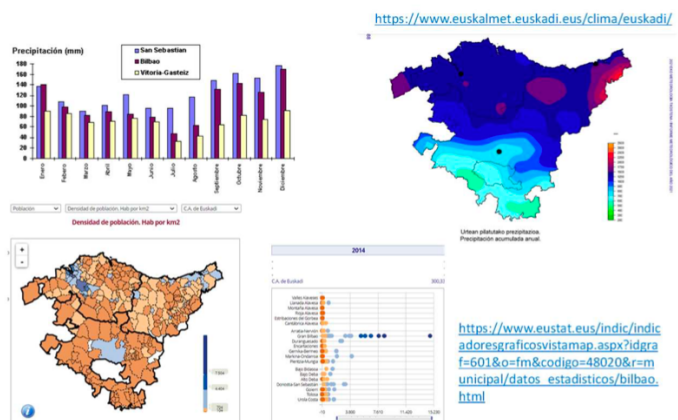


Figure 2
Information from Eustat

The estimation of surface precipitation from radar data is one of the most widely discussed topics over the years (Harrison, Driscoll, & Kitchen, 2000). (Belmonte & Bellini Saibene, 2017). There are many proven techniques and observations used to correct and provide a map that is close to reality and that can be used in different applications from hydrological, agricultural, water consortium to others that seek products made for decision making (WMO, 2022). In times of resilience where attacks on social welfare and the meteorological severity of some episodes put the economy at risk, having the most complete quality information and knowing how to use it is a challenge. In this context, the aim of the present work is to validate the disdrometer information in order to subsequently evaluate its integration in other observation systems such as the Kapildui radar. In a first phase, points near the coast are studied, where the radar geometry and the quality of the data is poor. The incorporation of new measures is always a great help in detecting errors, deviations and improving the quality of the final product, but they require prior studies to evaluate and define the best way to combine these measures. In this way, the contributions of both systems can be controlled, without losing control of the data.

2. INPUT DATA

The work will use information from previous studies from the disdrometer (Ángulo-Martínez, Beguería, Latorre, & Fernández Raga, 2018) (Nemeth & Beck, 2011), (Sintes & Joan, 2022) (Friedrich, Kalina, & Aikins, 2016) (Löffler-Mang & Joss, 2000) and the rawest data from the year 2021, from the recent DAEM disdrometer network. In addition, the information from the METAR files of the airports that have been recorded by the radar itself will be taken into account as reference information. Given the interest in validating the information in the coastal area and the use of METAR archives, the work focuses on the study of the closest disdrometers to the METAR stations located at the airports of Bilbao and Hondarribia (AEMET, 2021). The quality of the radar data at these selected points is evaluated in order to improve the estimation of surface precipitation at these points of high population and economic density.

3. METHODOLOGY

The first phase of the methodology focuses on the validation of the data of the disdrometer with minute resolution. For this purpose, information from the manuals (OTT HYDROMET, 2016) and from the literature associated with the disdrometer studies is used. The parameters provided by the disdrometer in a minute resolution data should be divided into raw-data parameters and into derived data obtained from the raw-data parameters. However, since the information from the manual is insufficient to provide explanations and inconsistent with the information recorded by the disdrometer in terms of the raw data recorded it was decided to work only with the minute derived data. In a second phase, the information from the disdrometer is validated taking as a reference the METAR data (Agencia Estatal de Meteorología, 2022) and meteorological information from the area that is necessary, considering the differences between the different measurement systems. The METAR data have a resolution of 30 minutes and allow more types of hydrometeors to be differentiated and provide more complete information on the weather in the area. In a third phase, the uses of the disdrometer and its application to weather radar are studied.

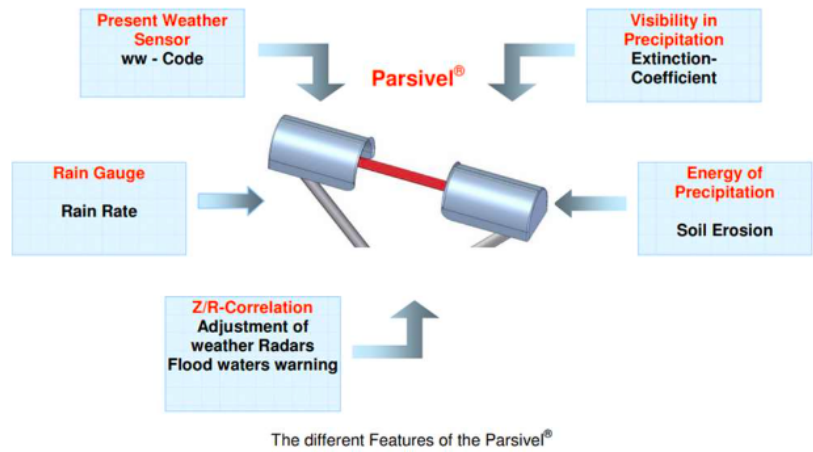
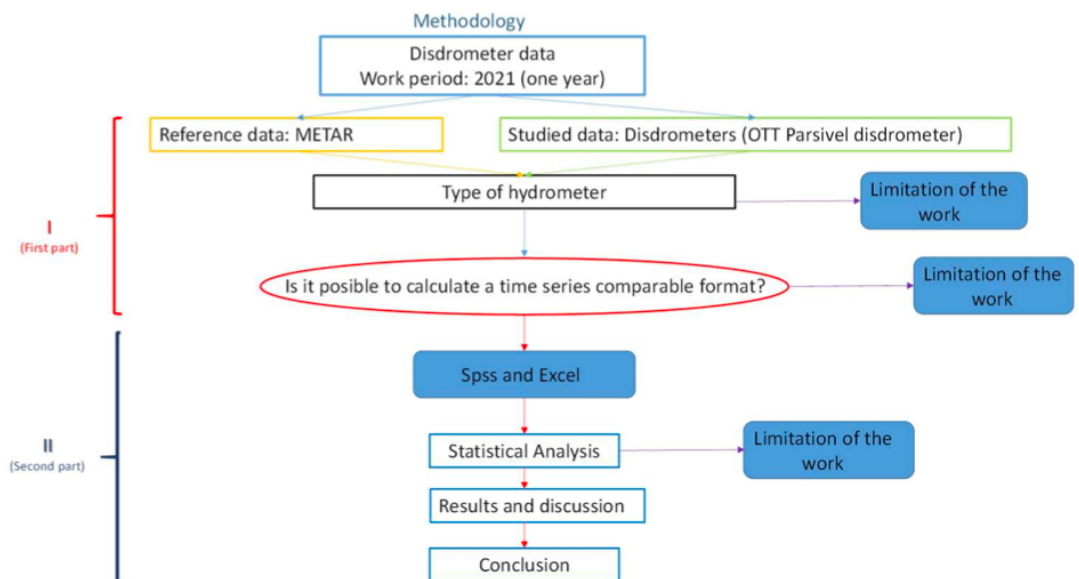


Figure 3
Applications of the disdrometer. (Nemeth & Beck, 2011)

Numerous efforts have been made to obtain the best data for the monitoring and surveillance of adverse episodes that can lead to floods, traffic accidents, etc., but always accompanied by material losses and damage. As can be seen in the graph and regardless of the negative growth of recent years, the population is distributed near the capitals (Eustat. Instituto Vasco de Estadística, 2022), in the valleys, while the accumulated rainfall is greater in the north where the largest population centres are located in the greater Bilbao and Donosti (San Sebastian) and one of the busiest ports in Spain, the "Port of Bilbao" (Puerto de Bilbao, 2022). The influence on the impact of the operation scans on the quality of the radar products at the coast is evaluated. The Scanning geometry at the coast, Beam blockage derived of the complex terrain and a dense network of surface stations, vs. the recent network of disdrometer stations of the Kapildui Weather radar are considered together. In a fourth and final phase, the data from both disdrometers and the Z/R values that can be derived from them are compared.

Figure 4
Methodology. Two different parts, the first one is related to the codification and verification of the data to a common format and the second is the analysis of the data.



4. RESULTS

The results are presented according to the approach of each of the phases of the methodology. First phase: General statistics of the series used in the data analysis

Figure 5
Common format
Common format
according to the
manual information.
Exploration of the
registered variables.

	Estadísticos descriptivos											
	N	Rango	Mínimo	Máximo	Media	Desv. estándar	Varianza	Asimetría	Curtosis	Error estándar	Error estándar	
	Estadístico	Estadístico	Estadístico	Estadístico	Estadístico	Estadístico	Estadístico	Estadístico	Estadístico	Estadístico	Estadístico	
Rainint01D	42970	87.282	.007	87.289	1.49544	.015860	3.287671	10.809	9.508	.012	155.833	.024
Z07D	42970	67.611	-7.947	59.664	18.85444	.050454	10.458785	109.386	.043	.012	-.586	.024
MOR08D	42970	19989	11	20000	13769.75	32.817	6802.616	46275582.282	-.491	.012	-1.405	.024
NPartDetectValidate11D	42970	3666	6	3672	276.82	1.840	381.462	145513.490	3.043	.012	12.327	.024
NPartDetect60D	42970	3721	6	3727	280.65	1.862	385.886	148908.091	3.026	.012	12.169	.024
ListNPart61D	42970	162	128	290	205.16	.013	2.610	6.811	-6.551	.012	233.342	.024
N válido (por lista)	42970											

	Estadísticos descriptivos											
	N	Rango	Mínimo	Máximo	Media	Desv. estándar	Varianza	Asimetría	Curtosis	Error estándar	Error estándar	
	Estadístico	Estadístico	Estadístico	Estadístico	Estadístico	Estadístico	Estadístico	Estadístico	Estadístico	Estadístico	Estadístico	
Rainint01M	58214	107.772	.007	107.779	1.55865	.013617	3.285531	10.795	8.167	.010	123.060	.020
Z07M	58214	64.653	-6.763	57.890	18.00228	.045428	10.960596	120.135	.073	.010	-.672	.020
MOR08M	58214	19831	169	20000	12544.78	29.608	7143.756	51033252.400	-.219	.010	-1.628	.020
NPartDetectValidate11M	58214	3959	6	3965	376.63	1.963	473.649	224343.041	2.380	.010	6.843	.020
NPartDetect60M	58214	3981	6	3987	380.55	1.979	477.400	227911.232	2.373	.010	6.788	.020
ListNPart61M	58214	334	129	463	205.43	.011	2.666	7.110	22.480	.010	2047.392	.020
N válido (por lista)	58214											

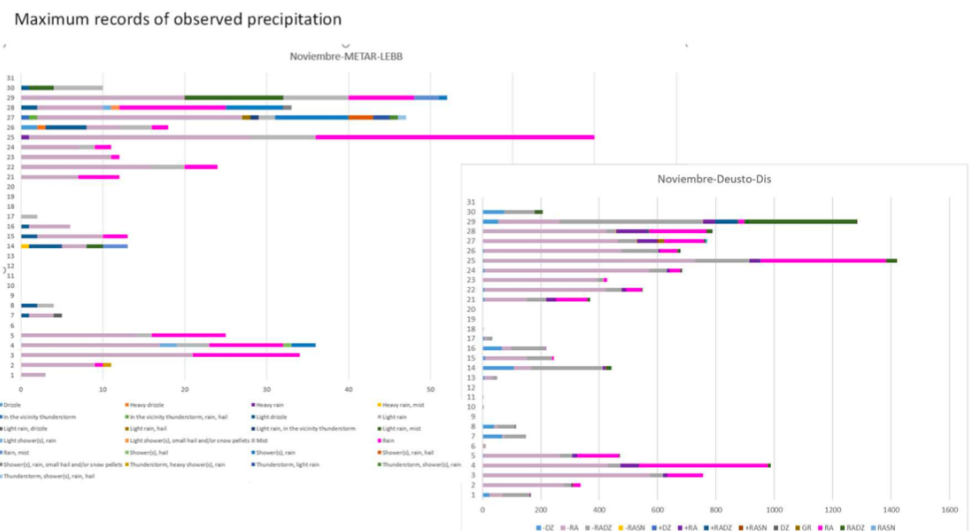
11.2 Measured value numbers

The measurements and status values are output from the Parsival in the form of a telegram. To this end, each value that can be output was assigned a measurement number. In addition, the number of digits that the value in the telegram can contain, the form in which this value is output and in what units is previously defined. These specifications are listed in the following table:

Measured value No.	Description	Digits	Form	Units
01	Rain intensity (32 bit)	8	0000.000	mm/h
02	Rain amount accumulated (32 bit)	7	0000.00	mm
03	Weather code according to SYNOP w/w, Table 4680	2	00	1
04	Weather code according to SYNOP ww, Table 4677	2	00	1
05	Weather code METAR/SPECI w/w, Table 4678	5	+RASN	1
06	Weather code according to NWS Code, Table 4679	4	RLS-	1
07	Radar reflectivity (32 bit)	6	00.0000	dBz
08	MOR visibility in the precipitation	4	0000	m
09	Sample interval	5	00000	s
10	Signal amplitude of the laser strip	5	00000	1
11	Number of detected particles	5	00000	1

Second phase: General statistics of the METAR series and comparison with the Disdrometer records. The most relevant aspect of this comparison is the complexity itself due to the different nature of the data. After the month-by-month study, different case studies are proposed, the first case selected being the one with the most records "25 November 2021".

Figure 6
The daily maximum of
the total 1 minute
records were registered
on 25th November
2021. Example: Deusto
station registered more
than 1400 records in
one day Versus
Sondika METAR
records with more than
48 (70 aprox.)



Third phase: Radar operation and strategies in the use of disdrometers. There are two uses contemplated in this paper: system monitoring and Z/R adjustment for surface precipitation products. The exploitation of the raw data from the disdrometer to determine the variability of the composition, through the number of particles detected, is left for later studies due to the complexity of the information and the doubts raised with the manufacturer.

Figure 7
The greater differences are found with small particles and mixed composition in October.

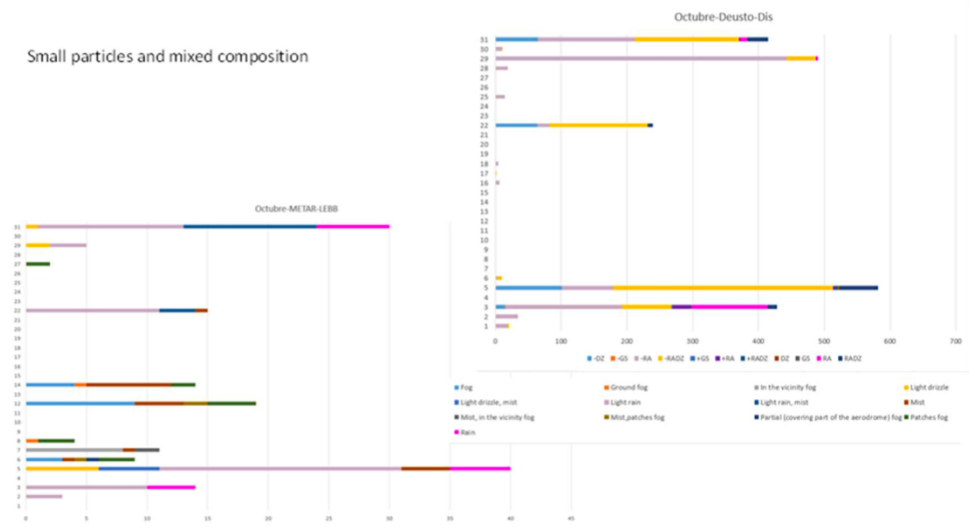
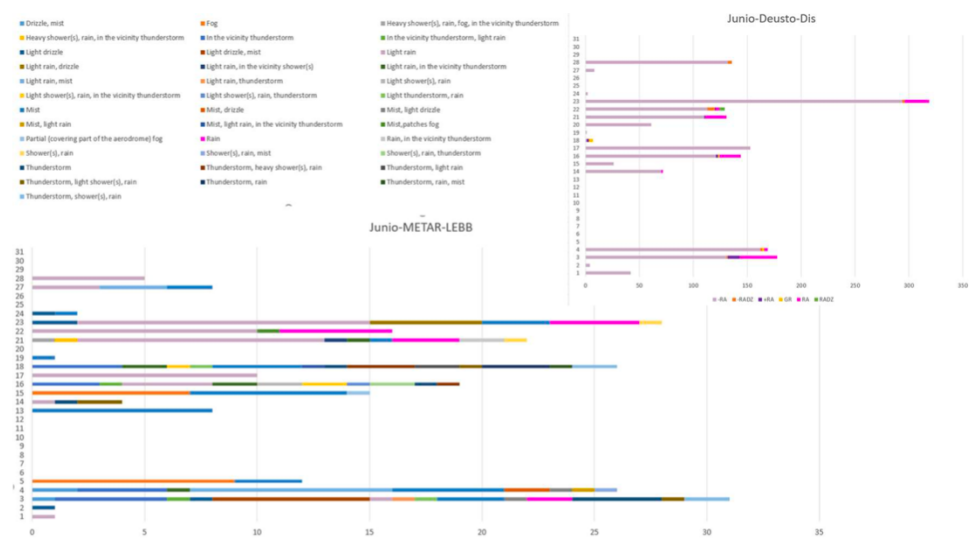


Figure 8
The Metar describe more type of hydrometers or "present weather situations" than the disdrometers



Fourth phase: Comparison between two coastline points and Z/R values obtained.

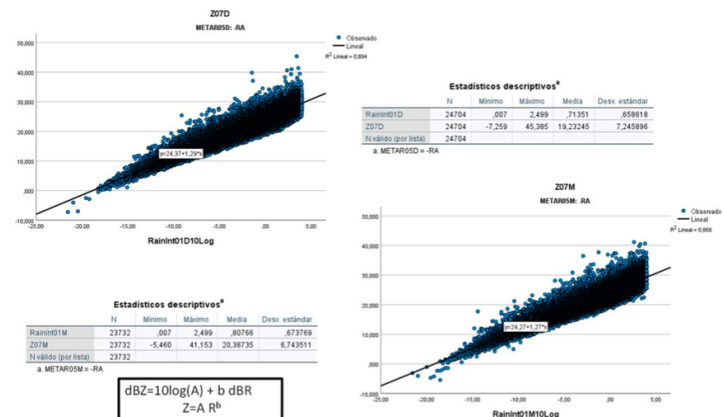
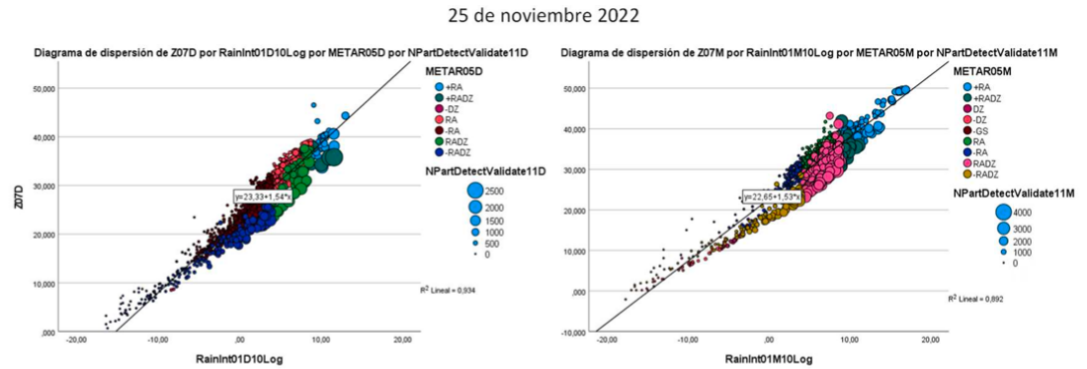


Figure 9
The most frequent hydrometer registered in both stations is the "-RA" the constants of the Z/R relationship are calculated using a linear model from the annual database.

Figure 10

The Z/R relationship is calculated from both stations on 25th November 2021. The type of hydrometer is colored and the size is the number of particles detected. Number of particles and size must be considered to find better adjustments.



5. CONCLUSIONS

In complex terrain, all available information is useful to improve and get closer to reality. The integration of the Kapildui and Jata radars together with the stations makes it possible to obtain a "Surface Rain Intensity-SRI" product with better results, but conditional on the quality of the data. But the integration of new observations has never been direct, because it is important to assess the independence and representativeness of these new observations, the quality in a wide range of meteorological conditions and their contributions to the operational products, without losing the traceability of the information. The disdrometer data is highly recommended for use in combination with radar to derive the Z/R ratio associated with the type of hydrometeor recorded. The Z/R ratios obtained by the disdrometer. Comparison with METAR data from the airport is not easy due to the different nature of the data. When the duration of precipitation is low or the observed composition of precipitation is heterogeneous, the differences are more pronounced. On the other hand, when the precipitation is persistent throughout the day and the composition is rainfall with variations in intensity, the matches are greater. Before using the data from the disdrometer network in the calculation of the Z/R ratio, more work needs to be done on the number and type of particles detected and the R-values recorded under different meteorological conditions, which is the aim of future work.

ACKNOWLEDGMENTS

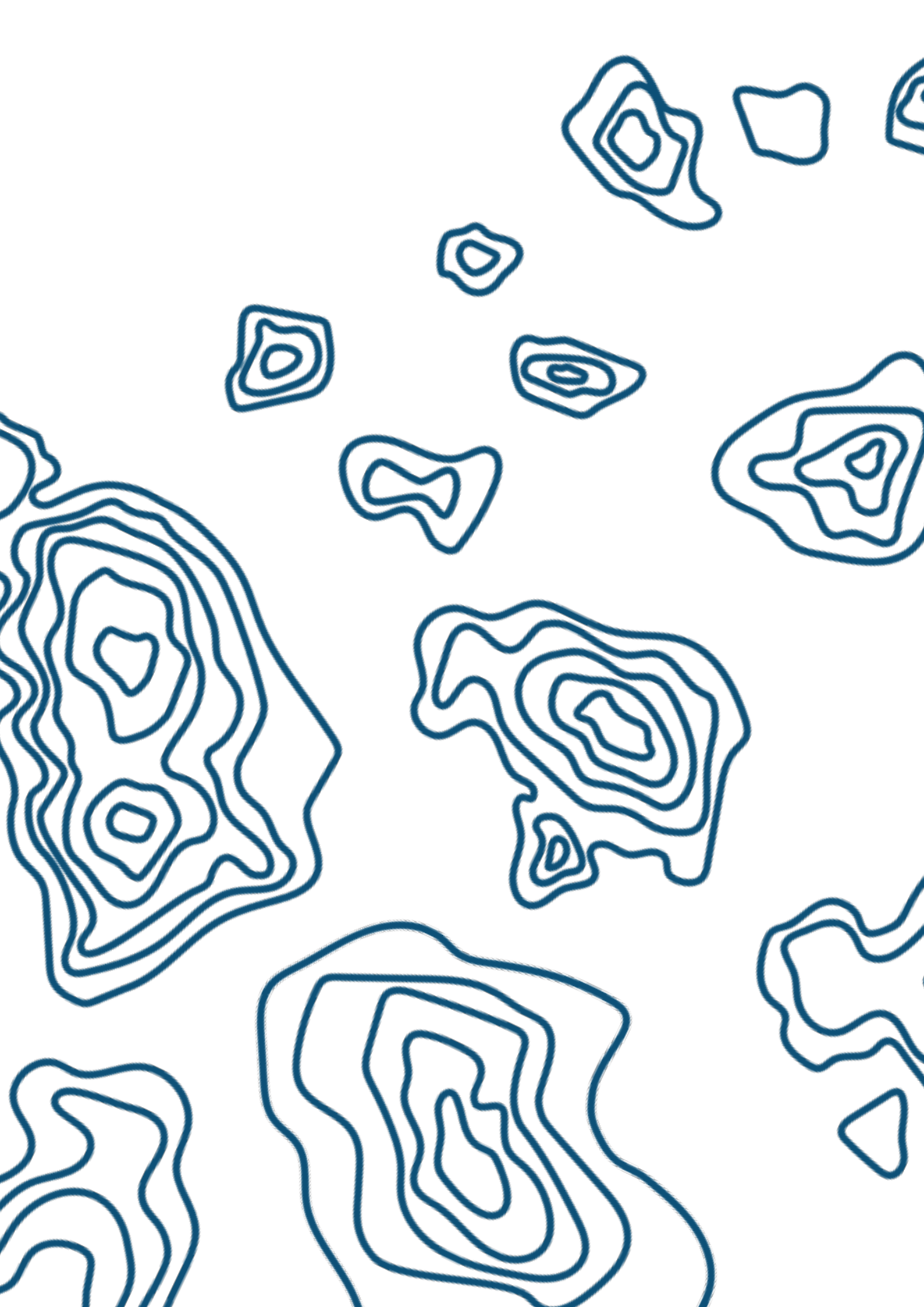
The authors would like to thank the emergency care and meteorology directorate DAEM and Euskalmet for their work in maintaining and expanding their hydrometeorological observation systems and offering the scientific community the databases for their exploitation. Furthermore, this work has been possible thanks to the collaboration between the company and the university, Tecnalia and the Bilbao School of Engineering (UPV/EHU) respectively.

REFERENCES

- AEMET. (2021). *Guía MET. Información Meteorológica Aeronáutica*. AEMET. Madrid: AEMET. Obtenido de https://www.aemet.es/es/conocermas/aeronautica/detalles/Guia_MET
- AEMET. (04 de 08 de 2022). *Radar de Jata en Vizcaya*. Obtenido de *Radar de Jata en Vizcaya*: <http://hdl.handle.net/20.500.11765/1144>
- Agencia Estatal de Meteorología. (20 de 04 de 2022). AEMET. Obtenido de <http://www.aemet.es/es/portada>
- Ángulo-Martínez, M., Beguería, S., Latorre, B., & Fernández Raga, M. (08 de 05 de 2018). *Hydrology and Earth System Sciences*. Recuperado el 10 de 04 de 2022, de

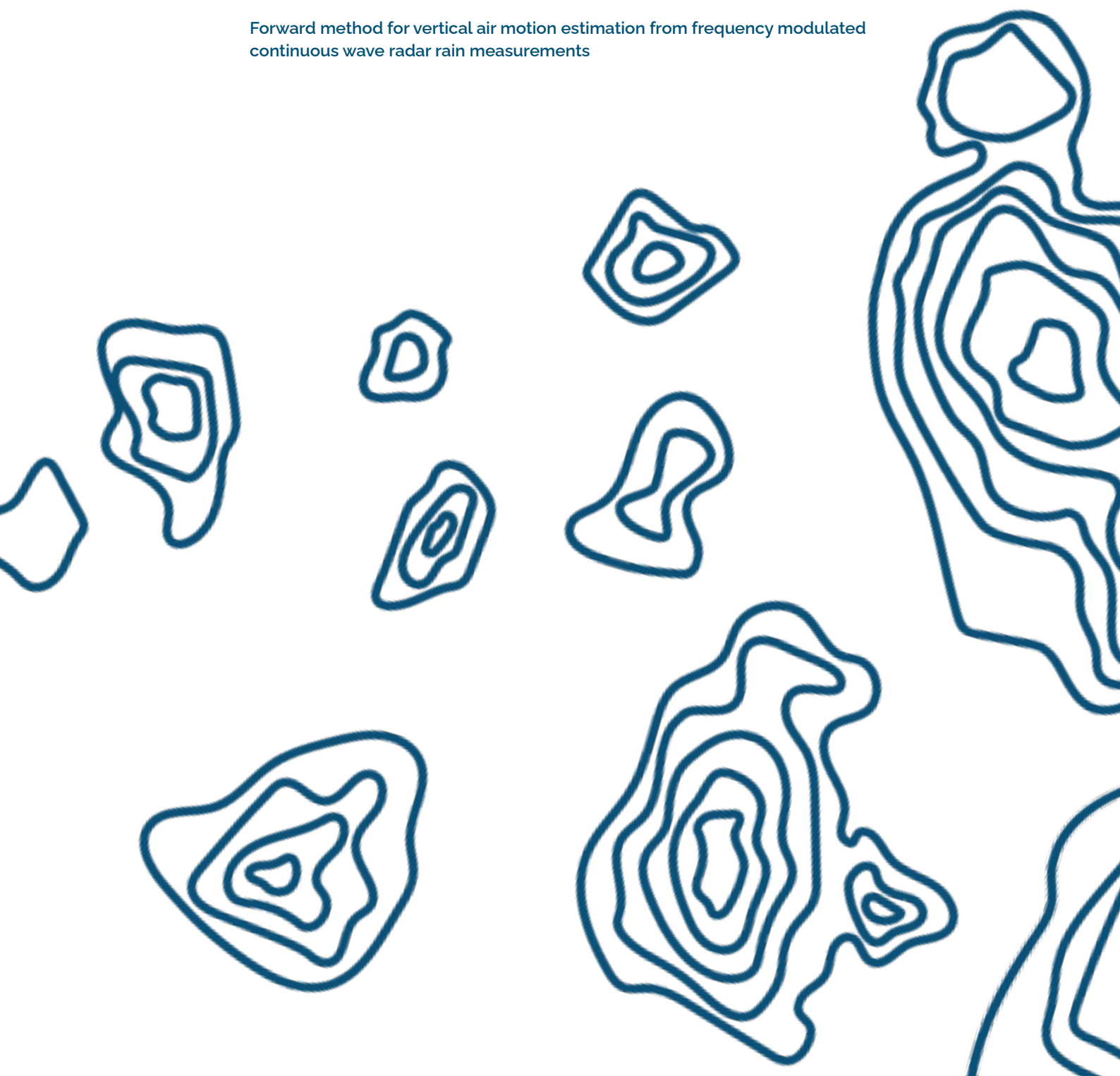
<https://hess.copernicus.org/articles/22/2811/2018/hess-22-2811-2018.pdf>

- Aranda, J., & Morais, A. (2006). *The new radar of Basque Meteorology Agency: site selection, construction and installation. Fourth European Conference on Radar in Meteorology and Hydrology* (pág. 4). Barcelona: *Proceedings of the conference*.
- Belmonte, M.-a. L., & Bellini Saibene, Y. (09 de 2017). INTA DIGITAL. Recuperado el 20 de 05 de 2022, de Repositorio Institucional Biblioteca Digital: <https://repositorio.inta.gob.ar/handle/20.500.12123/4500#>
- Bennett, A. (03 de 2012). BRISTOL INDUSTRIAL AND RESEARCH ASSOCIATES LIMITED. Recuperado el 13 de 04 de 2022, de Introduction to atmospheric visibility estimation: https://www.biral.com/wp-content/uploads/2015/02/Introduction_to_visibility-v2-2.pdf
- Euskalmet. (05 de 08 de 2022). Euskalmet. Observación. Datos de las estaciones. Obtenido de Euskalmet. Observación. Datos de las estaciones: <https://www.euskalmet.euskadi.eus/observacion/datos-de-estaciones/>
- Eustat. Instituto Vasco de Estadística. (05 de 08 de 2022). Población. Obtenido de Población: https://www.eustat.eus/estadisticas/tema_159/opt_0/tipo_12/ti_poblacion/temas.html
- Friedrich, K., Kalina, E., & Aikins, J. (2016). Raindrop size distribution and rain characteristics during the 2013 Great Colorado Flood. *American Meteorological Society*, 67.
- Gaztelumendi, S., Egaña, J., Gelpi, I., Otxoa de Alda, K., Maruri, M., & Hernández, R. (2006). *The new radar of Basque Meteorology Agency: Configuration and some considerations for its operative use. Fourth European Conference on Radar in Meteorology and Hydrology* (pág. 4). Barcelona: *Proceedings of the conference*.
- Gaztelumendi, S., Egaña, J., Otxoa-de-Alda, K., Hernandez, R., Aranda, J., & Anitua, P. (2012). An overview of a regional meteorology warning system. *11th EMS Annual Meeting 10th European Conference on Applications of Meteorology (ECAM)*, 8, págs. 157-166. Germany: *Advances in Science and Research*. doi:10.5194/asr-8-157-2012
- Gaztelumendi, S., Otxoa de Alda, K., Egaña, J., & Gelpi, I. (2006). Inclusion of Radar information in the surveillance panel of the Basque Meteorology Agency. *Fourth European Conference on Radar in Meteorology and Hydrology* (pág. 4). Barcelona: *Proceedings de la conferencia*.
- Harrison, D. L., Driscoll, S., & Kitchen, M. (21 de 11 de 2000). Improving precipitation estimates from weather radar using quality control and correction techniques. *En Meteorological Applications* (Vol. 7, págs. 135- 144). doi:10.1017/S1350482700001468
- Löffler-Mang, M., & Joss, J. (2000). An Optical Disdrometer for Measuring Size and Velocity of Hydrometeors. *Journal of Atmospheric and Oceanic Technology*, 130-139.
- Nemeth, K., & Beck, E. (05 de 2011). OTT Parsivel 2. Recuperado el 20 de 05 de 2022, de file:///C:/Users/g11834/Downloads/110501-ME-OT-WT-ar-Parsivel2_METEOROLOGICAL-EN.pdf
- Nemeth, K., & Martin, L.-M. (2006). OTT PARSIVEL @ENHANCED PRECIPITATION IDENTIFIER FOR PRESENT WEATHER, DROP SIZE DISTRIBUTION AND RADAR REFLECTIVITY - OTT MESSTECHNIK, GERMANY. TECO 2006 (pág. 4). Bruselas: *Proceedings TECO 2006 (WMO)*. Obtenido de [https://library.wmo.int/pmb_ged/wmo-td_1354_en/P1\(08\)_Nemeth_Germany.pdf](https://library.wmo.int/pmb_ged/wmo-td_1354_en/P1(08)_Nemeth_Germany.pdf)
- OTT HYDROMET. (2016). OTTHYDROMET. Obtenido de Instrucciones de funcionamiento del OTT Parsivel2: <https://www.ott.com/es-la/productos/download/operating-instructions-present-weather-sensor-ott-parsivel2-without-screen-heating-idioma-del-do-1/>
- Puerto de Bilbao. (05 de 08 de 2022). Bilbao Port. Obtenido de Bilbao Port: <https://www.bilbaoport.eus/>
- Sintés, E., & Joan, B. (05 de 08 de 2022). Precipitation analysis using disdrometer observations (2018). Obtenido de *Precipitation analysis using disdrometer observations (2018)*: <http://diposit.ub.edu/dspace/bitstream/2445/125266/1/Sintes%20Guardia%20Eva.pdf>
- WMO. (05 de 08 de 2022). Information for Decision-Making. Obtenido de *Information for Decision-Making*: <https://public.wmo.int/en/resources/2017-annual-report-services-decision-making/information-decision-making>



RADAR SIGNAL AND DOPPLER PROCESSING

Forward method for vertical air motion estimation from frequency modulated continuous wave radar rain measurements





FORWARD METHOD FOR VERTICAL AIR MOTION ESTIMATION FROM FREQUENCY MODULATED CONTINUOUS WAVE RADAR RAIN MEASUREMENTS

Andreu Salcedo-Bosch¹, Francesc Rocadenbosch^{1,2,*}, Stephen Frasier³, Paula Domínguez-Pla¹

¹*CommSensLab-UPC, Department of Signal Theory and Communications (TSC), Universitat Politècnica de Catalunya (UPC)*

²*Institut d'Estudis Espacials de Catalunya (Institute of Space Studies of Catalonia, IEEC), Barcelona, Spain*

³*Microwave Remote Sensing Laboratory, University of Massachusetts, Amherst, MA 01003-9284*

**francesc.rocadenbosch@upc.edu*

ABSTRACT

Abstract — Vertically-pointed Frequency-Modulated Continuous-Wave (FMCW) radar measurements of rain are greatly influenced by strong vertical winds (vertical air motion, VAM) in convective rain scenarios. Particularly, 2nd order products such as rain rate (RR) and drop size distribution (DSD) experience high estimation errors due to VAM. In this work, we consider the estimation of VAM from vertically-pointed FMCW radar measurements in order to correct VAM-corrupted rain 2nd order products. We present preliminary research on a forward method to estimate VAM velocity at a particular height from S-band FMCW radar measurements in convective rain scenarios. The method relies on the parameterization of the DSD as a gamma distribution. It estimates the VAM along with the constitutive parameters of the gamma distribution by means of a parametric solver. The methodology is tested over long-duration, high-resolution measurements by the University of Massachusetts FMCW radar and validated against a ground-based disdrometer in the context of the Verification of the Origins of Rotation in Tornadoes Experiment-Southeast (VORTEX-SE).

1. INTRODUCTION

Radars and disdrometers have been widely used to measure precipitation processes in the atmospheric boundary layer [1]. Ground-based S-band frequency modulated continuous wave (FMCW) radars have been used to assess the atmospheric boundary layer precipitation microphysical processes for more than 40 years [2], as they are unaffected by rain attenuation [3], [4]. Vertically-pointed FMCW radars permit the derivation of key rain 2nd order (integral?) parameters such as DSD and RR, among others [5]. The radar high spatial and temporal resolution permit an accurate monitoring of precipitation vertical profiles. Disdrometers record raindrop counts (at ground level) for different diameters during a measurement interval, and precisely derive rain DSDs from which 2nd order parameters such as RR can be obtained. However, each of these devices has its limitations. On one hand, the disdrometer is not able to give information of the vertical variations of precipitation. Moreover, large errors are common in scenarios with small diameter raindrops and low rain. On the other hand, radars have difficulty precisely measuring precipitation at low heights due to

interference from ground clutter, near-field effects, and parallax influence (for FMCW radars employing dual antennas). Additionally, radars estimate the DSD from radar Doppler spectrum by assuming that rain drops are Rayleigh scatterers that fall at their terminal velocities, which are determined by the drop diameter. In practice, the droplets falling velocity are influenced by the vertical air motion (VAM) [6], which arises as a radar-measured spectrum shift in the velocity axis. In the presence of large VAM, such as in convective rain scenarios, radar-derived DSD and 2nd order parameters may be corrupted [4], [6]. The VAM estimation and correction from stand-alone Doppler radar measurements has been of interest since the beginning of radar usage in precipitation measurement [7]. Lhermitte [8] proposed a method to differentiate VAM and raindrops terminal velocity in W-band ($\lambda = 3.2$ mm) radars by exploiting Mie scattering. The VAM is determined by comparing the observed spectrum to a predicted spectrum assuming no VAM. However, this is only feasible for very-short wavelengths. Hauser and Amayenc [7] proposed a fitting method in which the DSD was assumed to be with an exponential form characterised by two parameters (Marshall-Palmer distribution). This methodology optimised the best fit between the theoretical spectrum retrieved from the DSD model (shifted by VAM) with respect to the experimental spectrum observations. However, it required exponentially distributed size distributions and it is not suited for convective rain scenarios. More recently, Tridon and Van Baelen [6] proposed a VAM-correction method by shifting the radar-measured spectrum to maximise the correlation with a no-VAM scenario. Rocadenbosch et al. [4] proposed a VAM estimation method based on the correspondence between Z-RR measurements with three different Z-RR models. It consisted on a trial-and-error procedure in which the radar-measured spectrum was shifted until Z-RR relationship matched theoretical models. A similar approach was proposed by Kim and Lee [9], which resorted to radar reflectivity empirical relationships as well to estimate the VAM and then unshift the spectrum. However, they require user expertise in rain radar observations for an accurate correction. In contrast, here, departing from the proposal by Hauser and Amayenc [7], a forward method to estimate the VAM from stand-alone radar measurements is presented. The foundations of the forward method are to parameterise the DSD as a Gamma distribution and to project this parametric DSD through the radar processing chain up to the retrieved radar-measured reflectivity. The methodology is tested over experimental data measured by a vertically-pointed FMCW radar and validated by a disdrometer as a reference during a convective rain event in VORTEX-SE campaign in 2017. The paper is structured as follows: section II describes the VORTEX-SE campaign and presents the OTT Parsivel2 disdrometer and the UMASS S-band radar; section III revisits the disdrometer and rain radar operation procedure as well as the VAM correction method; section IV shows a case study of the VAM correction method; and section V gives concluding remarks.

2. INSTRUMENTS

The Verification of the ORigins of Rotation in Tornadoes Experiment-Southeast (VORTEX-SE) measurement campaign aimed at studying how different environmental scenarios affected the formation, characteristics, and evolution of tornadoes in the Southeast United States. The second measurement campaign of VORTEX-SE took place between 8 March and 8 May 2017 in northern Alabama. It involved multiple fixed and mobile instruments assessing the spatial and temporal evolution of storm events. During the experiment, the UMass S-band FMCW radar was deployed at the Scottsboro, Alabama airport along with an OTT Parsivel2

disdrometer, part of the Portable In-situ Precipitation Sensor (PIPS) package deployed by Purdue University. The S-band FMCW radar was developed by the Microwave Remote Sensing Laboratory from the University of Massachusetts (UMASS). It is a transportable radar which uses two parabolic dish antennas of 2.4 m diameter with 34 dB gain, with a transmitter of 250 W [10]. It is able to vertically profile the volume reflectivity spectral density as a function of velocity ($\eta(v)$) with temporal and spatial resolutions of 16 s and 5 m, respectively. The radar bandwidth permits to measure drop falling velocities up to 14 m/s. Thanks to the radar signal wavelength, the atmospheric boundary layer can be studied both in clear-air and precipitation scenarios. The OTT Parsivel2 is a laser-based disdrometer able to measure the ground-level rain droplets distribution as a function of diameter and falling velocity [11]. Its operation is based on the shadowing effect that drops generate when passing through a light band. From the hydrometeors distribution, 2nd order parameters such as RR and DSD can be derived. It has been widely used in measurement campaigns, and here, it will be used as a reference.

3. METHOD

A. Radar Data Products

Following [4], the DSD is obtained as the ratio of the volume reflectivity density with respect to the drop diameter, $\eta(D)$ [m^{-1}/mm], to the single-particle backscattering cross section of a drop of diameter D , $\sigma(D)$ [m^2/drop]. It can be formulated as

$$N(D) = \frac{\eta(D)}{\sigma(D)}. \quad (1)$$

FMCW radars are able to measure the volume spectral reflectivity, $\eta(v)$, which is the volume reflectivity (or radar cross section per unit volume) per unit Doppler velocity. In order to retrieve the DSD from radar measurements (see Equation 1 above), we need to express the spectral reflectivity as a function of drop diameter. To do so, the relationship $\eta(D)\partial D = \eta(v)\partial v$ is used. This relationship was found empirically by [12], and was put expressed analytically by [13] as

$$v_n(D)[\text{m/s}] = (9.65 - 10.3e^{-0.6 \cdot D[\text{mm}]})\delta v(h), \quad (2)$$

where $\delta v(h)$ is the height-dependent density correction for the terminal fall velocity, which is formulated as

$$\delta v(h) = 1 + 3.68 \cdot 10^{-5}h + 1.71 \cdot 10^{-9}h^2, \quad (3)$$

where h is the measurement height. From the DSD, second order products such as the reflectivity factor Z and the RR can be derived. The radar reflectivity factor can be obtained as the sixth power of the DSD as

$$Z = \int_0^{\infty} N(D)D^6 dD, \quad (4)$$

and the RR can be estimated from the DSD third moment as a function of drop terminal fall velocity

$$RR = \frac{\pi}{6} \int_0^{\infty} N(D)D^3 v(D) dD. \quad (5)$$

B. VAM influence.

Without VAM, the radar-measured Doppler velocities match the raindrops terminal falling velocities ($v_{Doppler} = v(D)$). In presence of VAM, the hydrometeors falling velocities are determined by both the drop terminal velocity as a function of diameter ($v(D)$ Equation 2) and the VAM velocity (v_{VAM}). Then, the radar-measured Doppler velocity is given by

$$v_{Doppler} = v(D) + v_{VAM}. \quad (6)$$

Therefore, drop diameter retrieval from velocity measurements and subsequent derivation of $\eta(D)$, DSD, and RR need to include the correction $v(D) = v_{Doppler} - v_{VAM}$. As v_{VAM} could not be measured with the available instrumentation, we face a non-linear inverse problem in which we need to find the best v_{VAM} estimation given radar volume reflectivity density $\eta(v)$ measurement [14].

C. Forward model for VAM estimation

We propose a forward model approach to solve the inverse problem of radar RR retrieval as a function of the VAM correction by constraining the DSD as a gamma distribution:

$$N(D) = N_0 D^\mu e^{-\Lambda D}, \quad (7)$$

in which N_0 , μ , and Λ are the intercept, shape, and slope constitutive parameters of the distribution, respectively [15]. In an inverse problem, the parameters to be estimated are represented by the state vector \mathbf{x} , and the measurements actually made to estimate \mathbf{x} can be represented by the measurement vector \mathbf{z} [14]. In our inverse problem, the state vector \mathbf{x} to be estimated is formed by the DSD gamma distribution parameters and the VAM. It can be formulated as

$$\mathbf{x} = [N_0, \mu, \Lambda, v_{VAM}]^T. \quad (8)$$

The measurement vector \mathbf{z} is defined as the radar-measured volume reflectivity density $\eta(v)$. It is formulated as

$$\mathbf{z} = \eta(v). \quad (9)$$

\mathbf{z} is a $N \times 1$ dimension vector, being N the number of velocity bins measured by the radar. We depart from Equation 1 in order to obtain the volume reflectivity density as a function of diameter from the DSD as

$$\eta(D) = N(D)\sigma(D). \quad (10)$$

Then, we make use of the relationship $\eta(v)\partial v = \eta(D)\partial D$ to obtain the volume reflectivity density as a function of velocity as

$$\eta(v) = N(D)\sigma(D) \frac{\partial D}{\partial v}. \quad (11)$$

For each state vector \mathbf{x} there is an ideal measurement vector \mathbf{z} related by a forward function $f(\cdot)$. The radar DSD-to-reflectivity forward function is defined as the expanded form of Equation 11 above as

$$f(\mathbf{x}) = N_0 D(v_{VAM})^\mu e^{-\Lambda D(v_{VAM})} \sigma(D(v_{VAM})) \frac{\partial D(v_{VAM})}{\partial v}, \quad (12)$$

where $D(v_{VAM})$ is the velocity-to-diameter relationship (see Equation 2) and v_{VAM} is VAM velocity correction (see Equation 6). Then, the forward model can be defined as

$$\mathbf{z} = f(\mathbf{x}) + \epsilon, \quad (13)$$

where ϵ is a residual error term. In order to solve the inverse problem, and thus, to estimate the state vector \mathbf{x} , we resort to a constrained non-linear least-squares (LSQ) method, finding the optimal \mathbf{x} that minimizes the squared error ϵ^2 between the model observation $f(\mathbf{x})$ and the actual observation \mathbf{z} . It can be formulated as an optimization problem as

$$\mathbf{x} = \arg \min_{\mathbf{x}} \|\eta(v) - \hat{\eta}(v, \mathbf{x})\|^2 \quad (14)$$

where $\hat{\eta}(v, \mathbf{x})$ is the estimated radar volume reflectivity, output of the radar DSD-to-reflectivity forward function $f(\mathbf{x})$. The block diagram in Figure 1 represents the optimization problem. The optimization problem in Equation 14 is solved by means of the trust-region-reflective algorithm [16].

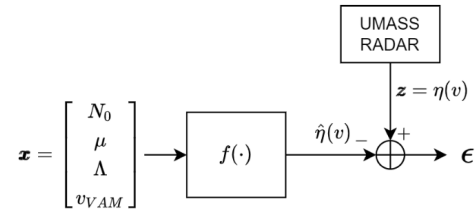


Fig. 1. Block diagram of the forward model algorithm. $f(\cdot)$ is the radar DSD-to-reflectivity forward function. The subtractor is used to compute the residual error, ϵ , between the measured and the estimated radar volume reflectivity density.

4. RESULTS AND DISCUSSION

The algorithm was tested over experimental data measured by the UMASS S-band FMCW radar and the OTT Parsivel2 during VORTEX-SE 2017 campaign (see section II). The VAM was estimated by means of the forward model method from radar volume reflectivity density measurements at 500 m. Reflectivity density measurements were 1-min averaged in order to reduce their uncertainty [7]. Then, radar measurements were corrected considering VAM estimations, and RR and DSD radar products at 500 m were recomputed. The VAM-corrected RR estimations were compared against the disdrometer RR as a reference, assuming vertical correlation between 500 m and 0 m measurement heights considering 10-min average ensembles. Although collision and coalescence processes are present in the precipitation process, correlation coefficients of $\rho \approx 0.75$ were found for the RRs between the radar measurements at 500 m and

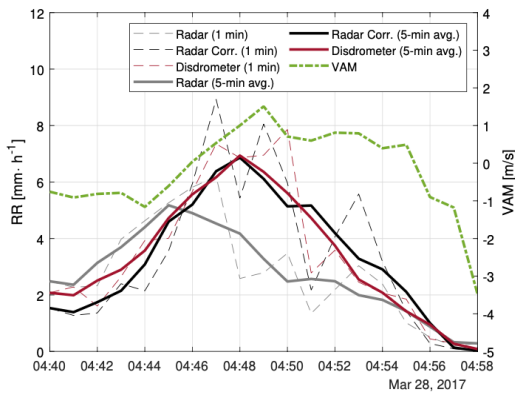


Figure 2
Time series representing the radar-measured RR (1 min), with (dashed black) and without (dashed gray) VAM correction, the disdrometer-measured RR (1 min, dashed red) and the VAM estimated by the forward method (green). Solid traces are the 5-min averaged versions of the respective dashed plots.

the disdrometer in the VORTEX-SE campaign [4]. Figure 2 shows the VAM estimation and correction results in terms of RR during a 20-minute observation period. By comparing the radar-retrieved RR without correction (dashed gray) to the disdrometer (dashed red), it can be observed how from 04:46 to 04:55 they largely disagree, being the first up to 3 mm · h⁻¹ lower than the latter. The VAM estimated by the inverse method presented in subsection III-C (dashed-dot green) shows constant -1 m/s values from 04:40 to 04:44, then it rises with a constant slope up to values around 1 m/s, and finally, at 04:55, it shows negative values down to -3 m/s. These VAM values seem to be in accordance with the RR, as a positive VAM implies a reduction of the radar-retrieved RR [17], corresponding to the 04:46-04:55 period in which the radar measures a lower RR as compared to the reference. After VAM correction, the radar-retrieved RR (dashed black) shows values of the same order of magnitude as the ones for the disdrometer, proving the validity of the VAM estimations. These results are further corroborated when comparing the 5-min window-averaged versions of the RR measurements (solid traces). The radar-measured RR (solid gray) shows significantly lower values in the 04:46-04:55 period with respect to the disdrometer (solid red). After correction, the radar-measured RR (solid black) matches almost ideally the reference. Note that when RR is very low, e.g., at 04:56-04:58 period, the VAM correction does not have a noticeable effect on the radar measurements, as reflectivity density values are too low. During the 04:40-04:44 period, it can be observed that the VAM-corrected radar RR shows lower values than the disdrometer reference. This may be due to an overestimation of negative VAMs. As a result, the algorithm estimates biased DSD parameters in order to match the measurements, i.e., to minimize the squared error between the measurement vector and the output of the forward function (see Equation 14). Figure 3 compares two DSDs measured by the radar, with and without VAM correction, against the reference DSDs measured by the disdrometer. Figure 3 a) plots the radar and the disdrometer DSD measurements at 04:43 UTC. Surprisingly, the VAM-corrected radar RR becomes underestimated (see Figure 2). As it can be observed, the raw DSD radar measurement (gray) virtually overlaps the reference (red). Therefore, the estimated VAM should be close to 0 m/s and no correction should be required. However, the forward method presented overestimates the VAM (VAM ≈ -0.8 m/s), compensating the poorer functioning of the forward method with a miss-estimation of the DSD constitutive parameters (N_0 , μ , and Λ), which leads to wrong DSD retrievals (black). On the other hand, Figure 3 b) depicts the comparison of DSD measurements at 04:49, where a VAM of 1.5 m/s is estimated. Here, a factor 10 difference can be observed between the radar-measured and reference DSDs. After VAM correction, the radar-measured DSD matches almost perfectly the reference. However, as previously reported in the literature [18], optical disdrometers underestimate DSDs at low diameters (see $D < 0.5$ mm at Figure 3 b)).

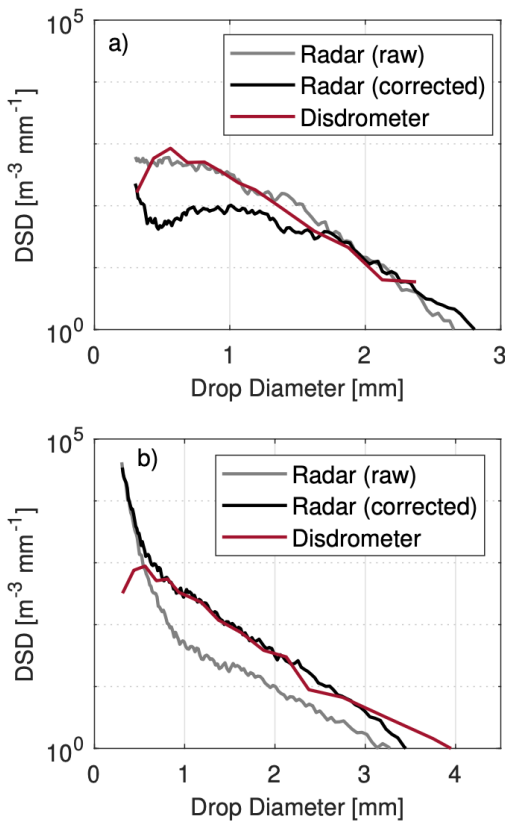


Figure 3
Comparison between DSDs measured by the radar, with (black) and without (gray) VAM correction, and the disdrometer (red). Two case examples are shown: (a) biased VAM estimation; (b) good VAM estimation.

5. CONCLUSIONS

An inverse method to estimate VAM velocity from stand-alone radar measurements was presented. The method consists on fitting a modelled volume reflectivity density, as a function of the VAM and DSD gamma distribution constitutive parameters, to the radar-measured reflectivity. The method was tested over experimental data captured during a 20-minute period by an S-band FMCW radar and validated with an OTT Parsivel2 disdrometer in the context of VORTEX-SE 2017 measurement campaign. The estimation results found VAM values mainly ranging from -1 m/s up to 1.5 m/s during the period under analysis. After VAM correction, the

radar-measured RRs were found to match almost ideally the disdrometer-measured RR for positive VAM values. However, overestimation of VAM negative values was found in no-VAM scenarios, leading to miss-estimation of the DSD constitutive parameters. These results were corroborated by comparing radar-retrieved DSD (with and without VAM correction) to disdrometer measurements. Although promising, the algorithm still needs to be further tested over different stratiform and convective rain scenarios in order to see if overestimation of negative VAM is also found, and how to improve these estimations. The VAM estimations could also be further validated by direct measurements of vertical wind by wind profilers.

REFERENCES

- [1] R. R. Rogers, "A review of multiparameter radar observations of precipitation," *Radio Science*, vol. 19, no. 01, pp. 23–36, 1984.
- [2] T. Ince, S. J. Frasier, A. Muschinski, and A. L. Pazmany, "An s-band frequency-modulated continuous-wave boundary layer profiler: Description and initial results," *Radio Science*, vol. 38, no. 4, 2003. [Online]. Available: <https://agupubs.onlinelibrary.wiley.com/doi/abs/10.1029/2002RS002753>
- [3] R. L. Tanamachi, S. J. Frasier, J. Waldinger, A. LaFleur, D. D. Turner, and F. Rocadenbosch, "Progress toward Characterization of the Atmospheric Boundary Layer over Northern Alabama Using Observations by a Vertically Pointing, S-Band Profiling Radar during VORTEX-Southeast," *J. Atmos. Ocean. Technol.*, vol. 36, no. 11, pp. 2221–2246, 2019.
- [4] F. Rocadenbosch, R. Barragán, S. J. Frasier, J. Waldinger, D. D. Turner, R. L. Tanamachi, and D. T. Dawson, "Ceilometer-based rain-rate estimation: A case-study comparison with s-band radar and disdrometer retrievals in the context of vortex-se," *IEEE Trans. Geosci. Remote Sens.*, vol. 58, no. 12, pp. 8268–8284, 2020.
- [5] R. J. Doviak et al., *Doppler radar and weather observations*. Courier Corporation, 2006.
- [6] F. Tridon, J. Van Baelen, and Y. Pointin, "Aliasing in micro rain radar data due to strong vertical winds," *Geophysical Research Letters - GEOPHYS RES LETT*, vol. 38, 01 2011.
- [7] D. Hauser and P. Amayenc, "A New Method for Deducing Hydrometeor-Size Distributions and Vertical Air Motions from Doppler Radar Measurements at Vertical Incidence," *Journal of Applied Meteorology and Climatology*, vol. 20, no. 5, pp. 547 – 555, 1981.
- [8] R. M. Lhermitte, "Observation of rain at vertical incidence with a 94 ghz doppler radar: An insight on mie scattering," *Geophysical Research Letters*, vol. 15, no. 10, pp. 1125–1128, 1988.
- [9] D.-K. Kim and D.-I. Lee, "Raindrop size distribution properties associated with vertical air motion in the stratiform region of a springtime rain event from 1290 mhz wind profiler, micro rain radar and parsivel disdrometer measurements," *Meteorol. Appl.*, vol. 23, no. 1, pp. 40–49, 2016.
- [10] J. Waldinger, T. Hartley, W. Heberling, S. Frasier, and R. Tanamachi, "S-band fmcw boundary layer profiler: System upgrades and results," in *2017 IEEE International Geoscience and Remote Sensing Symposium (IGARSS)*, 2017, pp. 4526–4529.
- [11] A. Tokay, D. B. Wolff, and W. A. Petersen, "Evaluation of the new version of the laser-optical disdrometer, ott parsivel2," *Journal of Atmospheric and Oceanic Technology*, vol. 31, no. 6, pp. 1276 – 1288, 2014.
- [12] R. Gunn and G. Kintzer, "The terminal velocity of fall for water droplets in stagnant air," *Journal of Atmospheric Sciences*, vol. 6, pp. 243–248, 1949.
- [13] D. Atlas, R. C. Srivastava, and R. S. Sekhon, "Doppler radar characteristics of precipitation at vertical incidence," *Reviews of Geophysics*, vol. 11, pp. 1–35, 1973.
- [14] C. D. Rodgers, *Inverse methods for atmospheric sounding: theory and practice*, ser. *Series on Atmospheric, Oceanic and Planetary Physics*, F. Taylor, Ed. World scientific, 2004, vol. 2.
- [15] A. Tokay and D. A. Short, "Evidence from tropical raindrop spectra of the origin

of rain from stratiform versus convective clouds," Journal of Applied Meteorology and Climatology, vol. 35, no. 3, pp. 355 – 371, 1996.

• [16] J. J. More and D. C. Sorensen, "Computing a trust region step," *SIAM Journal on scientific and statistical computing, vol. 4, no. 3, pp. 553–572, 1983.*

• [17] A. Salcedo-Bosch, P. Dominguez-Pla, F. Rocadenbosch, and S. Frasier, "Numerical Solver for Vertical Air Motion Estimation." in *2022 IEEE Int. Geo. Rem. Sens. Symp. (IGARSS-2022). IEEE, 2022, accepted.*

• [18] D. Jash, E. Resmi, C. Unnikrishnan, R. Sumesh, T. Sreekanth, N. Sukumar, and K. Ramachandran, "Variation in rain drop size distribution and rain integral parameters during southwest monsoon over a tropical station: An inter-comparison of disdrometer and micro rain radar," *Atmospheric Research, vol. 217, pp. 24–36, 2019.*

Concept *Urs Germann, Alexis Berne, Marco Gabella, Silvia Rao, Franziska Keller*

Design *Silvia Rao*

Format *PDF only*

Date *23 September 2022*

WITH SUPPORT FROM

The Federal Office of Meteorology and Climatology MeteoSwiss
L'École Polytechnique Fédérale de Lausanne EPFL



Schweizerische Eidgenossenschaft
Confédération suisse
Confederazione Svizzera
Confederaziun svizra

Swiss Confederation

Federal Department of Home Affairs FDHA
Federal Office of Meteorology and Climatology MeteoSwiss

EPFL

MeteoSwiss

